Ollscoil na hÉireann, Corcaigh

National University of Ireland, Cork

Preparation and Characterization of AlGaN structures for UVA LEDs

Thesis presented by

Sandeep Madhusudan Singh, M. Tech

for the degree of

Doctor of Philosophy

University College Cork

Electrical and Electronic Engineering

Head of School/Department: Prof. Jorge Oliveira

Supervisor(s): Prof. Peter J. Parbrook

Co-Supervisor: Dr. Stefan Schulz

Co-Supervisor: Dr. Vitaly Z. Zubialevich

2024

Table of Contents

Acknowlegement

Now, when my PhD adventure is almost over, I finally can reflect on people without whom it would not be possible. Firstly, I would like to thank Prof. Peter J. Parbrook and Dr. Stefan Schulz for inviting me to the UV LED project and thus allowing me to pursue my doctoral research in the Photonics group at Tyndall National Institute, UCC. I would not say that all four years of the program were smooth, there were many ups and downs as well as rough times due to COVID-19 pandemic. In this scientific endeavour, the only thing that kept me consistently on track was the supervision from my thesis committee, which I want to acknowledge for the patience, guidance, and teaching that helped me evolve through the various stages of the PhD program and led me to bridge scientifically relevant gaps in the area of III-N semiconductors.

I specifically thank Dr. V. Zubialevich for his patience in listening, training, teaching and rectifying my understanding of III-nitrides, enhancing my story-telling ability and helping with the preparation of the graphical representation of my scientific data.

I also thank Dr. P. Pampili for sharing his critical insights into the nuances of the X-ray characterization of my samples.

This project also helped me discover great colleagues and friends like Dr. Thomas O'Connor, Peter Milner and Robert Finn; without their input, discussions and criticism, my understanding of the larger picture of III-nitride semiconductors would not be deep enough.

I would like to thank Peter Milner and Dr. V. Zubialevich for the fabrication of the unipolar devices and µ-honeycomb templates which were used to carry out corresponding parts of this thesis.

For a researcher, making friends outside their research group is sometimes tough, certainly harder in an international place like Tyndall than back home (due to cultural, linguistic and religious diversity here). Furthermore, in the PhD stage of life, this is even more challenging due to too much focus on own research. Nevertheless, I thank my housemate and friend Amit Tanwar for the quality time spent over the last four years, and for his diligent support, compassion and patience. Outside Tyndall, my friends were the social fabric that helped me escape and forget the day-to-day research

issues, effectively allowing me to look at my scientific problems from a fresh perspective.

I am deeply grateful to my grandmother and late grandfather for being the sky and my parents for being the roof under which I could accomplish whatever I have.

Finally, I would like to thank the Science Foundation Ireland and IPIC for supporting my PhD scholarship without which I for sure could not be able to contribute towards this scientific topic.

Abstract

Visible / UV LEDs are developed from the same III-Nitride compounds semiconductor materials and share many design and technological aspects. However, the efficiency difference between the two types is quite significant, where the latter lags. Recent advancements in material technology such as the development of template/buffer, strain engineering, optimisation in doping techniques and the overall design of a UVLED structure have made it possible to achieve decent performance from UV LEDs. This sufficient performance together with the high demand for mercury-free UV light sources has led to an increase in the market share of UV LEDs, compared to other existing UV light sources.

Since a comprehensive study of a UV LED in general is too broad a topic for a PhD thesis, the focus of this work is concerned with two particular research questions i.e.: a) Since AlGaN is routinely used as an electron-blocking layer in visible and UV LEDs, does it act as such and how effective is it? b) How to achieve a low dislocation density template for UV (310-350 nm) LEDs where no native substrates for homoepitaxy are available for low-mid Al content AlGaN?

III-Nitride based LEDs generally use AlGaN as an electron blocking layer (EBL) to prevent surplus electron overflow from the active region of an LED into its p-doped region during device operation. The effectiveness of an AlGaN layer as an EBL has been studied in the literature using an unipolar structure (consisting of *n*-GaN/*uid*-AlGaN/*n*-GaN), and those results suggest that it is not as efficient as expected, which contradicts its successful routine use in LEDs. This discrepancy has generated interest in this topic, and so both simulation and experimental analysis of the proposed unipolar structure were carried out in this study. Simulation shows a rectifying nature of the AlGaN barrier, and, in contrast to previously published results, experimental results from this study corroborate the modelling. However, conditions leading to non-rectifying behaviour were also identified. Specifically, non-rectifying behaviour is observed for samples with barriers of Al content less than ~12%, and/or when a growth pause is introduced before and after AlGaN barrier growth. Based on our results, it can be concluded that AlGaN can indeed act as an efficient EBL in LEDs if the contrast in Al composition between EBL and last quantum barriers is at least ~15%.

Another important aspect of an LED is a good quality template, which sets the dislocation density in the LED active region and affects significantly achievable internal quantum efficiency and thus the overall device performance. Significant effort in this regard was made to develop low dislocation density crack-free AlGaN buffer layers grown on planar *c*-plane substrates (PVDNC© AlN/sapphire from Kyma Technologies, Inc.). Another objective of the above efforts was to understand AlGaN growth and the effect of various growth parameters. The key achievement here was the implementation of a composition-graded layer, whose function was to partially compensate dislocation-induced tensile stress in Si-doped AlGaN, that allowed to increase in the total thickness of the buffer before it started cracking. Growth conditions which favour bright UV emission from MQWs despite the moderate crystalline quality of AlGaN thin films were also identified. This work led to the realization of a planar AlGaN template with thick (~2 μm), UV transparent and crack-free *n*-AlGaN buffer substrate with a total dislocation density of ~4×10^9 cm^{-2}.

As no further improvement in crystal quality was possible using standard planar approaches, to set a path towards an even lower dislocation density template for an efficient UV LED, AlGaN overgrowth on a patterned surface was explored. Regular arrays of hexagonally arranged μ-holes were chosen as a structure for the study (micro honeycomb, μ-HC). As μ-HC is composed of both convex and concave shapes, it makes it a good model structure for understanding surface morphology evolution and the overgrowth mechanisms underpinning it.

There are three aspects to this research topic. The first one is about optimizing the μ-pattern itself, and the second relates to finding overgrowth conditions in the multi-variable growth parameter space suitable for the coalescence of μ-patterns back into planar layers of hopefully improved quality. In the third part, the growth conditions were to be optimised to direct surface morphology evolution towards the formation of regular arrays of crystallographically faceted V-pits with almost no *c*-plane regions. My study suggests that growth parameters influence the morphological evolution of the micro-patterned AlGaN in such a way that both above-mentioned outcomes are possible. Despite most of the work being focused on AlGaN with an Al content of ~20%, the developed approach is believed to be suitable for growing low dislocation density AlGaN across the composition range required to cover the entire UVA spectral range. I think the developed templates can act as a base

for improved performance standard UV LEDs and novel-type micro-faceted semi-polar UV LEDs.

Abbreviations

UPHS	Unipolar heterostructure
PVDNC	Physical vapor deposition nano-columnar
KYMA	
PL	Photoluminescence
FWHM	Full-width half maxima
FEM	Finite element method
FDM	Finite difference method
µ-HC	Micro Honeycomb
XRD	X-ray diffraction
PR	Photo-resist
DD	Drift-diffusion
TDD	Threading dislocation density
LED	Light emitting diodes
UV	Ultra-violet

Introduction

LEDs have revolutionised the lighting industry by replacing the conventional incandescent/mercury-containing fluorescence bulbs. They are energy efficient, have longer lifetimes, and ease of handling has further promoted their adaptation. Moreover, these attributes have benefitted consumers by lowering the electricity bills incurred and shall eventually decrease humanity's carbon footprint. The realization of visible LEDs was possible due to advancements in III-nitride material technology, besides that III-nitride materials have the potential to emit light beyond the visible part of the spectrum i.e., shorter (ultraviolet, UV), and longer wavelengths (infrared). As depicted in Figure 1, the UV spectrum is mainly segmented into 3 parts: a) UVA (400-320 nm) b) UVB (320-280 nm) and c) UVC (280-200 nm). In this work, the focus is on the UV spectrum specifically in the UVA range as it is suitable for various applications ranging from disinfection[2,3] to biomedical[4–6], etc.

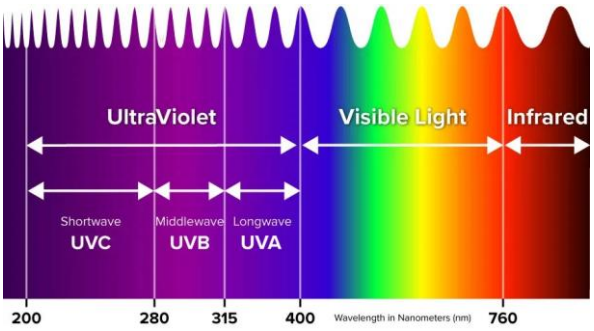

Figure 1: Schematic representation of spectral diapasons of electromagnetic radiation with light being the visible part of it (400-760 nm).
"Taken from reference 1"

UV LED Applications

Each segment of the UV spectrum can be utilized to target a unique set of applications which require the light output power to have a specific value shown in Figure 2. In this thesis, the discussion is mainly focused on UV LEDs with emission wavelengths from 310 to 350 nm, as they can be used in various such as curing[8], lithography[9] and biomedical

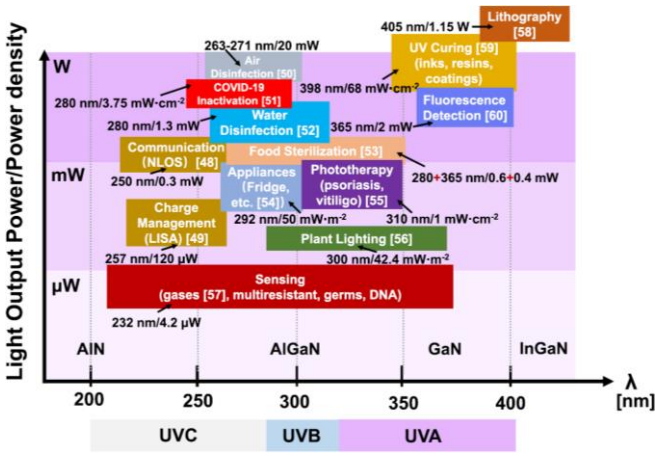

Figure 2: Application of UVA (400-320 nm), UVB (320-280 nm), and UVC (280-200 nm) LEDs.
"Taken from reference 7"

applications[5,10]. This UV region is specifically important for the phototherapeutic treatment of Vitiligo[4] and Psoriasis[6].

Earlier, cosmetic applications such as tanning, relied heavily on UV lamp-based solutions because of their cost-effectiveness and larger area of exposure. Nevertheless, UV LEDs are catching up in these applications because of their increasing efficiency and their ability to scale volume which plays a vital role in unit economics.

UV LED Market Share

UV LED demand is increasing year-on-year and is reflected in its market volume shown in Figure 3. UV LEDs pose the main competition to the existing UV lamps since they are cheaper and more mature technology in the marketplace. The majority of today's UV lamps are mercury-based bulbs which require warm-up time and are bulky and toxic for handling purposes.

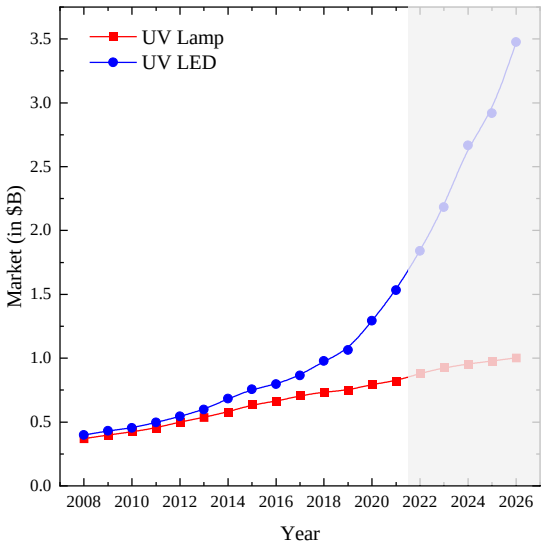

Figure 3:Market volume for UV LED and Lamps. Data extracted from 2021 Yole Developpment report. "Taken from reference 11"*

What is the reason behind the steady increase in the market volume of UV LEDs (Figure 3) compared to UV lamps? The answer is twofold: firstly, mercury is carcinogenic, and the industry requires a substitute. Secondly, UVLEDs are potentially more efficient than the mercury lamp technology. A further thrust for UV LED development was provided by the COVID pandemic which emphasised cost-effective disinfection applications using UV radiation[3].

This leaves an open question; can the adaptation of UV LEDs be further encouraged and what are the constraints which are holding it back? Answers to these questions require an in-depth understanding of the fundamentals related to the

* Concerns about the value of CAGR has been raised by Yole Developpment (private communication, 2023). However, this still represents the most recent available market analysis to the author's knowledge.

materials, design, and construction of a UV LED, as well as the challenges associated with the improvement of its efficiency.

A typical design of a UV LED is shown in Figure 4. Generally, it comprises seven regions: 1) *p*-region 2) Electron blocking layer (EBL) 3) Active region 4) *n*-region 5) Buffer 6) Template 7) Substrate. Charge carriers get injected into the active region from *p*/*n*-regions, recombine and generate light as a result.

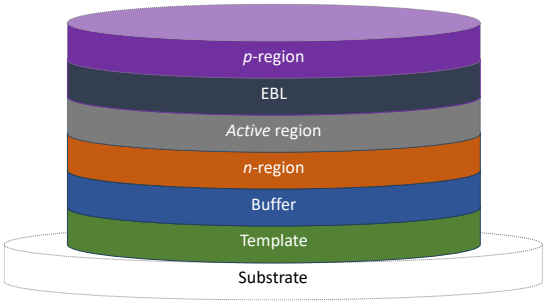

Figure 4: Typical design of a UV LED

The EBL serves to prevent electrons (as it is a more mobile type of charge carriers) from overflowing the active region straight to the *p*-region.

In homoepitaxy buffer layers provide lattice and thermal expansion coefficient matching between the substrate and LED epilayers, where as in the case of heteroepitaxy it is supposed is to minimise the generation of dislocations or filter the dislocation from propagating towards the active regions, after it is generated at the buffer substrate interface. In heteroepitaxy, where the buffer layers do not show significant quality improvement, high/moderate quality templates are preferred as they provide lattice and thermal expansion coefficient matching to the epilayers of the device. Details about these regions will be discussed in chapter 1.

The required knowledge and understanding for the development of a UV LED is being researched under the Irish Photonic Integration Centre biomedical project. The targeted UV LED should have an emission wavelength in the range of 310–350 nm and with an output power of 1 mW. The intent of the project is to use UV light for fluorescence[12,13] in endoscopy probes.

Outline of Thesis

The acquired knowledge regarding various aspects of a UV LED is very broad, so the focus of this thesis is on only some of them: (1) understanding the effectiveness of AlGaN as an EBL and (2) development of a low dislocation density buffer/template for an efficient UV LED. The overall structure of this work is described next.

Chapter 1 starts with the fundamentals of III-nitride materials, then goes on to elaborate more details about the overall UV LED design, its efficiency and the associated challenges related to the constituent layers with a particular focus on EBL and template development. Specifically, a general background on why the electron blocking layer is required and how it is studied using unipolar structures is provided. In addition to that, emphasis is also directed towards the need for a low dislocation density template for high-performance UV LED and what has been done in this regard in the literature before the start of this thesis. The chapter also concludes on existing gaps in the knowledge in this regard which defines the scope of further chapters of this thesis.

In Chapter 2, the experimental techniques which enable us to realise and characterise these UVLED building blocks will be discussed. Starting from the process technologies used in the epitaxy, fabrication, material and device characterization. Details of the growth conditions followed during the epitaxy of various templates/substrates and the fabrication process(work) flow for devices and template is also provided.

On the theoretical front, methods such as FEM, drift-diffusion, etc. utilized for the simulation of the unipolar structures will also be covered in this chapter.

Chapter 3 is focused on understanding unipolar transport through an intrinsic AlGaN layer sandwiched between *n*-doped GaN regions. This chapter is divided into two parts: in the first part, the result of simulation depicting the behaviour of a unipolar heterostructure is discussed. In the second part, experimental results[*] are discussed and compared to the previous simulations.

In Chapter 4, efforts are made to develop crack-free, transparent, thick, low dislocation density templates for UV LEDs. Initially, various planar approaches (e.g. AlN interlayer, etc.) were attempted during AlGaN growth to reduce dislocation density on a *c*-plane planar template. Realising the fact that reduction of dislocation density below mid 10^9 cm^{-2} is far from being trivial and requires more resources and time, efforts were redirected on utilizing AlGaN overgrowth on micro/nano-patterned (μ-holes) AlGaN templates[†] with low/moderate quality. In this work, optimization of

[*] Electrical characterization results were acquired from unipolar devices fabricated by Peter Milner.

[†] Fabrication of the μ-patterned templates was carried out by Dr V. Zubialevich, with some support from Peter Milner.

μ-holes and the surface morphology in different regions of the growth parameter space was studied intending initially to achieve a fully coalesced layer with reduction dislocation density.

Chapter 5 presents a summary of the thesis and provides an overall conclusion on the above-mentioned chapters. As well as suggests future works which can be pursued in these areas.

Chapter 1 Literature on III-Nitride Material and devices

This chapter focuses on the fundamental properties of III-nitride materials relevant to this thesis. Using this as a foundation, various aspects of UVLED device design, efficiency and challenges are discussed. Later, their connection and relevance to the research chapters/sections of the thesis are established.

1.1 Fundamental properties of III-Nitride materials

III-nitride materials have a defined hexagonal closed-packed crystal structure known as wurtzite (WZ)[15]. This crystal structure defines optical and electronic properties, some of which will be discussed below. Alloying different III-nitride materials opens up the immense possibilities to achieve any configuration with the desired composition. The composition of the material determines its lattice constant which dictates its respective energy bandgap. The ability to tune the energy bandgap by varying the composition allows the tuning of the emission wavelength of the material from IR to UV. 'Conventional' III-nitrides (i.e. excluding boron-containing alloys) are broadly classified into three different categories depending on their compositional configuration: binary compounds (III-N: InN, GaN, AlN), binary alloys ($^{A}III_{x}{}^{B}III_{1-x}N$: InGaN, AlGaN, InAlN) and ternary ($^{A}III_{x}{}^{B}III_{y}{}^{C}III_{1-x-y}N$: InAlGaN) alloys. In this thesis, we focus on GaN and $Al_xGa_{1-x}N$ ($x \leq 0.4$) alloys.

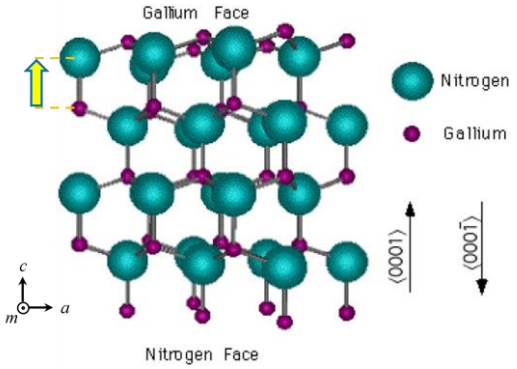

Figure 5: Crystal structure of GaN. "Taken from reference 14" Indicating the polar surface in III-Nitride materials. The direction of displacement of the hcp sublattices is indicated by an upwards arrow (in yellow).

The fundamental material properties of various III-nitrides have extensively been discussed[15–22] in books, review articles and previous theses defended in our/other research groups.

1.1.1 Crystal Structure

The most thermodynamically stable form of crystallization of III-nitride materials is wurtzite (WZ), which has a hexagonal symmetry[15] (referred to by space group $P6_3mc$). In this arrangement, the lattice constant $a = b \neq c$* and lattice angles are $\alpha = \beta = 90°, \gamma = 120°$, a unit cell of a wurtzite lattice† is shown in Figure 6. A summary of the lattice parameters of conventional binary material is provided in Table 1. For three-dimensional periodic structures, three-index Miller notation (*hkl*) is enough as for example it is used for cubic (symmetric) crystal structures. Since the hexagonal lattice is asymmetric in shape, the four-index form (*hkil*), known as Miller-Bravais, is useful but redundant so that the additional index '*i*' is equivalent to –(*h*+*k*).

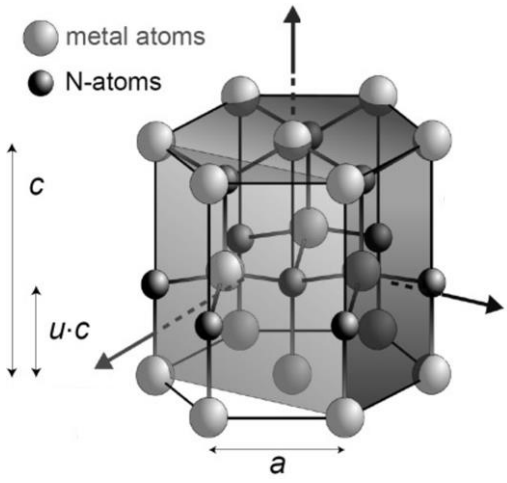

Figure 6: Wurtzite crystal structure of III-Nitride materials.
"Taken from reference 23"

Table 1: Lattice constants of wurtzite GaN and AlN at ambient condition[24].

III-Nitride Binary materials	*a* (Å)	*c* (Å)
GaN	3.189	5.185
AlN	3.112	4.982

The horizontal plane forming hexagons is called the basal plane and is denoted as (0001) or *c*-plane (Figure 7, *a*). This is the most commonly used plane for epitaxial growth of III-Nitrides. The other two main planes vertical (orthogonal (90°)) to the basal plane are denoted as *a*- and *m*-planes with corresponding Miller indices of $\{11\bar{2}0\}$ and $\{1\bar{1}00\}$ and are shown in Figure 7, *b* and *c*. Other than these, also slanted planes with respect to the basal one at angles < 90° are often used with examples of *a*-plane-tilted $\{11\bar{2}2\}$ and *m*-plane-tilted $\{1\bar{1}01\}$ shown in Figure 7, *d* and *e*.

* The lattice parameters of hexagonal unit cell are *c* and *a*.

† u is defined as the anion-cation bond length (also the nearest neighbor distance) devided by the *c*-lattice parameter.

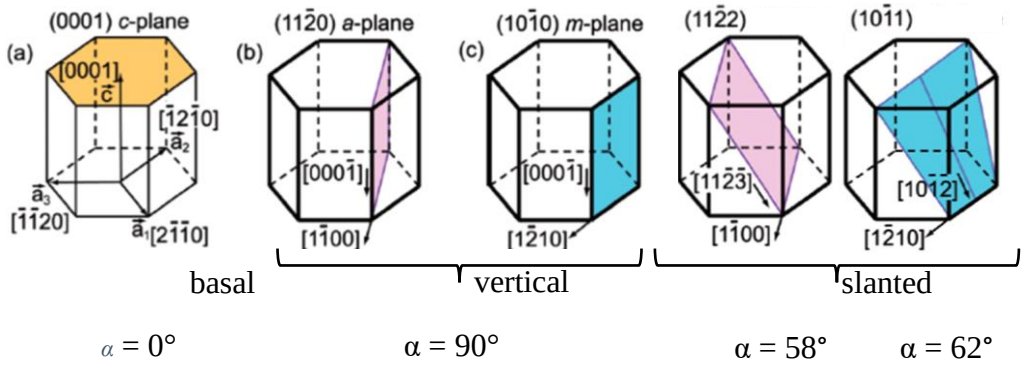

Figure 7: Crystallographic planes in III-Nitride materials. "Taken from reference 25"
The α angles were calculated for AlGaN with respect to the c-plane AlGaN (α = 0°). (modified for AlGaN)

Various electronic and optical properties of III-nitride materials and devices are, by virtue of crystal structure, dependent on orientation due to polarization present in III-nitrides, the concept which will be described next.

1.1.2 Polarity and polarization of III-nitrides

1.1.2.1 Polarity of crystal

In the III-nitride wurtzite crystal structure, group-III atoms define the cationic sub-lattice while nitrogen atoms define the anionic sub-lattice, as shown in Figure 5. Furthermore, in the wurtzite crystal structure, both these sub-lattices are interpenetrating hexagonal closed-packed ones. This occurs in such a way that they (both sub-lattices) are equally oriented with respect to the *c*-axis (no mutual twist) and displaced with respect to each other along it (i.e. *c*-axis). This breaks crystal structure symmetry along the *c*-direction, so that opposite III-nitride surfaces perpendicular to the *c*-axis are not equivalent, which makes the crystal polar in this direction. The polarity of III-nitride materials affects the surface morphology, electronic and optical properties, etc.

As was just stated, polarity is a consequence of the absence of an inversion plane perpendicular to [0001]. Conventionally, the polarity is defined by the direction of bonds from cation to anion in which two sub-lattices are displaced (i.e. *c*-direction [0001]). A *c*-plane surface is referred to as Ga-polar when the vector of displacement of sub-lattices from cation (Ga) to anion (N) atoms is directed out of the crystal as e.g. in Figure 5.

1.1.2.2 Polarization

III-Nitride materials form covalent bonds with sp^3 hybridisation so that crystal structure can be represented as a plurality-ordered tetrahedron* with a nitrogen atom inside it and shared ¼ metal atoms at its apexes. Due to the strong difference in electronegativity between the two element atoms[26], they are charged with opposite signs and show strong ionicity (ionic character). Despite this, the ideal tetrahedron† does not have any dipole moment as all bond lengths are equal and interchangeable. However, as was described above, the III-nitride lattice structure is composed of two interpenetrated sub-lattices displaced with respect to each other along the *c*-plane. Due to the difference in electronegativity of different species, these sub-lattices are charged and thus experience mutual attraction. This attraction distorts the above-mentioned tetrahedrons‡ and makes a non-zero dipole moment. While dipole moments of all tetrahedrons in the bulk compensate (and thus cancel) each other, those at the opposite *c*-plane surfaces remain. These charges present in free-standing III-nitride crystals define their so-called spontaneous polarization. If such a crystal is additionally distorted by applying external mechanical strain the charges will be further modified. This behaviour is known as piezoelectricity.

1.1.2.3 Spontaneous Polarization

For real (non-ideal) structures the *c*/*a* ratio deviates from the ideal value, leading to spontaneous polarization (P_{sp})[27] as was described above. The *c*/*a* ratio for the binary III-Nitride compounds is shown in Table 2. The polarization field can have a value of up to 0.1 C/m^2 in nitride semiconductors[28]. Effectively, these lattice polarisations electrostatically act as two-dimensional lattice charge densities (σ) located at the two sides of the sample with values between 10^{13} and 10^{14} e/cm^2 [28]. This macroscopic polarisation and the associated surface charges induce an internal electric field:

$$E_{sp} = P_{sp}/\varepsilon_0(\varepsilon - 1) \qquad 1\text{-}1$$

*Fig.1.1, P. 3 in Ref. [15]
†Fig.2.32, P. 233 in Ref. [15]
‡Fig.2.33-34, P. 233-234 in Ref. [15]

where ε is the dielectric constant of the material. In GaN and AlN with a polarisation field (P_{sp}) of 0.034 C/cm^2 and 0.09 C/cm^2, respectively this results in a built-in electric field up to ~10^7 V/cm, equivalent to 1 V/nm[28]. The spontaneous polarization increases as the structure deforms from an ideal wurtzite structure[16]. The correlation can be seen from Table 2, as in the case of GaN the difference in c/a – $(c/a)_{ideal}$ is smaller compared to AlN and so the spontaneous polarization constant is also smaller.

Table 2: Ratio of lattice constants of wurtzite GaN and AlN[24].

Binary materials	c/a	$(c/a) - (c/a)_{ideal}$[29]	P_{sp} (in C/cm^2)
GaN	1.626	0.007	0.034
AlN	1.601	0.032	0.09

1.1.2.4 Piezoelectric polarization

As alluded to above, if an external mechanical stress is applied at the interface of a material, the layer becomes strained and the crystal structure deforms, this results in further modification of the spontaneously induced charges. Generally, this kind of deformation occurs at any given heterointerface for example: GaN/AlGaN, AlN/GaN, etc. thin films and/or quantum wells. In this process of deformation, the nature of the strain developed at the heterointerface can be either tensile or compressive. Irrespective of the nature of strain, the piezoelectric polarization at the interface is a function of strain (e.g. in the case of a fully strained material to the underlying layer, of lattice mismatch (Figure 8)).

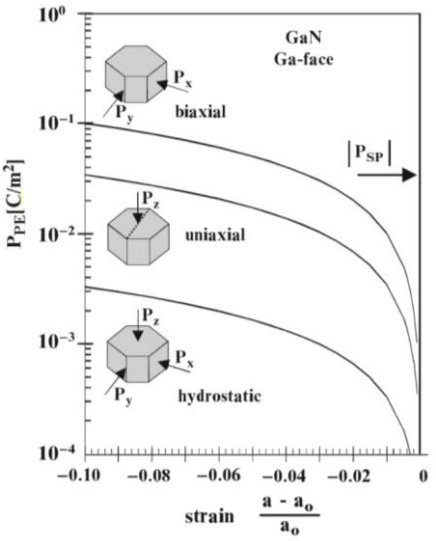

Figure 8 Piezoelectric polarization along (0001) as a function lattice strain of wurtzite GaN at different types of mechanical stress applied.
"Taken from reference [P. 50 in Ref. 16]"

In general, a biaxial compressive stress will reduce the '*a*' lattice parameter and enlarge the '*c*' lattice parameter. Therefore, this change in lattice parameters from the ideal values, will induce a piezoelectric polarization in the opposite direction of spontaneous polarisation, see Figure 9. Furthermore, the tensile stress will decrease

the *c*/*a* ratio, hence piezoelectric and spontaneous polarization would be in the same direction and will result in an increase in overall polarization[29].

In addition to that, there exist crystallographic orientations (planes) which have inversion symmetry intact and do not induce any polarization charges which leads to no polarity in these orientations. For this reason, planes marked as *vertical* (perpendicular to the *c*-plane) in Fig.3 are also referred to as non-polar planes ([11$\bar{2}$0], [10$\bar{1}$0]). Slanted planes (in fg.3) are characterized by reduced polarization and for this reason, are called semi-polar.

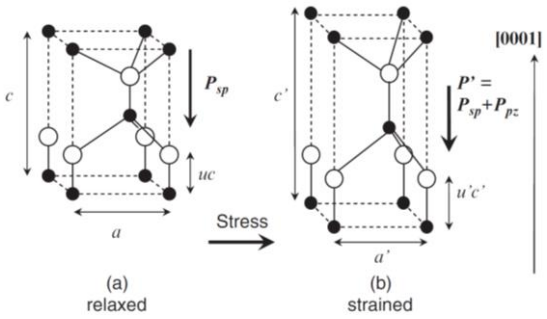

Figure 9 Crystal deformations due to strain induce a variation of the spontaneous polarization. "Taken from reference [P. 473 in Ref. 16]"

1.1.3 Band structure

Another important property of semiconductor materials is the existence of an energy bandgap which separates the conduction band energy states* from the valence band energy states allow for electrons bound to particular atoms, due to which light interaction with carriers is possible. Compounds in which photo-excited electrons can transition from the conduction band back to the valence band without the need for an additional particle (typically phonons) are called direct bandgap semiconductors. All conventional III-nitrides are direct bandgap semiconductors.

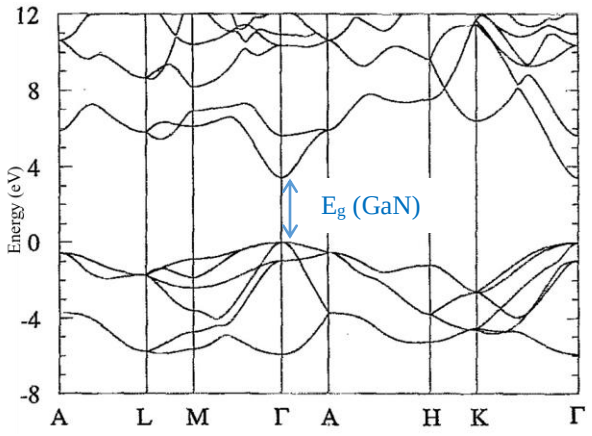

Figure 10 Band structure of wurtzite GaN. "Taken from reference 30"

*In this energy state an electron is free to move in the whole crystal.

1.1.3.1 Band structure of GaN and low aluminium content AlGaN

The band structure of wurtzite GaN is shown in Figure 10 and its corresponding energy gap (bandgap) at the Γ point has been highlighted. It is the centre of the Brillouin zone with zero quasi-momentum ($k = 0$) and this is why no additional particle which carries quasi-momentum is required for nonequilibrium carrier recombination. The value of GaN bandgap at room temperature is ~3.42 eV[30–32] which corresponds to near UV spectral range (~365 nm) and demonstrates positive crystal-field splitting energy, which results in a *standard* sequence of valence bands at the Γ point, i.e. heavy hole (HH), light hole (LH) and crystal field split-off hole (CH) in the decreasing order of energy. The heavy hole band is mainly composed of P_x and P_y characters resulting in the dominant polarisation of light to becomes perpendicular to the *c*-axis (E⊥c)[33] which enables UV LEDs to emit transverse electric polarized light which can escape the active region towards either surface or substrate. This is in contrast to UV LED with high aluminium containing active regions which show the dominant polarisation of light becoming parallel to the *c*-axis (E||c)[33].

The effect of low (≤ 40%) aluminium composition on the band structure of $Al_xGa_{1-x}N$ is important because of our interest in UVA/B LED.

The electronic band structure and valence band ordering at the Γ point of $Al_xGa_{1-x}N$ for Al composition less than 40% is similar to GaN and a band structure of $Al_{0.25}Ga_{0.75}N$ is shown in Figure 11. Liou et al.[34] calculated the band structure using density functional theory with local density approximation (LDA). The electronic bandgap of $Al_xGa_{1-x}N$ at the Γ point is described as a function of aluminium content in the layer and increases with the increase in AlN content.

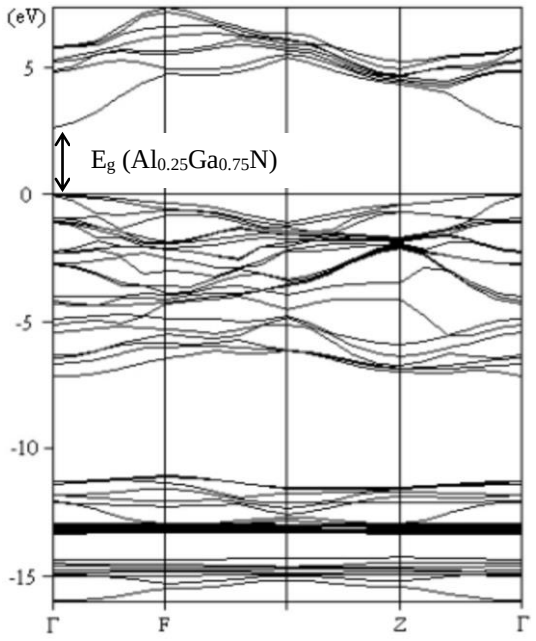

Figure 11 DFT band structure of $Al_{0.25}Ga_{0.75}N$ estimated using LDA approximation.
"Taken from reference 34"

1.1.4 Other properties of GaN-AlGaN material system

An innate property of compound semiconductors is the formation of alloys of two binary materials resulting in ternary compounds. This property opens up new technological possibilities for bandgap and strain engineering in multilayer epistructures. Generally, these epi-structures will consist of one or more layers of binary/ternary compounds of III-nitride material grown using an epitaxial growth technique on foreign substrates, also referred to as heteroepitaxy. The electronic and optical behaviour of these heterostructures is set by the constituting binary and/or ternary materials composition in the layers. So, in the following section, the relationship between the composition of the material and its lattice parameters, and electronic and optical properties are discussed.

1.1.4.1 Dependence of lattice parameters on AlGaN composition

In general, the physical property of a binary semiconductor alloy can be predicted by a linear interpolation between the properties of the constituent compounds at the endpoints. This is true with a high degree of precision for variation of lattice constant with composition as can be seen from Figure 12. This is also known as Vegard's law (equation 1-2).

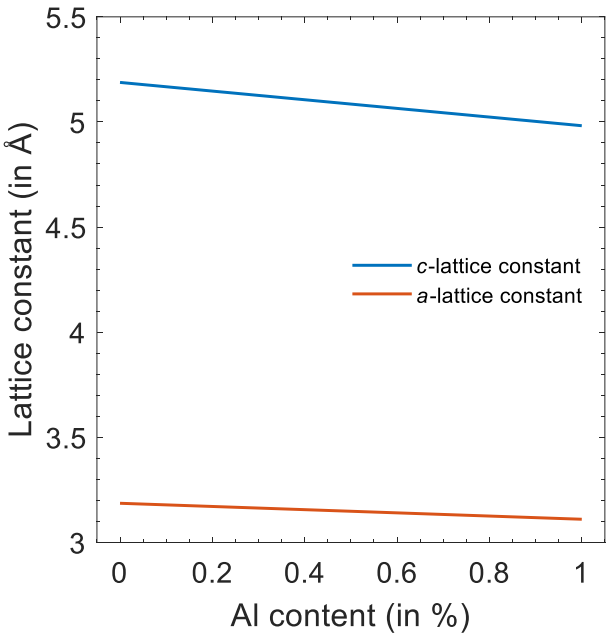

Figure 12 Variation of *c*- and *a*-lattice parameter of $Al_xGa_{1-x}N$ as function of Al content. [P.247 in Ref. *15*]
(Note: Data extracted from[15] and re-plotted)

In the case of AlGaN, the use of linear interpolation is sometimes disputed owing to the large difference in atomic sizes and ionicity of the nitride binaries[34]. The Vegard's law deviation parameters for $Al_xGa_{1-x}N$ are reported as 0.018 Å for the *a* and −0.036 Å for the *c* lattice constant, respectively. We are using basic Vegard's law in this

thesis, assuming the linear variation of the lattice parameter of ternary alloys with composition:

$$a_i^{A_xB_{1-x}N}(x) = x \cdot a_i^{AN} + (1 - \mathrm{x}) \cdot a_i^{BN}, \qquad 1\text{-}2$$

where a_i is the lattice parameter of a crystal direction (*a* or *c*), A and B indicate metals and *x* is composition.

1.1.4.2 Composition dependence of AlGaN bandgap

The value of energy bandgap is not a linear function of Al-composition for AlGaN alloy and deviates from Vegard's law as can be seen in Figure 13. The approximation used to estimate the bandgap of AlGaN is referred to as virtual crystal approximation (VCA): where E_g^{AN} and E_g^{BN} are representing the bandgap values for the two binary compounds with a *composition-independent* bowing parameter of ***b***. The bandgap bowing has been extensively studied[34–40].

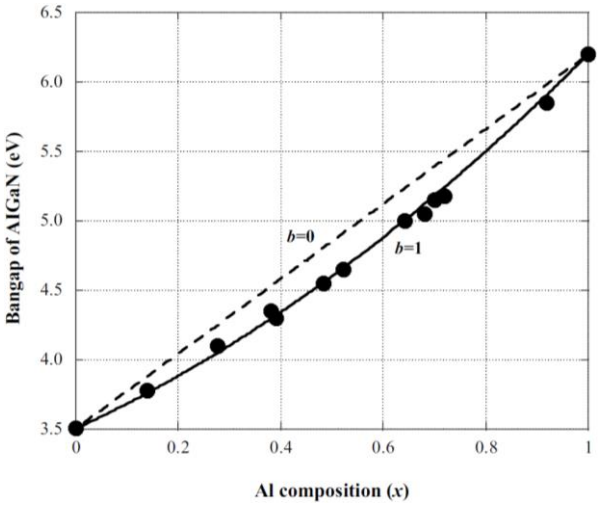

Figure 13 Energy bandgap of AlGaN as a function of aluminium composition (solid circle) fitted with least square function with bowing parameter (b=1.0 eV). "Taken from reference [P. 92 Ref. 15]"

With regards to its great importance to the technology of semiconductors, the behaviour and determination of the bowing parameter ***b*** requires a detailed knowledge of sample quality, precise composition, and strain condition.

$$E_g^{A_xB_{1-x}N}(x) = x.E_g^{AN} + (1 - \mathrm{x}) \cdot E_g^{BN} - \boldsymbol{b} \cdot x \cdot (1 - x). \qquad 1\text{-}3$$

1.1.4.3 Polarization in AlGaN

The ternary compound AlGaN, will also show spontaneous and piezoelectric polarization and the characteristics values will change with composition. The spontaneous polarization of AlGaN is expressed by[41]:

$$P^{sp}_{AlxGa1-xN}(x) = -0.090x - 0.034(1-x) + 0.019x(1-x) \quad \text{1-4}$$

The above expression has factored in a bowing parameter to capture the non-linearity observed in spontaneous polarization[41], as can be seen in Figure 14. In contrast to the spontaneous polarization , the piezoelectric polarization follows a linear function of Vegard's law for ternary AlGaN alloys[41] as can be seen from Figure 14 . It can be expressed by equation (1-5).

$$P^{pe}_{AlxGa1-xN}(x) = xP^{pe}_{AlN}\big(\varepsilon(x)\big) + (1-x)P^{pe}_{GaN}\big(\varepsilon(x)\big) \quad \text{1-5}$$

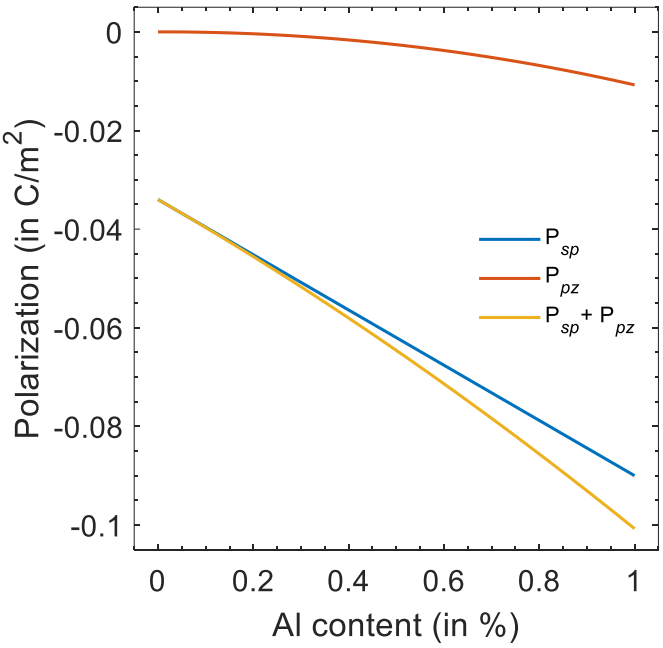

Figure 14 Effect of Al-content of a $Al_xGa_{1-x}N$ layer on different polarizations (Psp spontaneous, Ppz piezoelectric and Psp + Ppz total). Data is extracted from [P. 248, 257 Ref. 15] and re-plotted. Spontaneous polarization is calcaulted from Vegard's law (no effect of bowing is considered). Piezoelectric polarization of $Al_xGa_{1-x}N$ as a function of Al composition is calculated for a material strained to GaN layer.

1.1.4.4 Effect of polarization at GaN/AlGaN interfaces

As discussed previously, the absence of symmetry in hexagonal crystal lattice results in some crystallographic orientations showing polarization while others do not. Lattice strain at these heterostructure interfaces results in a change of polarization (both magnitude and direction) which affects the built-in electric field and can change the effective energy bandgap in quantum structures[42]. An example, of the same is illustrated in Figure 15, where the effect of the built-in electric field on the transition energy of electron-hole in a 5 nm thick quantum well (QW) GaN/$Al_{0.1}Ga_{0.9}N$ heterostructure simulated in the polar (0001) and non-polar(10$\bar{1}$0) direction. The presence of an electric field in the QW reduces electron and hole wavefunction overlap and redshifts the emission wavelength, this needs to be considered in the design of the epi-structure.

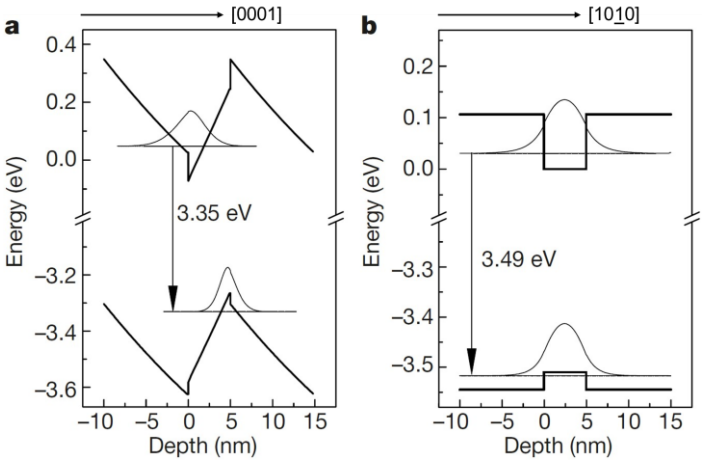

Figure 15 Energy band profile of a single quantum well, with (5 nm GaN) / (10 nm $Al_{0.1}Ga_{0.9}N$) in the direction of a) c- (0001) and b) m-(10$\bar{1}$0) calculated using self-consistent Schrodinger Poisson considering strain and coulombic interaction.
"Taken from reference 42"

1.2 Material and design challenges of a UV LED

In the late 1980s, development in the area of III-nitrides materials and devices was very limited. There was an immense scope for improvement in attributes of material and devices such as quality, morphology, efficiency, etc. Breakthrough in material (epitaxial) growth led to improvement in quality and morphology. This reciprocates to the fabrication of devices with improved efficiency. All in all, improvements in various experimental techniques have contributed significantly to the progress in III-nitrides materials and devices.

This enabled the first realization of III-nitride-based UV-LED[43] in 1999. Since then, UV technology has progressed significantly in material engineering, device design, packaging, etc. In this section, we will discuss the literature on the materials used in device construction and generic device design to build our foundation and understand previous research on UV LEDs.

1.2.1 Generic design and challenges of a UV LED

The structure of a generic UV LED and issues associated with individual layers is shown in Figure 16 and is broadly categorized into seven distinct regions: a) *p*-type doped region; b) electron blocking layer (EBL); c) active region; d) *n*-type doped region; e) buffer; f) template; and g) substrate. Each region can consist of one or more than one layer, with each constituent layer having its unique function in the operation of a UV LED. Each constituent layer poses a unique design/engineering challenge which is also highlighted in Figure 16.

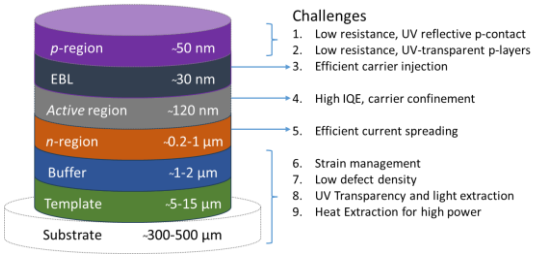

Figure 16 Schematic of a typical UV LED. (showing challenges in the design/engineering of various layers) adapted from the book of III-nitride ultra-violet emitters [P. 5 in Ref. 44] and modified

As stated in the introduction, the key focus area of this thesis is to understand and find solutions for challenges related to EBL (issue 3), *n*-region (issues 5-6) and buffer/template (issues 6-8). However, there are factors such as: a) incomplete ionization of magnesium which limits the maximum achieved hole concentration effectively making *p*-doped region challenging; b) poor light extraction from the bottom surface of a planar substrate due to high refractive index between AlGaN and sapphire resulting in the UV light to be trapped in the substrate reducing the light

extraction efficiency of the overall design. These and various other factors limits the performance of UV LEDs and require significant research attention to understand and solve these problems.

Material quality plays an important role in device performance and efficiency. Conventional III-V devices are typically realized using epitaxial growth technology on native substrates is also referred as homoepitaxy. Native substrates provided lattice and thermal expansion coefficient matching between the epilayer of the device materials and substrate. The prevention of lattice mismatch between the epilayer and substrate helps in avoiding generation of strain and defects in the grown layers. Eventually, this helps the grown epilayer retain/preserve the material quality of the initial native substrate. At this stage, the high quality of the epilayer material reciprocates into the fabricated devices with high efficiency. The various efficiencies associated with a UV LED are discussed below.

1.2.2 Efficiency of a UV LED

Normally, the overall efficiency of an LED device is referred to as the wall-plug efficiency. This is defined as the ratio of total optical power emitted by the device to electrical power applied. The wall plug efficiency is equal to the product of electrical efficiency, injection efficiency, internal quantum efficiency and light extraction efficiency (Figure 17). The definition and further details about various efficiencies can be found in the thesis of Dr. P. Pampili[22]. The state-of-the-art blue LED has 50 times higher wall plug efficiency than a typical UV LED operating in the range of 300-340 nm, this is because all four contributing efficiencies for UV LEDs are less than those for blue LEDs. This begs the question, how can these individual efficiencies be improved? The answer lies in how the individual efficiencies are affected by the functioning of each layer of a UV LED and the respective issues which are limiting their further improvement.

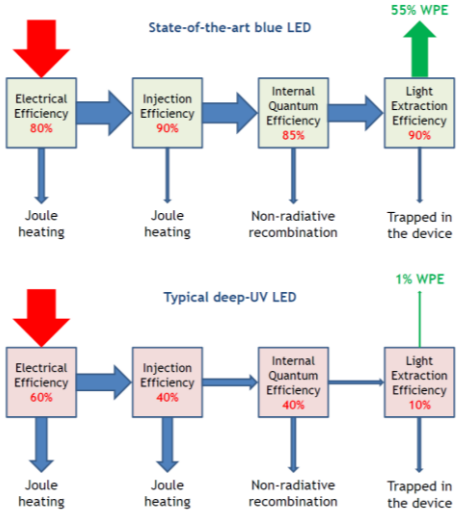

Figure 17 Efficiency comparison of a blue LED and a UV LED.
"Taken from reference [P. 23 Ref. 22]"

In the context of this thesis, it is worth noting that EBL performance affects the carrier injection efficiency, whereas material quality relates to the internal quantum efficiency[45] of a device. Both these efficiency terms require a substantial increase to be able to match the existing blue LED technology.

1.2.3 Epitaxial growth of III-nitride materials

III-nitride materials have a wurtzite crystal structure and are defined by '*c*' and '*a*' lattice constants as discussed earlier in this chapter (subsection 1.1.1). These crystals do not occur naturally, rather are realized in a controlled environment on a bulk substrate with a similar crystal structure using typically high-temperature processes. The process in which the atomic arrangement of a substrate helps to order the atomic arrangement of a newly grown material is known as epitaxial growth. Epitaxial growth also referred to as "epitaxy", is a process in which the underlying crystal structure of a substrate is followed leading to the formation of a single crystalline solid on the substrate. For this process, the grown material and the substrate should have similar lattice parameters in the direction perpendicular to the growth. It is considered[46] that epitaxy can occur only if the lattice mismatch (Eq. (1-6)) is less than ~15%.

$$lattice\ mismatch\ = \frac{(a_e - a_s)}{a_s} \tag{1-6}$$

Ideally, if lattice mismatch is zero between the substrate and the grown epilayer at growth conditions, then defects and imperfections can be avoided and the epilayer is strain-free, this condition is referred to as lattice-matched epitaxial growth. Since the substrate and the material being grown are the same materials then this is called homoepitaxy as shown in Figure 18.

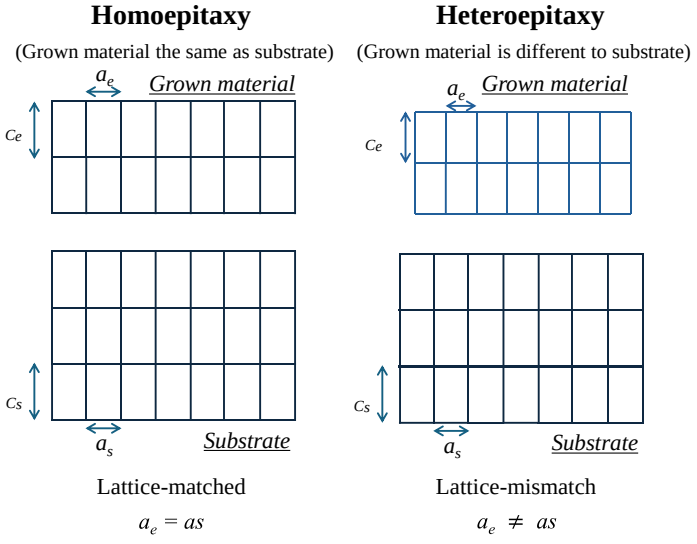

Figure 18 Type of epitaxy depends on the lattice mismatch.

However, if the materials of substrate and epilayer are different then the growth is referred to as heteroepitaxy (Figure 18). In this case, deviations from the lattice-matched condition may occur (except for the rare cases when in-plane lattice parameters of these two materials occasionally coincide) and result in the generation of mechanical strain within the bulk of the epilayer, eventually leading to the formation of defects (dislocations) or material discountities (cracks). The above processes typically are of threshold character i.e. there is a certain amount of strain which material can tolerate. Figure 19 shows examples of possible combinations of grown material and substrate in the case of heteroepitaxy when this threshold is not yet exceeded. If the growth is pursued beyond the critical thickness (corresponding to the above mentioned threshold), the strain which has built up in the lattice finally results in the relaxation of the newly grown layer.

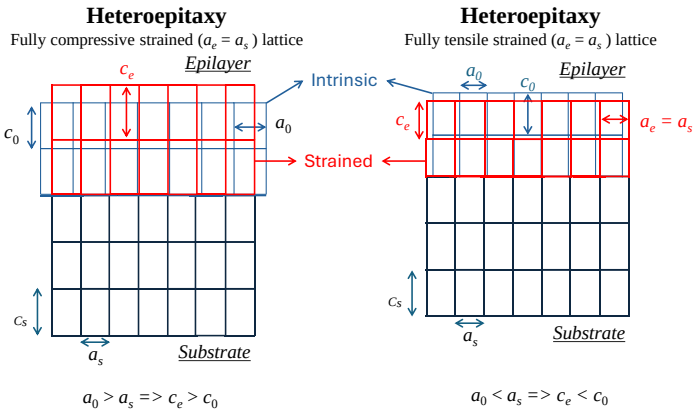

Figure 19 Schematic of a fully strained a) compressive and b) tensile heteroepitaxial film.

If grown material has lattice parameters larger than the substrate then relaxation is not "only" possible through random occurrences of missing half-planes on limited intervals perpendicular to the growth directions (Figure 20, *a*). In the opposite case (when the lattice parameter of the grown material is smaller than the substrate), an alternative way of relaxation can be through cracks. However, if the critical thickness of the crack formation is larger than that of plastic relaxation, then a similar mechanism occurs but through random occurrences of extra-

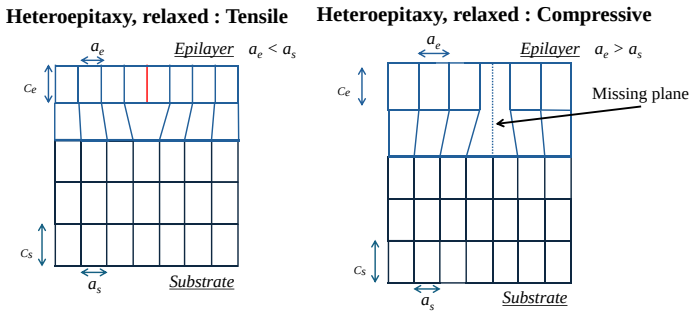

Figure 20 Schematic of a relaxed a) tensile and b) compressive heteroepitaxial film.

half planes (Figure 20, *b*). In both cases of plastic relaxation, ends of the above-mentioned intervals were either missing or extra-half planes occur propagate vertically and become cores of threading dislocations with edge-type components, while the intervals themselves (the horizontal lower borders of the missing or extra-half planes) represent the misfit component of dislocation loop.

In the case of a relatively small lattice mismatch and/or large critical thickness, the strain relaxation can occur via a surface roughening mechanism. The roughening is observed in these features due to the slight tilt in the surface of the individual grains with respect to each other and their coalescence result in formation of a dislocations with screw-component.

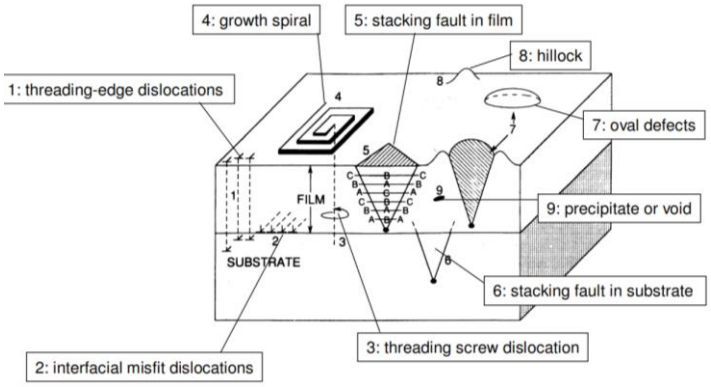

Figure 21: Defects in epitaxial films
"Taken from reference [P. 320 in Ref. 47]"

Rather than mechanical strain-induced ones, other defects can occur in certain circumstances too. Some of them are summarized in Figure 21. They can be of different types such as point defects (interstitials, vacancies, impurities, etc.), extended defects (e.g. above-mentioned dislocations of screw and/or edge type, stacking faults, inversion domains, etc.) or surface features (hillocks, pits, voids, etc.) (P. 320 in Ref. [47]). Some of these defects are observable in the epitaxial growth of III-nitride materials and will be discussed below in more detail.

1.2.3.1 Lattice matching of III-nitride materials

Generally, epitaxial growth is preferred to be carried out on cheap native (bulk) substrates, because it provides automatic lattice and thermal expansion coefficient matching. In the case of III-nitride materials, the available native substrates are expensive, and their usability is limited to a narrow range of alloy compositions. The majority of III-nitride materials alloy compositions suffer from the absence of cheap native substrates due to which epitaxial growth has to be carried out on cheap foreign substrates i.e. heteroepitaxially. This approach however compromises the quality and morphology of the epilayer.

1.2.3.1 Sapphire for III-nitride epitaxy

Sapphire is the most frequently used substrate for the growth of III-nitride materials because of its cost-effectiveness, thermal stability, high crystalline quality, manageable lattice mismatch, and availability in large diameters. The differences in lattice constant and thermal expansion coefficient between GaN and sapphire are shown in Table 3. The mismatch of ~13% is close to the above mentioned empirical limit and results in the columnar nature of the growth. The introduction of an AlN buffer layer[49,50] on sapphire was found to improve the quality and morphology of the GaN layer.

Table 3: Lattice mismatch Δa/a and differences in thermal expansion coefficients Δα/α [P. 399 in Ref. 48]

GaN on substrate	Δa/a (%)	Δα/α (%)
GaN (0001) / Sapphire (0001)	+13.9	-34.2
GaN (0001) / Si (111)	-20.4	+55.3
GaN on buffer layer	**Δa/a (%)**	**Δα/α (%)**
GaN (0001) / AlN (0001)	+2.5	+5.5

The above finding was a major milestone in the area of III-nitride materials and paved the way for the development of a novel pseudo substrate/template (AlN was deposited on sapphire using PVD) which was later pioneered by Kyma Tech. These templates enable improvement in the quality of the grown epilayer, whether it is GaN or low aluminium content AlGaN compared to direct growth of GaN or AlGaN on sapphire. So, for the above reasons, we prefer Kyma Tech. substrates as our standard substrate to grow AlGaN layers, this will be discussed in more detail later.

1.2.3.2 Substrate bending during III-nitride epitaxy

Another consequence of lattice mismatch between substrate and epilayer is that the corresponding mechanical stress results in substrate bending[51]. Moreover, this

bending is associated with loss of thermal contact between the substrate and the substrate holder which consequently impacts the temperature profile across the substrate resulting in undesired in-wafer inhomogeneities in layer thickness and composition. This bending (convex or concave) is dependent on the difference in lattice constant of the material being grown with respect to the substrate and is subject to change upon cooling down (which is defined by the sign of their thermal expansion coefficient mismatch).

1.2.4 Challenges in epitaxial growth of $Al_{\sim 0.2}Ga_{\sim 0.8}N$

In III-Nitride materials alloying is feasible over a wide range of compositions. In principle, this property is very beneficial as it can enable the generation of photons with the desired wavelength from infrared to deep UV. However, in reality, the light emission efficiency of devices varies widely over this large spectral range. Epitaxial growth on the only available expensive single crystal GaN and AlN native substrates can provide us with good quality material in a limited region of the overall compositional range. So, for composition regions where native substrates are unavailable heteroepitaxial growth is pursued which results in poor quality of the material, effectively reciprocating into the inefficiency of the fabricated devices. Although reports[52] suggests that III-nitride devices can tolerate much higher dislocation densities (~10^9-10^{10} cm^{-2}) compared to conventional III-V devices (Figure 22), it is clear that they have a detrimental effect on their performance. For example, calculations by Karpov et. al[45], suggest that the light emission efficiency of the materials can be significantly improved if the threading dislocation density (TDD) was reduced down to ~2×10^7 cm^{-2}.

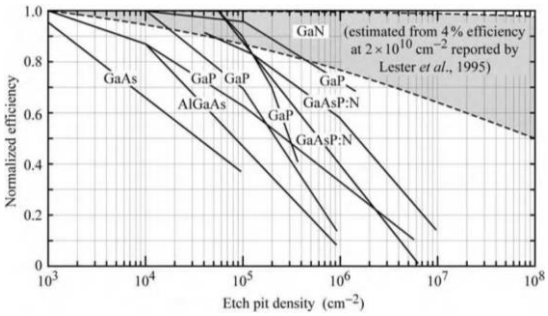

Figure 22 Comparison of III-V and III-Nitride material efficiency as a function of material quality (adapted from F. Schubert) "Taken from reference [P. 231 Ref. 17]"

To achieve the above-mentioned TDD for the realization of an efficient device at any desired wavelength, epitaxial growth should be carried out on native substrates or low dislocation density templates.

After years of development, the only available but still quite expensive native substrates are those of GaN and AlN single-crystal substrates.

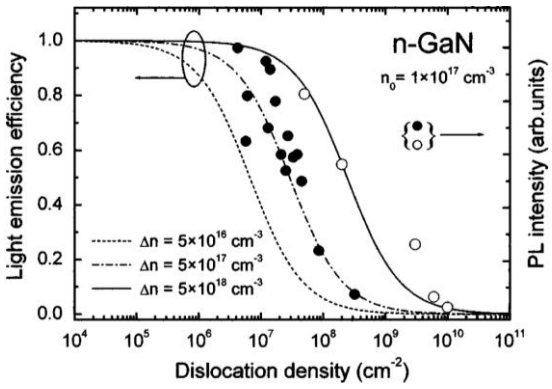

Figure 23 Impact of material quality of a substrate on light emission efficiency.
"Taken from reference 45"

For near UV LEDs, low aluminium content AlGaN is required as a buffer. Epitaxial growth of a *u*-$Al_{\sim 0.2}Ga_{\sim 0.8}N$ buffer layer on GaN native substrate results in cracking due to lattice mismatch (AlGaN a-lattice constant is smaller than that of GaN). On the other hand, growth on AlN native substrate results in poor morphology and/or crystal quality due to strong compressive strain initially and its plastic relaxation later on. Even though high-quality GaN templates on sapphire are available, GaN absorption of the desired UV (~340 nm) light limits their usefulness in the realization of a bottom-emitting UV LED. For this, reason several approaches have been attempted in the literature to achieve a good/acceptable quality of AlGaN on foreign substrates.

1.2.4.1 Template Development: Planar approaches.

Template development can be categorized by the processes followed to realize a buffer layer as planar or a template on a substrate as patterned approach. In a planar approach, direct growth is carried out on the substrate, during the growth (in-situ) various strain engineering and/or dislocation filtering techniques are implemented, whereas in a patterned approach, a pre-grown initial template with poor/moderate quality is patterned using conventional lithography. Overgrowth on the processed template is carried out, this is also referred to as selective area growth.

A planar approach saves time and resources when compared to a patterned approach. However, the enhancement in quality of the template provided by a patterned approach is potentially significantly higher than a typical planar approach.

Understanding and implementing both these approaches can help in maintaining a balance between the development cost and quality of a final device.

1.2.4.2 Buffer (u-AlGaN)

In the absence of AlGaN native substrates, epitaxial growth of the buffer layer is carried out on a cost-effective foreign substrates such as sapphire or sapphire, with a pre-deposited III-nitride nucleation layer (e.g. AlN/sapphire from KYMA Tech.) also known as heteroepitaxy. The downside is the generation of high-density threading dislocations (TDD) (due to plastic strain relaxation) and/or cracking and/or surface morphology deterioration due to lattice mismatch between the two materials. Threading dislocations impede the optical quality[45,53–55] and electrical performance[53] of the material as was outlined above.

1.2.4.3 Current spreading/ Contact layer (n-AlGaN)

The *n*-doped layer in Figure 16, just after the buffer is referred to as the current spreading/contact layer, its function is to inject electrons into the active region. It needs to be crack-free, transparent, and conductive enough for both current spreading and the formation of a low-resistance metal contact. To satisfy the last two requirements, a significant amount of silicon doping (~2×10^{18} cm^{-3}) is required. However, due to the poor quality of the heteroepitaxial AlGaN layers, silicon incorporation into these layers is limited[56] because the high density of dislocations tends to act as compensating centres for the dopant atoms, while further increasing the amount of bi-axial tensile strain[57] in the already strained layers. This strain cumulates with the thickness of the epilayer[58] and eventually results in cracking, to achieve crack-free the thickness of the epilayer is constrained. This constraint on the overall thickness of a current spreading layer hinders the overall conductivity[59] of the layer effectively resulting in current crowding[60] at the contacts. Thus, the above reasons limit the achievable crystal quality of heteroepitaxial *n*-AlGaN layers.

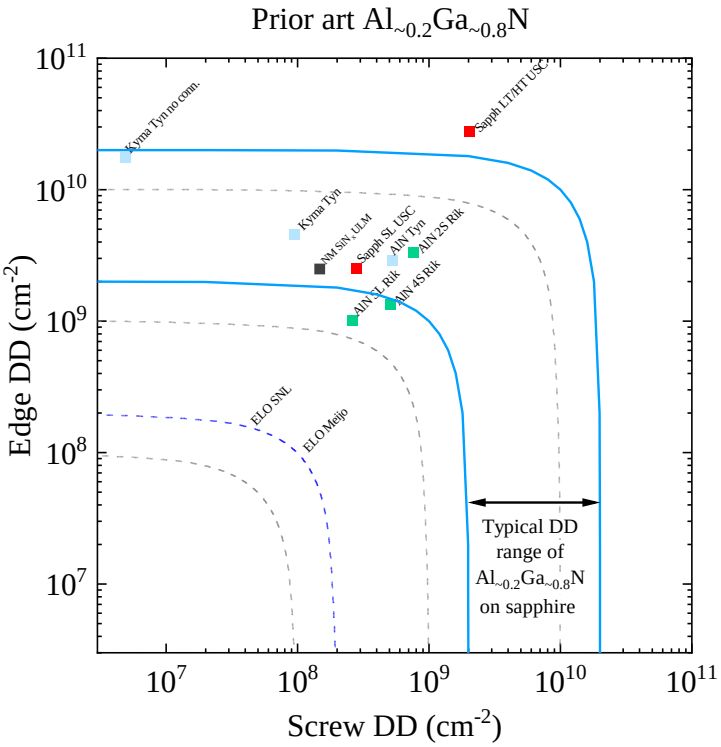

Figure 24: AlGaN (low Al) template quality improvement techniques implemented and resulting dislocation density.
Institutes: Meijo: Meijo University; Rik: Riken; SNL: Sandia National Lab; Tyn: Tyndall National Institute; TuB: TU berlin; ULM: ULM University; USC: University of southern California

In the literature, various techniques have been utilized to prevent cracking and manage strain while attempting to reduce dislocation density such as low-temperature GaN[61] and AlN[62] interlayers, in-situ nano-masking with SiN_x[63], superlattices[64], etc. State-of-the-art crystal quality achieved by different groups using various planar approaches is summarized in Figure 24. This helps us to measure the overall improvement in

template development and compare individual contributions from planar and patterned techniques. Overall, planar techniques were beneficial to some extent in crack prevention and reduction in dislocation density typically down to low ~10^9 cm^{-2}.

1.2.4.4 Template Development: Patterned

According to literature reports[58,65], the quality of typical planar templates achievable by conventional planar approaches is only about low ~10^9 cm^{-2}. However, this is still more than two orders higher than the desired level of ~1-2×10^7 cm^{-2}. It was also observed that *a*-type dislocations contributed ~70-90 % to the total dislocation density[58,62,63,66]. With limited success on planar template development, some radically different approaches have been proposed in the literature involving patterning (on nano- or micro-scale) of conventionally grown moderate quality epilayers, or direct patterning of substrates followed by overgrowth aiming to coalesce patterned structures back to planar layers of hopefully improved quality.

In the earlier days of development, GaN material technology suffered from similar issues of poor material quality, etc. To overcome these issues various patterning and lateral overgrowth techniques were explored. In general, implementation of dislocation filtering techniques by selective area overgrowth through the opening in a mask layer patterned on a base (pre-grown relaxed GaN) template led to substantial reductions in dislocation density[67]. Nonetheless, these techniques cannot be extended to the growth of AlGaN because aluminium adatoms stick to the mask material (typically SiO_2 or SiN_x) resulting in the growth of amorphous or poly-crystalline materials.

Still, Ga-rich AlGaN buffer layers were realized with reduced dislocation density by facet-controlled lateral overgrowth (FACELO epitaxy)[68,69]. This technique combines a) dislocation filtering by using a mask layer and, b) dislocation bending effects by lateral overgrowth of GaN in the open regions forming pyramidal $(11\bar{2}2)$ one-dimensional GaN strips. Then, on these GaN strips, AlGaN is grown, effectively achieving low dislocation density (~1-2×10^8 cm^{-2}) AlGaN templates on which the first UV (~336 nm) laser diodes were realized[70,71]. However, this dislocation reduction strategy cannot be implemented for a bottom emitting UV LED because of the absorption of UV light (below ~365 nm) by the initial GaN epi-layer template limiting its applications.

Thus, maskless µ-patterning combined with two-step AlGaN growth results in the realization of low dislocation density templates. In the first step, a UV transparent relaxed AlGaN/AlN buffer layer grown on a substrate (AlN/sapphire) was employed in which significant material is removed by standard fabrication techniques, the resulting in a template that can be used as a base template for the second step AlGaN overgrowth. In the second step, AlGaN lateral overgrowth is carried out on the fabricated µ-patterned template till coalescence.

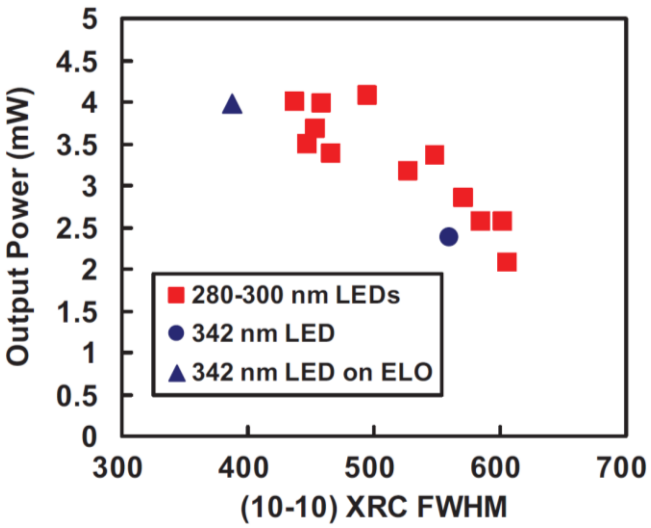

Figure 25 Effect of edge dislocation density of substrate on the light output power of LED devices.
"Taken from reference 53"

Investigation of AlGaN overgrowth by Kueller *et. al*[72] on one-dimensional (strips) µ-patterned relaxed AlGaN/AlN templates resulted in the realization of coalesced AlGaN layer. The author highlights the fluctuation of aluminium content in polar and semi-polar regions which can limit the transparency of a buffer layer this was also observed during growth on 1D GaN strips by Iwaya *et al.*[73]. This report[72] lacks detail regarding growth conditions which result in *c*-plane expansion and quantification of reduction in dislocation density. AlGaN overgrowth on one-dimensional (strips) nano-patterned relaxed AlGaN by Allerman *et al.*[74], successfully realized thick templates with TDD as low as ~2-4×10^8 cm^{-2}. Using this technique reduction in dislocation density was possible due to bending and annihilation of dislocations caused by outward growing semi-polar facets of the 1D (strips) µ-pattern structures.

The principle behind dislocation reduction in all the above pattern-regrow techniques is based on removing a significant volume of dislocated material in the fabrication process and replacing it with laterally overgrown material with lesser or (ideally) no dislocations. However, there can be some circumstances in which dislocations located in the central (core) regions of a µ-patterned template stay frozen

(do not move) and continue to move upward in the direction of growth or dislocations are generated during the coalescence process at the coalesced front. In either circumstance the reduction in total dislocation density is limited. As a consequence non-uniformity in the distribution of dislocation density is observed over the mesa and etched region. Overall, the reduction in dislocation density results in increased power output of a UV LED which can be seen from Figure 25.

Initially, low TDD template development was targeted for the development of laser diodes (LD) which are rectangular (asymmetric) in shape and require lower dislocation densities along the stripe (cavity) length than breadth. So, rectangular shaped µ-patterns were used to pattern and overgrow leading to a reduction in dislocation density along the length of a LD. Additionally, rectangular µ-patterns simplified the easy alignment of lithography masks during device fabrication to the specific low TDD regions with the rectangular shape achieved during epitaxial overgrowth. However, these rectangular µ-structures upon overgrowth result in a non-uniform distribution of dislocation density and strain (i.e. different local strains along the direction and perpendicular to the direction of the rectangular µ-structure/strip), to overcome this issue Allerman *et al.*[74] reduced the rectangular strip width to sub-micron dimensions which resulted in a more uniform TDD distribution over the mesa and etched region. Lateral overgrowth of µ-pattern results in dislocations bending close (~0.25 µm) to the growth surface. This effect is utilized in some of the recent experiments discussed below, where the dimension of µ-structures patterned on the material surface is kept close to ~0.5 µm to promote equal bending of dislocations towards all the growing surfaces.

Some measures were taken apriori to enhance improvement in the quality of the coalesced template such as: maximizing the quality of the initial base template before patterning; while minimizing the volume of the leftover dislocated material after patterning

Further studies of overgrowth on periodic (symmetric) µ-patterned surfaces were conducted to achieve a lowering in TDD and a more even distribution of strain. Typically, a periodic µ-structure with symmetric surface can be geometrical broadly classified into two types: a) convex surface or b) concave surface. Previously, AlN/AlGaN overgrowth on convex µ-structures[75,76] (nanocolumns/ rods) has been focused upon.

Conroy *et al.*[75], achieved AlN nanocolumns with a diameter ≤0.5 µm and, during AlN overgrowth dislocation bending at the growth surface was observed. Meanwhile, these nanocolumns tend to bend (tilt and twist with respect to each other due to preexisting dislocations in their bodies and random distribution within them) during overgrowth, resulting in some generation of dislocations in the process of coalescence. In spite of that, the material quality of the coalesced templates was far superior to the corresponding initial planar reference (base) template.

AlN nanorods of 0.5 µm in diameter realized using nano-imprint lithography were used by Omori *et al.*[76] as templates for Al-rich AlGaN growth. The authors managed to coalesce a triangular array of such nanorods with 1 µm pitch and an improved quality template was realized.

In general, patterning-coalescence techniques have been proven to be more promising, enabling better qualities compared to planar approaches. On the other hand, they require more work and optimization.

1.2.4.5 Electron blocking layer (EBL)

The issue of injected carrier loss[17] from the active region into either *p*/*n*-regions is caused by poor carrier confinement and/or due to distribution statistics (fermi-dirac statistics) of carriers. It severely affects the radiative efficiency of conventional III-V quantum well[77]/double heterostructure based LEDs, and is found to be a function of temperature and barrier height (difference between quantum well and barrier). To prevent, carrier leakage and maximize recombination in the active region strong carrier confinement (typically of several hundred meV, i.e. much larger than kT) is required. If strong confinement cannot be implemented in the design then, alternative approaches such as multi-quantum well structures and electron-blocking layers can be used to address this issue.

Similar issues of carrier overflow from the active region have affected III-nitride LEDs[78]. As in the early days of III-nitride-based visible emitter development using InGaN quantum wells a thin AlGaN cap layer was used after the active region to prevent indium out-diffusion during the growth of *p*-GaN[78]. Its secondary function was to prevent surplus electron overflow from the active region into *p*-regions. This layer was referred to as the electron-blocking layer (EBL) in III-nitride-based LEDs.

Due to its importance later on various works were carried out to optimise its effectiveness as an EBL.

UV LEDs incorporate EBL in between active and *p*-region. Normally, It is a single layer of an intrinsic AlGaN with higher 'Al' content than the last barrier in the active region. The potential barrier generated due to the difference in 'Al' composition between these AlGaN layers is used to prevent, the overflow of electrons from the active region directly into the *p*-region. Suppression of such electrons is important because they recombine (typically non-radiatively) with existing holes in the *p*-region reducing also the hole injection efficiency[78]. An ideal EBL should meet the following requirements: i) optically transparent to the light wavelength emitted by the active region i.e. does not absorb the desired emitted light from the quantum wells, ii) prevents surplus electron flow into the *p*-region and iii) allows easy hole injection into the active region. In recent years, further development and optimization of the electron blocking layer in UV LED has been reported in the literature.[78–81]

A typical AlGaN EBL layer has an 'Al' content difference (with barriers in the active region) of ~10 % and a thickness of ~25 nm. The lower limit of the 'Al' contrast and EBL thickness is determined by the need for the EBL to show a decent conduction band barrier while being optically transparent to the emission from the active region, whereas the upper limit is dependent on the tensile strain generated due to lattice mismatch at the interface of the layer with the last barrier in the active region. These limits constrain the design parameters of an AlGaN EBL implemented in a UV LED. On top of that, it is very complicated to measure the effectiveness of *i*-AlGaN EBL in a UV LED structure as the barrier effect to the surplus electrons is coupled with hole permitting nature of the layer.

To overcome these problems, a unipolar heterostructure (UPHS) which consists of an *i*-$Al_xGa_{1-x}N$ layer sandwiched between two *n*+ GaN regions was designed to study the AlGaN effectiveness as a barrier to vertical electron transport. Previous reports on UPHS by Nath *et al.*[82] and Browne *et al.*[83] question the effectiveness of AlGaN as a barrier. The reason behind this ineffectiveness is related to the compositional inhomogeneity present in AlGaN, due to which carriers tend to seep through the low mole fraction regions, effectively reducing the potential barrier height felt by the carriers resulting in poor rectifying behaviour.

1.2.5 Conclusion

From the above information, it is clear that some issues with near-UV LEDs need to be addressed. The effectiveness of AlGaN as a barrier is questioned as on one hand, it is routinely used in all LEDs (both visible and UV) while on the other hand, literature reports are suggesting that the electron blocking function might not be as strong as expected. In this thesis, this issue will be examined using simulation and experiments in Chapter 3 where the effectiveness of AlGaN as a barrier is studied in detail. In the first section of Chapter 3, a model design used to conduct a 2D simulation of a unipolar heterostructure (UPHS)* is described with the composition of *i*-AlGaN layer represented by three different compositional distribution models, with a specific focus on the random alloy and smeared interface representation because of their uniqueness. Details of the framework followed in the realization of these unique compositional distributions are depicted. Moreover, these models were used to study the thermal and quasi-equilibrium behaviour of AlGaN barrier parameters (such as 'Al' content and thickness). The explanation for the observed behaviour in the simulations is provided and based on this, conclusion have been derived. The conclusion from the simulations was utilized to conduct follow-up experiments on the barrier parameters.

In the second section of the chapter, experimental UPHS samples were grown on *c*-plane GaN templates using MOCVD, followed by fabrication and characterization. The results of our experiments show that there are effects which can influence the effectiveness of AlGaN as a barrier, observed effects within the scope of the experiment are discussed and some other effects which might influence are highlighted. Suggestions helpful for observing the barrier effect of the AlGaN layer are made.

The second issue is the absence of a good-quality template for near UV LEDs, this issue sets our ultimate goal i.e. to improve the quality and morphology of heteroepitaxial AlGaN epilayers while aiming to realize a thick ($\geq$ 2 µm), transparent, conductive, planar *u*/*n*-AlGaN template. There is a general consensus in the literature that conventional planar template development approaches have only limited

* A unipolar heterostructure (UPHS) consists of an *u*-AlGaN layer sandwiched between two *n*-GaN regions

capability in improving the quality of AlGaN layers grown heteroepitaxially. Nonetheless, to understand the limitations of planar approaches, I experimented with some of the known planar approaches (e.g. LT AlN interlayers) previously studied in the literature. I can confirm their limited scope in improving quality. Still, I was able to achieve relatively thick (~1.6 µm) *n*-AlGaN without cracks by implementing a novel composition-graded structure which allowed me to partially compensate for the doping-induced tensile strain with moderate quality. Since realizing the fact that further improvement in quality was not possible using planar approaches, this led us to continue with patterned template development (pattern-regrow approach).

Previously, several techniques based on a pattern-regrow-coalescence approaches have been pursued. However, most of them are too focused on quality improvement while the growth mechanisms leading to particular surface topologies are overlooked. This knowledge gap is part of the focus in chapter 4 of the present thesis. As an additional goal of this study was to understand growth mechanisms and competition between different crystallographic orientations, a structure with a plurality of convex and concave intersections of planes was chosen (µ-honeycomb) as a model pattern.

The details of the fabrication process flow leading to µ-honeycomb patterned templates are provided in Chapter 2 (2.1.5). Furthermore, in Chapter 4 (4.2) optimization of µ-pattern and study of AlGaN overgrowth conditions are discussed in detail. The results in the section are discussed in a three-fold way: a) first optimization of the aspect ratio of the initial µ-pattern to avoid parasitic growth directly on sapphire rather than on AlGaN itself was attempted, b) then the growth parameter space was investigated to find conditions for coalescence of µ-patterns or vice-versa formation of periodic features with crystallographically defined semi-polar microfacets and finally; c) analysis of the surface morphology evolution was conducted to identify the driving forces defining ultimate surface topologies of overgrown patterned structure.

Chapter 2 Techniques and Methods

To achieve the goals of this research, understanding and utilization of several experimental techniques and simulation methods were necessary.

In the first section of this chapter, the relevant experimental techniques, which can be broadly classified into three categories: a) epitaxial growth, b) fabrication, and c) characterization, will be described. In the second section of this chapter, the discussion is focused on the mathematical foundation on which theoretical methods of simulating a real semiconductor device used in this work are based. Further, details about the simulational framework incorporating the above physics of semiconductor devices are also given there.

2.1 Experimental Techniques

Generally, vapour phase deposition techniques such as MOCVD are the preferred way to achieve epitaxial growth of III-nitride material. Various physical attributes of an epitaxial layer are important from a device standpoint. So, these thin films are analysed at various stages using various characterization techniques, and are classified into two categories: a) material and b) device. Material characterisation can be further categorised into in-situ and ex-situ techniques. During growth, material parameters such as layer thickness, its surface morphology and curvature are monitored using in-situ characterization techniques. After growth, the structural quality of the sample is assessed ex-situ using X-ray diffraction. Furthermore, the resulting macroscopic surface morphology is analysed using Normaski microscopy and microscopic surface morphology is measured using a scanning electron microscope. The optical quality of the material is measured using photoluminescence spectroscopy.

After satisfactory results from the material analysis, the optimum growth parameters are used to grow device samples. The material of these samples is characterized and then devices are fabricated. The fabrication process consists of steps: a) spin-coating, b) lithography, c) dry/wet etching and d) metal/dielectric deposition. The fabricated devices are further characterized to extract the device parameters. Device characterization techniques are application-specific and vary for different devices.

2.1.1 Growth

2.1.1.1 Widely used epitaxial growth techniques

Epitaxial growth process technologies can be classified in various ways depending on the vacuum technologies, growth rate, precursors (vapour, metal-organic, salts, etc.), etc. The most frequently used technologies are as follows: metal-organic chemical vapour deposition (MOCVD), molecular beam epitaxy (MBE) and hydride vapour phase epitaxy (HVPE). Stringfellow *et al*. have provided a detailed description of these technologies and compared their respective strength and weaknesses in Ref. [84] (P. 4).

The realization of large-scale GaN bulk single crystals is limited due to the high equilibrium vapour pressure of nitrogen at growth temperatures above 1000°C.

Johnson et al.[85] found that III-nitride materials realized using MOCVD result in superior morphological and device characteristics compared to MBE. Thus, in this research work MOCVD process technology will be used to realize epitaxial growth of III-nitride materials.

2.1.2 Basics of MOCVD

MOCVD derives many concepts and working principles from CVD technology. Some of the most relevant aspects are as follows: transport of desired elements to the reactor is accomplished by the use of volatile precursors; concept of phase transition from gas to solid at the boundary layer in an open reactor*; fluid dynamics studies have helped optimize the aspect ratio and growth conditions (low pressure, effect of carrier gas) of an open reactor to maintain laminar flow† while preventing vortex formation, this results in achieving high flow rate, uniformity and homogeneity of the grown layer [CH. 6 in Ref. [86]].

In summary, all the above insights led to the current operation principles of MOCVD systems. Most of the precursors used in MOCVD growth are volatile (have vapour pressure <150 mbar) metal-organic compounds. They are captured by a carrier gas flown through special containers (bubblers where precursors are normally stored) and delivered to the reactor chamber through a specially designed pipework system allowing switching on/off, control of flow, etc. Upon entering the hot zone of a reactor, precursors undergo decomposition, whereas the products of this decomposition chemically react in the vicinity or on the surface of the substrate thus contributing to growth. The residuals of the above reactions are carried away into the exhaust; the overall process is schematically shown in Figure 26.

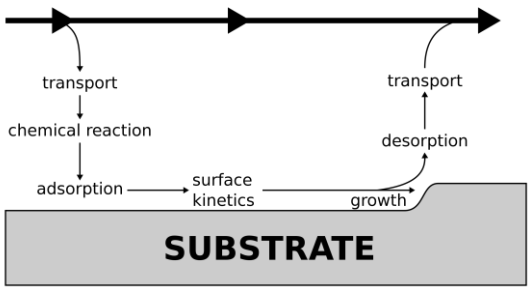

Figure 26: Schematic of steps occurring during a growth process in MOCVD conditions. "Taken from reference 87"

*It is a reactor design in which carrier gas flows continuously from source to substrate, effectively maintaining a difference in the chemical potential between to two, while achieving mass transport. This difference is the driving force of epitaxial growth on the substrate.

†In this type of flow fluids (gas or liquid) follow a smooth or regular path.

The rate of these chemical reactions (on the surface of the substrate) affects the growth rate of the desired epilayer and is dependent on the thermodynamical process parameters such as surface supersaturation*, substrate temperature, rate of desorption and partial pressure. Depending on the rate-limiting factor of these chemical reactions, the growth process can be of two types, i.e. a) reaction-limited (kinetically controlled growth) and b) mass transport-limited.

At low temperatures and large partial pressures of precursors, the transport of adatoms to the surface is fast, while surface reactions are slow; therefore, temperature acts as a "throttle pedal" for the reactions is a rate-determining factor, due to which the growth rate increases with it. On the other hand, at high temperatures and low partial pressure, the limiting factor is the mass transport of the precursors from the source/ambient to the growth surface. Typically, mass transport limited conditions are favoured for the growth of an epilayer in MOCVD.

2.1.2.1 MOCVD of III-nitrides used in this work

Reactor Design

Generally, the design of a growth reactor is classified into a horizontal or vertical reactor depending on the direction of flow of precursors with respect to the substrate surface. The reactor used in this work is a vertical shower-head type manufactured by Aixtron (Figure 27). Various components of the main growth chamber of the reactor are shown in Figure 28:

A) thermocouple is used to measure the susceptor (backside) temperature;

B) tungsten heater is a configuration of three zones that radiatively heat the susceptor allowing for a homogenous radial temperature profile;

C) the showerhead is a water-cooled two-plenum system used to introduce precursors into the growth chamber through a laterally separated array of nozzles;

D) reactor lid is a mount on which various systems and units are placed such as optical ports, in-situ monitoring units, etc.

E) optical ports through which in-situ signals are acquired;

F) showerhead water cooling is where the water is circulated in the showerhead assembly;

*Is defined as a state of dynamic equilibrium in which the chemical potential of the incoming adatoms existing in the metastable (gas) state on the substrate surface is far greater than the adsorbed adatoms i.e. incorporated into the lattice (solid phase).

G) double O-ring seal is used to maintain the low-pressure environment in the growth chamber;

H) susceptor is graphite that is coated with SiC. It has regions defined as pockets for substrates (3 × 2 inches in the used configuration);

I) quartz liner is the piece of "glass" ware whose function is to contain total flow and minimize its contact with reactor sidewalls;

J) susceptor support on which susceptor rests;

K) exhaust removes the residual gases from the growth chamber.

Figure 27: III-Nitride material Aixtron MOCVD reactor housed at Tyndall.

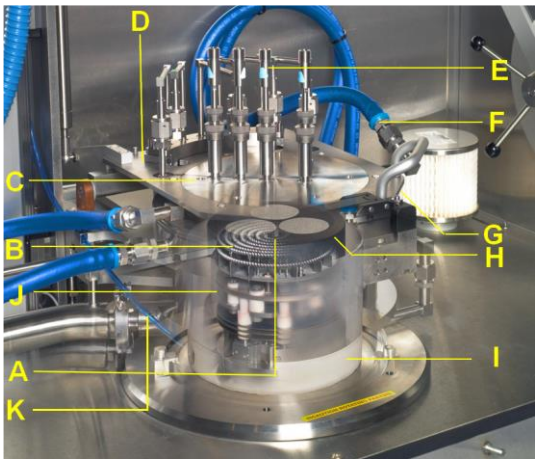

Figure 28: Picture of a cross-section view of shower head "Taken from reference [P. 71 in Ref. 88] "

Sources

The list of precursors used in the growth process of various samples is shown in Table 4. The metal-organic precursors were stored in bubblers and delivered to the reactor during growth. TMGa and TMAl precursors are used as the source for group-III elements. Ammonia gas is preferred as a source of nitrogen over molecular nitrogen because of its high cracking efficiency at standard MOCVD growth conditions.

Table 4: List precursors

Metal organic (MO), Gas (G)		
Precursors	Short form	Bubbler Temperature (°C)
Trimethyl Gallium	TMGa	0.5 MO
Trimethyl Aluminium	TMAl	20 MO
Disilane	SiH_4	G
Ammonia	NH_3	G
Carrier gas	H_2	G

Prerequisites for an optimum epilayer

In general, material parameters (e.g. mole fraction, layer thickness, surface morphology, crystalline quality, etc.) of an epilayer are dependent on more than one MOCVD process parameter (e.g. reactor pressure, substrate temperature, V/III ratio, etc.). Optimization is required to achieve material parameters within the desired range. In the process of optimization of a new material or structure, the starting set of parameters can be arbitrary or depart from the set of parameters known for the nearest previously optimized material/structure. While full details of approaches implemented in this work will be provided in the relevant chapters, here I just briefly present the basis for growth of various types of samples explored.

2.1.2.2 Planar approaches and sample types

An approach is referred to as a planar approach when direct growth of the epilayer is carried out on a flat unpatterned substrate. During such a growth, various in-situ strain engineering and/or dislocation filtering techniques can be implemented. Some such techniques/approaches used in this study are described below.

Substrates used

In this thesis, the most frequently used substrates are: i) sapphire ii) AlN/sapphire (prepared at Tyndall), and iii) 'Kyma' templates. Standard single-side polished *c*-plane sapphire (nominally no miscut) was procured from Cryscore Optoelectronic Ltd. Typical AlN templates utilized in the thesis comprise ~2 µm thick AlN grown on procured *c*-plane sapphire using our standard recipe[89]. 'Kyma' substrates mentioned above are *c*-plane sapphire substrates with a thin (~25 nm) AlN nucleation layer deposited by the PVDNC technique; the deposition of thin AlN on such wafers is procured from and carried out by Kyma Technologies, Inc.

Direct growth of AlGaN

Initially, sapphire and/or Kyma substrates were used to directly grow uniform composition *u*/*n*-$Al_{\sim 0.2}Ga_{\sim 0.8}N$ in standard AlGaN conditions (hydrogen ambient, 1060 °C, NH_3 composed 10% of the total flow (of 8000 sccm)). No particular treatment of substrates was used in this case except for thermal annealing/surface cleaning before the actual introduction of metal-organic precursors and ammonia.

AlN connecting layer

The next approach involved the introduction of an AlN connecting layer before the growth of AlGaN. Three thicknesses have been applied: 100, 200 and 400 nm. Only Kyma substrates were used here. Standard growth for AlN parameters were used to grow the connection layer: hydrogen ambient, 1110°C, 75 mbar, V/III ratio of 25, f_{TMAl} = 60 µmol/min which corresponded to a growth rate of ~0.36 nm/sec. Consequent growth of AlGaN was carried out as described above. The optimal connection layer of 200 nm was used in all subsequent approaches when grown on Kyma substrates.

LT-AlN interlayers

In literature[61,90–95], low-temperature interlayers have been shown to be able to provide better management of tensile strain and improve the crystal quality of the main layer. So, to study whether a low-temperature (LT) AlN interlayer can be of any benefit in our case, two AlGaN samples were grown with an LT-AlN interlayer placed halfway through the AlGaN layer. Growth parameters of the LT-AlN interlayer were as follows: 75 mbar, hydrogen ambient, ~600 °C, V/III ratio 1000 (which corresponds to 2240 sccm of NH_3). The difference between the two samples lies in high temperature (1250 °C) annealing after LT-AlN growth, which was applied for one sample and not for another.

Graded composition

Besides crystal quality and conductivity, another aspect of the buffer layer is its continuity (lack of cracks). As discussed earlier, AlGaN with rather high dislocation density (the case here) is susceptible to cracking when doped with silicon. We have observed a buildup of tensile strain during direct growth of uniform composition *n*-AlGaN experimentally which limits the achievable thickness of crack-free epilayers. To mitigate this issue the following strategy has been tried: when aiming for an ultimate aluminium content in the AlGaN buffer of ~20%, I deliberately deposited an undoped ~30% AlGaN of thickness enough to almost fully relax it with respect to AlN connecting layer first. Then the transition to the final 20% AlGaN was done gradually while doping.

AlGaN growth conditions used

Besides "standard" AlGaN growth conditions, some modifications have been also used. The first one can be referred to as "GaN standard" conditions. In this case, growth parameters typical for GaN growth were used: hydrogen ambient, 1060°C, 150 mbar, V/III ratio of ~1000. While they were found useful in some cases (details in Chapter 4), they were found to be non-optimal from the point of view of the precursor used.

The second modification was based on the previous one, but a pressure of 75 mbar was used instead of 150 mbar. These conditions are referred to as "hybrid conditions" as pressure is taken from the "AlGaN standard" while the rest of the parameters are from the "GaN standard".

Unipolar *n*-GaN/*i*-AlGaN/*n*-GaN heterostructures

To prepare UPHS samples, initially thick (~1.5 µm) *u*/*n*-GaN templates were grown on Kyma substrates. These templates were grown concurrently in one campaign to prevent run-to-run variation of heterostructure in the device design. A unipolar heterostructure consists of an intrinsic AlGaN region sandwiched between two conductive *n*-GaN layers. These samples were grown at a substrate temperature of 1060°C with a V/III ratio at 75/150 mbar reactor pressure. Generally, the GaN regions were grown at 150 mbar pressure whereas the AlGaN regions were grown at 75 mbar to achieve good control of aluminium content. To change reactor pressure, some time is required (cannot be ramped instantaneously). Two strategies were tried: growth paused during the ramp and continuous growth of *n*-GaN during the ramp.

2.1.3 Characterisation Techniques: Material

Most of the grown epilayers were studied during and after growth to assess material parameters such as crystal quality, surface morphology, etc. A sound assessment requires further understanding of the *in-situ* and *ex-situ* characterization tools and their underlying functioning in detail, which are described below.

2.1.3.1 In-situ characterization

During epitaxial growth of an epilayer continuous control of various material parameters (e.g. thickness, morphology, strain) is achieved by *in-situ* monitoring and

characterization of process parameters (e.g. surface temperature, growth rate, curvature) using integrated tools.

In-situ reflectance, temperature and curvature (Laytec Epi-Curve TT)

During epitaxial growth, generally, it is carried at elevated temperatures. In our reactor, material growth rate, surface morphology and stress status are measured by "Epi-Curve TT" software backed up by corresponding hardware. This is an integrated solution consisting of a pyrometer, reflectometer and curvature sensor used to measure the 'true temperature', reflectance and wafer curvature.

The pyrometry uses the intensity of Planck radiation at 950 nm wavelength.

The LayTec reflectometer acquires in-situ data at three different wavelengths: 405 nm, 633 nm and 950 nm. They are used to analyse growth rate (from the frequencies of fabry-perot oscillations occurring due to interference of beams reflected from substrate/material interference and growth surface) and surface morphology evolution (from the average value of reflectance i.e. ignoring fabry-perot oscillations).

The measurement of wafer curvature is carried out by shining two parallel laser beams on the substrate surface and imaging their reflections onto a CCD camera. The in-situ curvature is then calculated from the distance difference between the two spots: as the spots go apart from each other if the wafer is convexly bowed and vice-versa they go closer to each other for concave bowing of the wafer.

Argus

The uniformity of epilayer thickness across a wafer is linked with temperature uniformity in the radial and axial directions. While radial homogeneity is secured by susceptor rotation, axial homogeneity requires fine-tuning of three-zone heater relative intensities. To do this Argus unity is used which has six pairs of photodiodes positioned along the susceptor radius. With susceptor rotation, Argus allows for the *in-situ* generation of a thermal map of the carrier surface with a resolution of 0.1°C (achievable with calibration using a blackbody radiation simulator).

Further analysis of various aspects of an epilayer post-growth is accomplished using *ex-situ* characterization techniques.

2.1.3.2 X-ray diffraction

As mentioned in Chapter 1, the heteroepitaxial growth of III-nitride material results in the generation of mechanical strain in the film and as a result of its plastic relaxation dislocations are formed. After the initial relaxation, some residual strain might still exist in the partially relaxed epitaxial film. Knowing this residual strain is necessary for example for the estimation of the composition of ternary compounds.

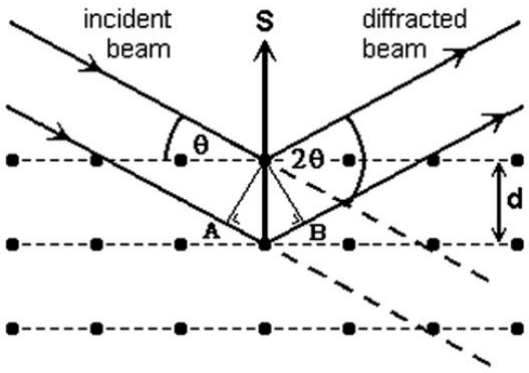

Figure 29: Schematic of Bragg's law of diffraction. "Taken from reference 18"

In this context, a non-destructive technique which has been extensively employed to study the composition, strain status and structural quality of grown material is X-ray diffraction. This crystallographic technique is governed by Bragg's law of diffraction (equation 2-1), which relates the angle of diffraction (θ) of an X-ray beam with wavelength (λ) and the spacing between two parallel planes (d_{hkil}) in a crystalline material (in our case III-nitride material) as shown in Figure 29.

$$2d_{hkil}sin\theta = n\lambda \qquad 2\text{-}1$$

Generally, the wavelength of incident X-ray photons is 1.54 Å also referred to as Cu_α. These are generated by bombarding electrons on a metal (in the case of Cu_α line it is obviously copper) and the wavelengths with the highest monochromaticity are selected and directed towards the sample under study. The atomic arrangement of the crystal lattice of a material acts as a three-dimensional diffraction grating in which the incident X-rays undergo coherent elastic scattering (diffracted) by the atomic electron cloud. Constructive interference between these diffracted/scattered x-ray beams occurs at specific angles

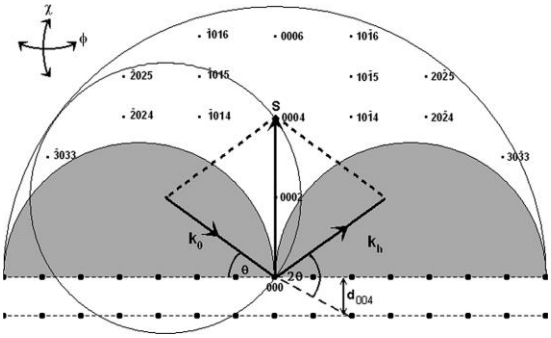

Figure 30: A section through reciprocal space for an [0001]-oriented GaN film. (Sample is at origin) "Taken from reference 18"

i.e. when the path length is an integral multiple of the incident wavelength (equation 2-1). Each set of crystal planes in the real space (Figure 29) is Fourier transformed into diffracted spots (Figure 30) in the reciprocal space. The position and shape of a diffraction spot are inversely related to the interplanar spacing (d_{hkil}) of the crystal planes. The above description is based on a so-called kinematical theory* which is adequate for this discussion. There is a very broad literature available which has covered the structural characterization of III-nitride materials using X-ray diffraction. However, my accumulated knowledge in this area is mostly from the review article of Moram *et al.*[18] which has covered the fundamentals and instrumentation in regards to this topic. Nonetheless, more information on this matter can be acquired from Kidd's book.[96]

At this point, to gain insight into a material crystallographic nature, it is important to introduce the conventional nomenclature of various angles concerning the sample, source and detector shown in Figure 31. These angles are known as a) Omega (ω), which is the angle between incident X-ray beam and sample surface; b) two Theta (2θ), is the angle between the original direction of X-ray beam and its diffracted part; c) Phi (φ), is the rotation angle of sample with respect to normal to its surface; and d) Chi† (χ), is the angle between normal to the sample surface and plane within which both incident and diffracted X-ray beams lie.

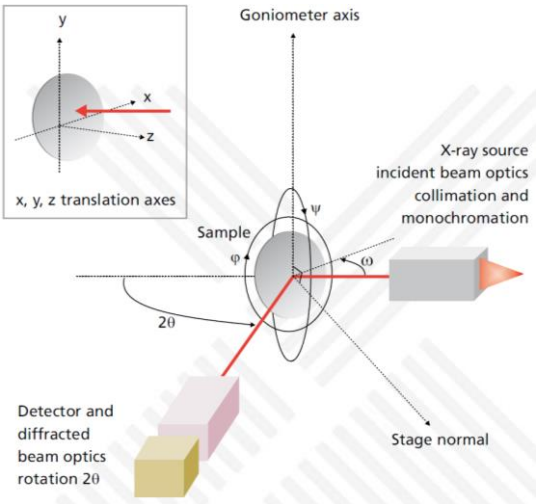

Figure 31: Schematic of various angles and key components of a diffractometer "Taken from reference 96"

Usually, all the diffraction spots seen in Figure 30 represents specific crystallographic (direction) planes with respective ($hkil$) and are further assessed using 1D scans: a) $\omega - 2\theta$ (or $2\theta - \omega$ which are essentially the same) scans, b) ω-scans, etc. These scans are also called rocking curves (due to the rocking nature of the sample being measured).

* This theory breaks at low angles and for highly perfect samples.
† This angle is marked as Psi (Ψ) in Figure 31.

In an $\omega - 2\theta$ (or $2\theta - \omega$) scan, the detector position (2θ) is changed in a step of $\delta 2\theta$ which has twice the value of the change in incident beam angle (ω), i.e. $\delta(2\theta) = (\delta 2\omega)$. This results in a radial movement in the diffraction space and provides information regarding the interplanar spacing of the chosen crystallographic orientation, which can be useful in assessing the material of layers composing the studied sample.

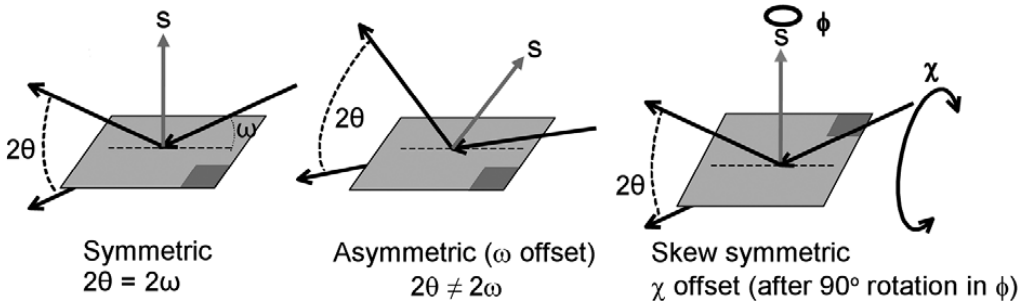

Figure 32: Possible diffraction geometries. "Taken from reference 18"

It is understood that due to the design of a standard diffractometer, not all the planes are equally accessible for $\omega - 2\theta$ scans in a particular orientation of detector and source i.e. the regions greyed out in Figure 30 are not visible to the detector. So, the orientation of the detector and source needs to be changed to study inaccessible planes of a material (e.g. $1\bar{1}01$, $11\bar{2}2$ of III-nitrides) using various types of geometry. Some of the extensively used diffraction geometries are shown in Figure 32: a) symmetric ($\theta = \omega$; $\chi = 0$), b) asymmetric ($\theta \neq \omega$; $\chi = 0$) and c) skew-symmetric ($\theta = \omega$; $\chi \neq 0$).

In a standard ω-scan measurement in an arbitrary geometry, the source angle of incidence (ω) is varied in the diffraction plane while the diffracted signal is measured by the detector positioned at the fixed scattering angle (2θ) relative to the incident beam. The physical significance of a ω-scan is that, it shows parallelity of planes contributing to the constructive interference of X-rays.

The main mechanism affecting the parallelity of crystal planes in III-nitride epilayers is the presence of dislocations. Particularly, screw-type dislocations affect the parallelity of basal crystal planes (parallel to the *c*-plane). For this reason, information about screw-type dislocation densities can be obtained from the ω-scan of symmetric reflections (0002), (0004), etc. Likewise, edge dislocations will disturb the parallelity of planes perpendicular to the basal plane (i.e. *m*-plane, *a*-plane, etc.).

As seen from Figure 30, these planes are inaccessible in either geometry as the incident beam has to hit the sample parallel to its surface. For this reason, slanted planes ($\{10\bar{1}2\}$, $\{1011\}$, etc.) are typically used for edge-type dislocation density estimation.

The strain state of a sample (e.g. a heterostructure or an LED device material) cannot be assessed by a single one-dimensional scan if the composition of individual layers is not known. A combination of symmetric and asymmetric or skew-symmetric allows in principle to determine both the composition and strain status of a layer in a multilayer stack. Although the overall approach is quite complicated,[97] its advantage is that it allows quantitative independent determination of composition and strain. A simpler visual (and thus in general case only qualitative) analysis of strain can be done using so-called reciprocal space maps (RSM).

To plot a reciprocal space map, a two-dimensional (2D) scan of asymmetrically located diffraction spots is conducted along two axes of measurements (with one axis being typically $\omega - 2\theta$ scan taken at different ω-offsets). The collected 2D information is available in angular units but can be replotted in coordinates of the diffraction vector (Q_x along the *x*-axis, Q_y along the *y*-axis) which are proportional to the inverted in-plane and out-of-plane lattice constants respectively (which explains the name of such representation of XRD data – RSM). As clear from the above, in an RSM, materials having the same Q_x values have the same in-plane lattice parameters and therefore either lattice-matched or fully strained to each other. On the other hand, if a material undergoes relaxation, then its Q_x value drifts away from that of the layer on which it is grown. Such a layer is not "vertically aligned" to the underlying layer and thus is at least partially relaxed. The exact formulas for $Q_x(\omega, \theta)$ and $Q_y(\omega, \theta)$ are broadly available in specialized literature and can be found for example in previously mentioned Kidd's book (P. 77-78, Ref. [96]).

To get full information about a sample a certain set of crystallographic directions has to be studied. For *c*-plane III-nitrides, to get information about *c* lattice parameters a symmetric scan needs to be taken e.g. (0002), (0004), etc. For *a* lattice parameter, an additional asymmetric or skew-symmetric scan is required as one needs an interplanar spacing of a plane at an (ideally large) angle towards the *c*-plane. In this work, I have studied the following directions: [0002] (symmetric), $[1\bar{1}01]$ (skew-symmetric) and $[1\bar{1}05]$ (asymmetric) as these specific planes have relatively large intensities and are enough to analyse the quality, composition and strain in the studied

material. Reciprocal space mapping can be conducted for all the above-discussed geometry, but the most informational is along [$1\bar{1}05$] as this asymmetric measurement captures the relaxation of the epilayer relative to the underlayer/substrate. [P. 7 Ref. [18]]

The equipment used in this study is a PANalytical X-ray triple-axis diffractometer shown in Figure 33. One-dimensional (1-D) scans were conducted using a gas (Xe) detector mount, while 2-D maps were constructed using a PIXcel3D (solid-state hybrid pixel detector) instrument.

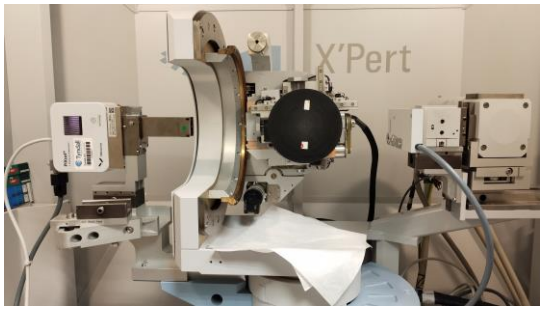

Figure 33: Picture of our X-ray diffraction setup

As discussed above, the broadening of a diffraction spot can be used to obtain the full-width half-maxima (FWHM) of a ω-scan which for epilayers encapsulates information regarding dislocations in them. Typically, a narrow FWHM is always desired for an ω-scan, as it is attributed to large grain size and thus the presence of fewer densities in threading dislocations of a particular type.

Overall, the intensity of collected photons for a respective crystallographic direction (*hkil*, where $i = -(h + k)$) is a function of various parameters such as the position of a sample (x, y, z coordinates), incidence angle (ω), diffracted angle (2θ), etc., and the signal to noise ratio is maximized for all the above parameters. To determine the composition of an epilayer from the measured $\omega - 2\theta$ data, simulation using commercial simulation software (Xpert) is carried out which is based on full dynamical theory.

In this work, the screw and edge dislocation density is estimated from the FWHM of ω-scans, β. As was mentioned previously screw dislocations affect the parallelity of basal planes and therefore the density of dislocations with a screw component N_{screw} can be assessed by analysis of ω-scans measured along symmetric reflections (0002, 0004, etc.). The following formula is applied, assuming the case of a random distribution of dislocations:

$$N_{screw} = \frac{{\beta_{0002}}^2}{4.35\, b_{screw}^2}, \qquad 2\text{-}2$$

where FWHM β_{0002} is given in radians and b_{screw} is the Burger's vector, which for screw-type dislocations is equal to the c lattice parameter, which needs to be

presented in centimeters for N_{screw} to be in cm^{-2}. Similar to the (2-2) formula can, in principle, be used for estimating the density of dislocations with the edge component N_{edge}:

$$N_{edge} = \frac{\beta_{1\bar{1}00}{}^{2}}{4.35\, b_{edge}^{2}}, \qquad 2\text{-}3$$

where b_{edge} is Burger's vector for edge-type dislocations which is equal to a-lattice constant. However, as was mentioned above for standard *c*-plane samples, the *m*-plane is not directly accessible. For this reason, an inclined skew-symmetric reflection is used in this work (and thus $\beta_{1\bar{1}01}$ instead of $\beta_{1\bar{1}00}$ in (2-3)). This approach lacks accuracy as both screw and edge dislocations contribute to the value of $\beta_{1\bar{1}01}$, but since our samples are typically dominated by edge type dislocations for simplicity, it was considered acceptable for qualitative comparison between similar type samples.

Assessing material quality by measuring the FWHM of the ω-scan is not only affected by the presence of dislocations but also by various other factors such as: width of broadening present in an instrument, intrinsic rocking curve width of the crystal, lattice strain at dislocations (micro-strain), limited correlation lengths and wafer curvature. These factors can introduce error in the accurate estimation of quality using XRD. So, a sample was measuring multiple times to determine the spread introduced due to instrument and over the sample, since these two factors are coupled and it is hard to separate them.

This value of the spread was assumed, to be constant for all the samples and so the same was applied to all the reported FWHM values measured using the XRD system.

2.1.3.3 *Scanning Electron microscopy (SEM)*

In scanning electron microscopy, an image is formed by rastering a sample surface with electrons that are accelerated (inside the column) in a vacuum by an applied electric field. Rastering is realized by an electric field applied perpendicular to the direction of accelerated electrons. These accelerated electrons upon interaction with the sample surface results in generation of different of radiation shown in the Figure 34. Depending on the requirement of the study specific detectors are integrated with the SEM configuration to investigate different attributes of a specimen. The two most commonly used detectors are based on secondary electron and back scattered electron detection. The main difference between these two types of signals is that the former is acquired from a larger volume and provides information regarding composition, presence of different phases and crystallography to the sample whereas the latter is generated near to the surface of the sample and has extensive information regarding the topography of the sample.

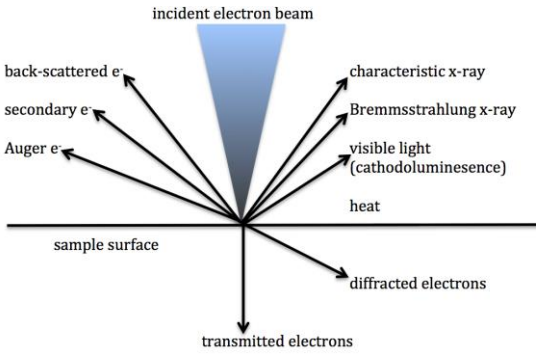

Figure 35: Sample surface interaction with electron beam.[98]

In this work, the secondary electrons generated from our sample were used to study the sample surface as these are generated close to the surface of the sample. The interaction volume of these accelerated electrons is dependent on factors such as accelerating voltage, material density, etc. Typically, in nitride materials the depth of penetration can be anywhere from ~100 to 200 nm from the top of the sample surface. This help in construction of a clear picture of the topography of the sample surface. This technique is best suitable for conductive

Figure 34:Image of a column of SEM Zeiss Supra 40

samples, as being irradiated with electrons, an insulating surface charges and disrupts the normal incidence of new electrons, resulting in a distortion of the acquired images.

Zeiss Supra (Figure 34) and Quanta FEI were used to study the microscopic features and topology of various planar or patterned surfaces. The images acquired by Zeiss were constructed by equally mixing signals (50:50) from the inlens detector and the secondary electron detectors.

2.1.3.4 Nomarski Interference Optical Microscope (DIC)

Optical microscopy utilizes an adjustable combination of lenses which is used to generate a magnified image of the surface. It is beneficial to study macroscopic features (such as hillocks, cracks, etc.) on the surface of interest using optical microscopy as it is the simplest and fastest way to examine the surface morphology of prepared samples. There exists more than one variation or modification to the basic optical microscope design scheme, with each having unique features to offer. Here we used the differential interference contrast microscopy[99] technique also known as Nomarski microscopy.

The Nomarski optical microscope works on the principle of interference of white light. Initially, the white light is split into two components by a wollaston prism, these two components are incident on the material surface and are combined by another wollaston prism at the collection optics. The interference between the two components of the combined light is dependent on the path difference created due to surface features and the angle of the receiving prism. This provides information regarding the depth of a material. In this work, a Nomarski microscope from Olympus (Figure 36) was used in standard mode to analyse the surface of planar samples.

Figure 36 Normaski microscope

2.1.4 Optical Characterisation

Not only microscopy but photons emitted as a result of spontaneous recombination of non-equilibrium carriers can also be utilized to characterize III-nitride semiconductors, owing to the direct nature of the energy band gap. In general, ways of generation of the non-equilibrium carriers define the type of luminescence e.g by light (photoluminescence), by electric current (electroluminescence), by temperature (thermoluminescence), by electrons (cathodoluminescence), etc. Among these, photoluminescence is the simplest type of luminescence, and was used in this study.

In photoluminescence, a high energy photon (greater than the energy bandgap of being tested semiconductor) incident to the sample generates an electron-hole pair with their total energy equal to that absorbed photon. Such hot (having excess energy) carriers very quickly (on the order of ~1 ps) lose it through the interaction with the lattice generating phonons, the process known as thermalization. Recombination of such thermalized carriers produces thus photons that are characteristic of the studied material rather than the excitation source used to excite them. This characterization technique can be utilized to study various material properties e.g. bandgap of the semiconductor, emission from impurity/defect states, localisation of carriers, etc. Additionally, this is a non-destructive method of analysis which allows sample reusability.

2.1.4.1 Photoluminescence Spectroscopy

In this work, diode pumped solid state laser with passively Q-switching from CrysLaS (Figure 38) was utilized to excite the samples for the assessment of their optical quality. Since, III-nitrides are direct bandgap materials, photo-excited electrons and holes can recombine quite efficiently as they do not need a third particle for quasi-momentum conservation (the case in an indirect semiconductor where electrons and holes are thermalized into the corresponding minima of different Brillouin zones). As was already alluded to, recombination of these electrons with holes results in the emission of photons characteristic to the bandgap of the material and thus is referred to as near band edge (NBE) emission. The NBE emission is useful in determining the energy bandgap, degree of compositional fluctuations, Stoke's shift, optical quality of the studied thin film, etc. As the optical quality of an epilayer is directly associated with the density of dislocations in the material[45,53], it is insightful to correlate it with structural quality estimated for example by XRD.

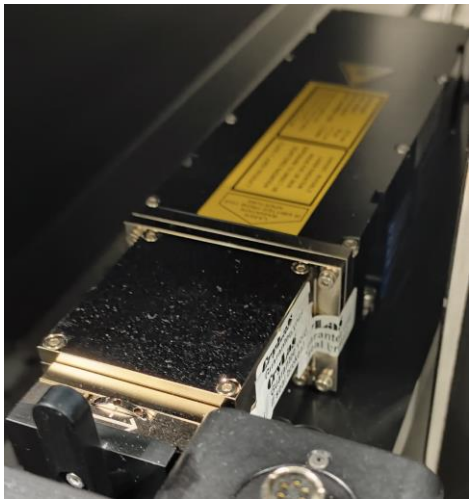

Figure 38 Picture of pulsed 213 nm emitting laser from CrysLaS (FQSS 213-Q).

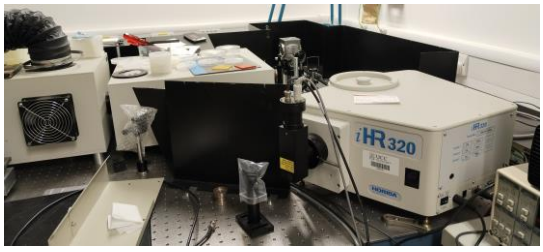

Figure 37 Photoluminescence setup

In my experimental setup, using a pair of convex lenses, sample emission was initially collimated and then focused on the entrance slits of an *i*HR spectrometer (Figure 37) equipped with a charge-coupled device-based matrix (multiple channel detector). Further details on the design and the instrumentation of this photoluminescence setup have been provided in Sahab Norouzian's thesis (P. 78-79, Ref. [21]).

While there exist multiple variations of PL measurements (i.e. temperature resolved, time-resolved, excitation power density resolved, excitation wavelength resolved, etc.) here only standard room temperature PL was used.

2.1.5 Fabrication of µ-patterned structures and UPHS devices

In addition to planar techniques for the growth of *n*-doped buffer AlGaN layers described above, a number of experiments were carried out on the overgrowth of patterned on micro-scale samples. To prepare them as well as UPHS devices, several standard fabrication techniques were used: dielectric sputtering, resist spin-coating, optical lithography, e-beam metal evaporation, inductively coupled plasma (ICP) dry etch, and wet etch. These will be briefly described below.

The project fabrication team comprises of Dr V. Zubialevich and Peter Milner worked on the fabrication of the below mentioned µ-structures, with most work conducted by Dr V. Zubialevich and with some contributions to the process development by my colleague Peter Milner. The fabrication of unipolar devices were done by Peter Milner.

2.1.5.1 Techniques used for fabrication:

Dielectric deposition

SiO_x or SiN_x were used as a cap layer. They were either sputtered or formed using plasma-enhanced chemical vapour deposition (PECVD). Typically, the thickness of these layers was approx. 50-100 nm. The sputterer from Oxford-PVD and PECVD from Sentech tools were used for their deposition respectively. This was typically the first step in the µ-HC fabrication process.

Resist spin-coating

For forming homogenous layers of photoresists (PR: LOR-3A and S1813 were used in this study), a standard spin-coater was used. For both resists, the rotation speed of 4000 rpm and time of 50 seconds were used. LOR-3A was baked for five minutes at 180°C and S1813 was baked for 90 seconds at 115°C. Before spin-coating, to secure good resist adhesion, an adhesion promoter (HDMS) was used for five minutes at 120°C.

Optical lithography

Post bake sample was subjected to exposure to UV light for 6-9 seconds. Optical lithography was carried out using an MA6 mask aligner. Suitable optical masks were used for µ-HC structure and UPHS devices. Post-exposure, development in MF-319 developer was carried out for 35-60 seconds to translate the optical mask into the resist. Samples then were thoroughly rinsed in deionised water and dried using a nitrogen gun.

Metal evaporation (E-beam evaporation) and resist lift-off

A metal stack of Ti (20 nm)/Al (170 nm)/Ti (50 nm)/Au (50 nm) was evaporated using electron beam evaporation (Temescal FC2000 E-Beam evaporator) to form an as-deposited ohmic contact layer on the etched *n*-GaN layer (top and bottom) for UPHS devices.

For µ-HC structures, different metals were tried (Ni, Pd, Au) as a hard mask layer. These layers were deposited using the same tool before or after optical lithography as will be explained later (different approaches were tried). In the latter case, the samples were then subjected to a lift-off process in 1165 resist removal for several hours at 90°C followed by rinsing in room temperature isopropanol alcohol and deionized water.

Inductive coupled plasma reactive ion etching (dry etch)

Two pieces of equipment were used for dry etching: Synapse etcher for dielectrics (SiN_x or SiO_x) and Oxford Cobra for III-nitrides. Standard previously optimised recipes were used for both. In the case of dielectrics, an SF_6 and C_4F_8 based chemistry was used, and Cl_2 based one was used for III-nitrides. In the latter case, it was found that enhancing of thermal contact of the sample with the carrier wafer (by placing a special vacuum oil in between) has detrimental effects on the verticality of the sidewalls and thus no oil was used in the optimised procedure.

Wet etch

Since one of the etch mechanisms in the above described dry etch is physical removal by bombardment with energetic ions, the material suffers from undersurface damage. This needs to be removed by another method which is much more gentle in terms of this sort of damage. Wet etch is a good way to achieve this. In this study, a

commercial KOH-based solution (AZ400K) was used. Since III-nitrides are known for their general chemical stability, the above-mentioned solution at an elevated temperature of ~80°C was used. Even under these harsh conditions the etch is strongly anisotropic with *c*-plane and non-polar planes being effectively unaffected which results in its self-limiting nature, especially for structures with concave geometry. For this reason, hexagonally shaped µ-patterns with {X0$\underline{X}$1} oriented (nearly vertical as X is typically more than 5) sidewalls were obtained upon wet etch.

2.1.5.2 Fabrication of µ-HC structures

Process workflow of fabrication of µ-patterned templates

A general workflow of the fabrication process followed in the patterning of the initial base template to the template with µ-patterned (honeycomb) structures[100] is shown in Figure 39.

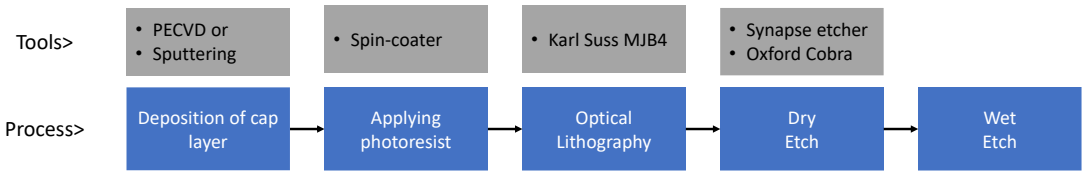

Figure 39: Schematic of the fabrication process flow of µ-HC structures.

Various iterations of this workflow, particularly its evolution to the optimised form that eventually was used for the majority of experiments in this study will be explained next.

Iteration 1. – AlN µ-HC

As a first attempt to fabricate µ-HC structures ~2 µm-thick AlN on sapphire templates with moderate quality were used. The exact workflow in this case was as follows:

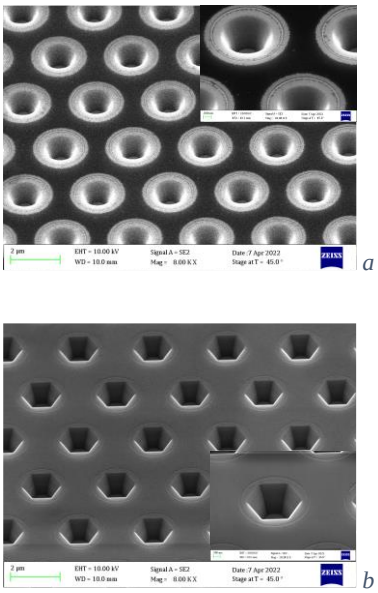

Figure 40: Bird-eye view SEM of a) µ-HC structure after dry-etch and resist removal (residuals of LOR give darker contrast) and b) after additional wet-etch in room temperature AZ400K for 5 min.

1) Spin coating of the PR pair (LOR3A + S1813) was carried out on as grown surface, and the resist underwent a pre-exposure bake as described above.
2) The sample was then exposed to UV radiation with a mask containing circular openings (with a diameter of 1 µm and pitch of 3 µm) followed by the development, which translated the mask into the resist.
3) An ICP-RIE dry etch was carried out using the PR itself as a hard mask till the depth of ~1 µm (Figure 40, *a*).
4) Room temperature AZ treatment was finally carried out to remove damage by dry etch material (this also removed residuals of LOR-3A and transformed circularly shaped cavities into hexagonal shaped ones as seen in Figure 40, *b*).

Iteration 2. – AlGaN Honeycomb template with 1+/3 µm (diameter/pitch)

In the second attempt, the initial AlN template was replaced by ~1.6 µm thick AlGaN on Kyma as the base material for µ-patterning. The following modifications of our approach were implemented here:

1) A blank bilayer of metal/silica was formed on the as-grown sample initially.
2) A single PR layer of S1813 was then spin-coated, prebaked, exposed (using the same optical mask as in the previous iteration-1) and developed (Figure 41 *a*, *e*).

3) Unprotected by S1813 silica was removed by Synapse dry etcher.
4) Exposed metal (Pd) was removed by *aqua regia* wet-etch where time was deliberately extended beyond the point of vertical etch (i.e. until the exposed metal was completely removed). This extra time metal underwent lateral etch allowing for larger openings compared to those defined by the optical mask (i.e. beyond 1 µm).
5) Short BOE was then used to remove residuals of the silica cap layer (Figure 41 *b, f*).
6) Upon this, the metal hard mask was translated into AlGaN using an ICP-RIE dry etch.
7) To remove the residual of the metal hard mask, a long enough aqua regia wet etch was implemented (Figure 41 *c, g*).
8) Finally, room temperature AZ400K treatment was carried out to remove damage by dry etch material and reshape in a crystallographic way, dry etched µ-holes (Figure 41 *d, h*).

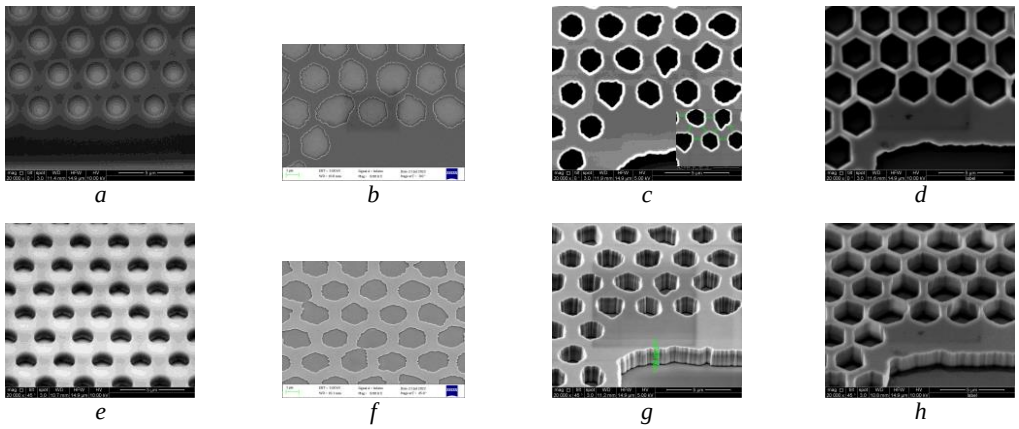

Figure 41: SEM images of AlGaN µHC (sample A (35s) with 1+ µm) obtained at different stages of fabrication process. The first row shows images (a-d) in Top view and second row shows images (e-h) in inclined view (45°). PR mask after lithography (a,e), Lateral etch of metal and cap removal (b,f), After dry etch with metal hard mask (c,g), After wet etch (d,h).

Generally, this approach did not work as expected: lateral wet etch of metal was found to be non-uniform resulting in strong deviations of openings from initially circular shape. This produced rather strong irregularities in the final µ-HC structures as can be seen from Figure 41 *c, d, g, h.*

In this iteration, two variations of samples were fabricated: in the first one (sample A), the lateral shrinkage of the metal hard mask was carried out for ~35 s (which corresponds to ~ 20 s of purely lateral etch) while dry etch was carried out

down to depth of ~1.7 µm (down to sapphire); in the second variation (sample B), the lateral shrinkage of the metal hard mask was carried out for 45 s (corresponding thus to a longer lateral etch of ~30 s) but a shallower dry etch was used (down to depth of ~1.5 µm). The main difference between these two variations therefore is in the aspect ratio of µ-holes.

AlGaN 2 µm µ-HC template

Since the expansion of the metal mask described above did not work well, a new specifically designed optical lithography mask with disks rather than openings and of larger diameter (2 µm disks vs previously used 1 µm openings) was designed, ordered and used to obtain AlGaN µ-HC structures. The exact fabrication workflow is described below:

1) Initially, a thin (~50 nm) silica layer was sputtered on the as-grown sample surface.
2) A bilayer of the same as before PRs was spin-coated on the base template followed by a standard optical lithography with the new mask.
3) Metal (Ni) evaporation was then carried out to form a ~80 nm layer.
4) Unwanted metal sitting on top of the resist disks (for this reason inverted optical lithography mask was used here) was removed by the standard resist lift-off process.
5) In this way formed metal hard mask (array of ~1.8 µm openings) was then translated into AlGaN using ICP-RIE dry etch down to sapphire (~2.2 µm deep, Figure 42, *a*, *e*).
6) To remove the residual of the metal hard mask, a long aqua regia wet etch was implemented while residuals of the silica cap yet remained.
7) An 80°C AZ400K wet etch of controlled duration (Figure 42, *b-d*, *f-h*) was carried out to achieve a crystallographic reshaping and expansion of the µ-holes while also destroying the cap layer in the process.

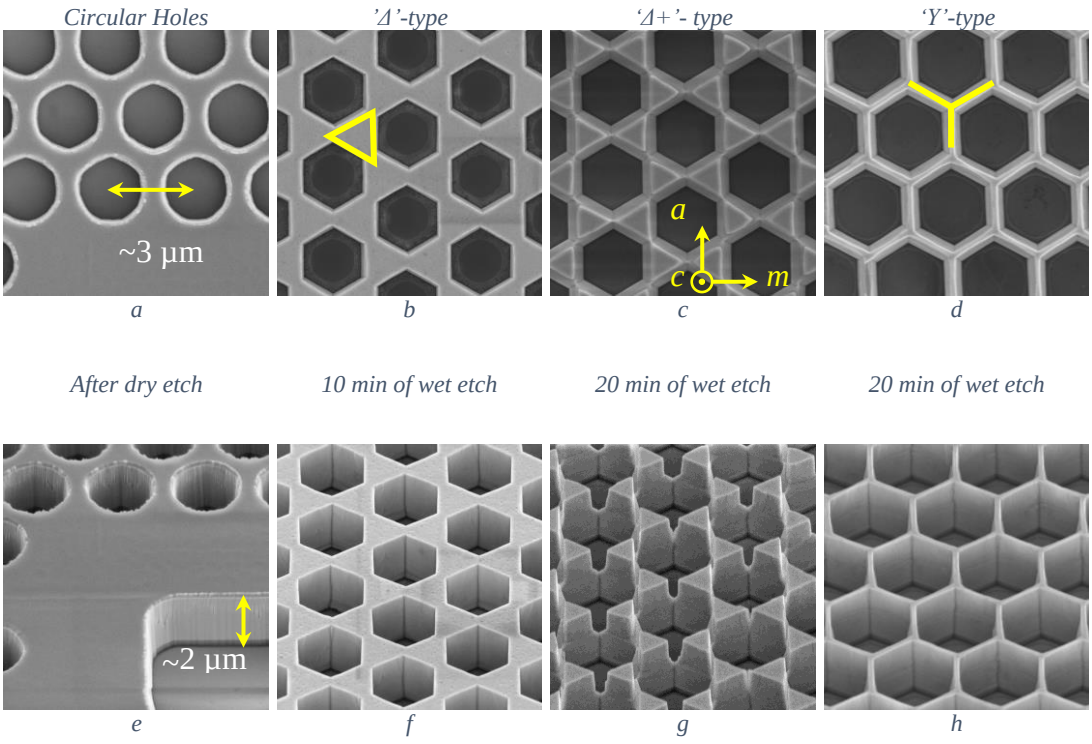

Figure 42. – Top view (a-d) and 45° tilted view (e-h) SEM images of AlGaN layers patterned into µ-HC: (a, e) - after dry etch; (b, f) - after 10 min wet etch in hot AZ (Δ-type); (c, g) - after 20 min wet etch in hot AZ ('Δ+'-type); and (d, h) - after 20 min wet etch in hot AZ (Y-type). The array pitch for all samples is fixed at 3 µm. ***Here and below: the width of the images is 9.2 µm unless specified otherwise; crystallographic orientation of AlGaN array as specified in image (d)*** *"Taken from reference [100]"*

As was mentioned above, a lateral expansion of holes using a wet etch of AlGaN using AZ 400K was implemented to reduce the amount of the initial material (together with dislocations in it) in our µ-HC templates. This approach was found to be significantly more homogeneous and crystallographic compared to the wet etch of metal in our previous experiment, which was significantly anisotropic and caused strong defects in the overall structure.

Due to the hexagonal transformation of initially circular µ-holes, two main configurations of µ-HC are possible and were fabricated: a configuration in which hexagons are adjacent to their neighbours corner-to-corner and a configuration in which they are adjacent side-by-side ("classic" honeycomb). Based on the shape of the residual material in these two configurations, they are referred to as Δ- and Y-type, respectively.

2.1.6 Fabrication of unipolar heterostructure devices

Unipolar heterostructure devices were fabricated using the process flow shown in Figure 43. In the first step i.e. just after wafer cleaning, photo-resist (PR) (S1813) was spin-coated (4000 rpm for 50 seconds), baked (at 115°C for 60 seconds) and exposed to UV radiation for ~7 seconds. This was followed by development (MF319 for 100 seconds) and later the photo-resist mask layer was used to etch ~500 nm into the sample. Leftover PR was removed from the surface of the sample. To define the top and bottom contacts of the device, a similar process of PR coating (but with lift-off PR), UV exposure and development was carried out, to open regions in PR where metal can be deposited. Ti/Al/Ti/Au as mentioned previously (P. 65 in section E-beam evaporator) was evaporated followed by lift-off to remove the leftover PR and metal from the surface.

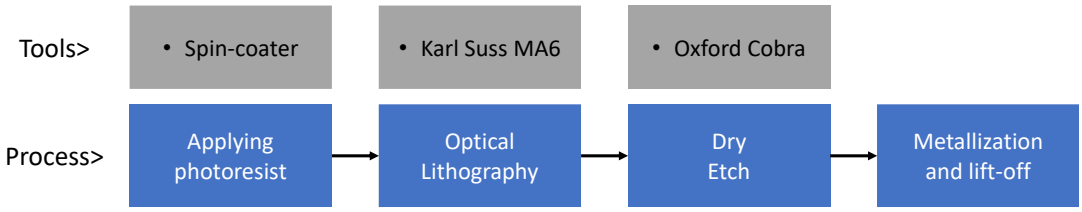

Figure 43: Schematic of the fabrication process of unipolar heterostructure device.

Samples discussed in this thesis were realized using the above techniques of epitaxial growth. Devices were fabricated on the epi-ready substrates and were later characterized. A set of fabricated unipolar devices with varying diameter is shown in Figure 44.

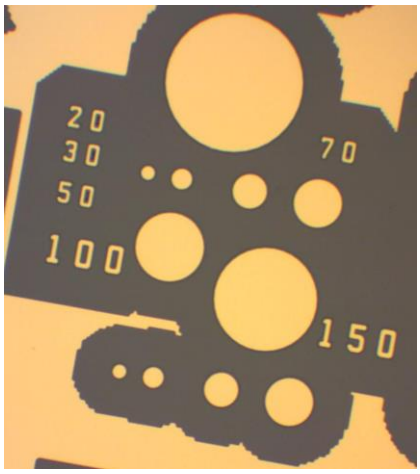

Figure 44:Fabricated unipolar devices.

2.1.7 Device Characterization Techniques

After fabrication, device parameters are assessed and their behaviour is studied by electrical characterisation. This provides insight assessment and helps in giving feedback on whether further optimization at the material level or fabrication process is required.

2.1.7.1 Current-Voltage Characteristics and Contact Resistance Measurement

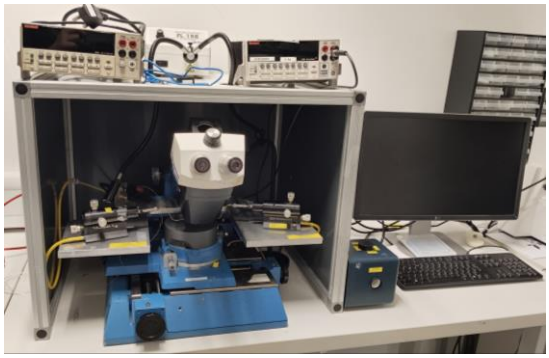

Figure 45: IV probe station

UPHS devices were characterized using an in-house probe station shown in Figure 45. Current-voltage measurement was accomplished using Keithley Source Meter 2400 and multimeter 2000. Probes of various diameters were available to measure the smallest dimension transmission line patterns. Top and bottom circular transmission line patterns available in the mask were used to measure the contact resistance and extract the resistivity of the bottom n-GaN layers.

Since there were device-to-device variations (mostly in terms of leakage current under the knee voltage range) least leaky devices were reported after comparing a good number of them.

2.2 Theoretical Methods

Apart from experimental techniques used in this study, some theoretical modelling was also required to develop a sound understanding of the device's physics. Particularly, one of my aims was to study the vertical transport of electrons through a unipolar heterostructure (UPHS), which can serve as a model structure analogous to EBL in an LED. This requires a sound understanding of the framework and the theoretical methods based on which transport equations are solved in simulation software. A detailed description of these procedures and approaches has been captured by Selberherr *et al.*[101] while I tried to discuss some of the important ones relevant to the used commercially available simulation package.

Semiconductor transport equations can be derived from Maxwell's, Poisson and continuity equations, the details of these derivations are largely available, so we do not discuss them here. However, only the important equations required for understanding of electron transport in UPHS will be discussed. The basic semiconductor transport equations were used to derive the most fundamental transport model i.e. drift-diffusion described below. As we know from Chapter 1 (subsection 1.1.2), III-nitride materials are polar in nature. Thus, it becomes important to incorporate polarization in the vertical direction (*c*-axis) while conducting the transport simulation and consider the contribution of electron terms in the carrier transport derivation. One of the tasks within this work was to check and validate the polarization charge generated at the GaN/AlGaN interface by Atlas (SILVACO) and compare these values against results obtained from an independently developed custom finite difference method (FDM) code. Overall, the development of these procedures was the foundational work which led to study carrier transport in polar semiconductors with compositional fluctuations which is discussed in the following chapter.

2.2.1 Transport Equation : Drift-Diffusion (DD) Model

2.2.1.1 Analytical considerations

In this section, a connection is established between the relevant basic semiconductor equations for electron transport in their respective reduced form, deemed important for the study of UPHS devices which is discussed in the following chapter.

Poisson's equation (2-4) associates the electrostatic potential (ψ) in a semiconductor device with the space charge density (ρ), where ϵ is the local permittivity of the material.

$$div\ (\epsilon \cdot \nabla\, \psi) = -\rho \tag{2-4}$$

The space charge density is the sum of all the contributions including mobile, fixed charges, ionized impurities and electrons, etc. present in a semiconductor material. In the context of our study n represents the ionized electron density and the term N_D^+ represents the ionized donor atoms.

$$\rho = e(N_D^+ - n) \tag{2-5}$$

Considering various sub-components of space charge density the new equation can be represented by equation (2-6).

$$div\ (\epsilon \cdot \nabla\, \psi) = -e(N_D^+ - n) \tag{2-6}$$

From the equation (2-6) electric field ($\vec{E}$) with the device can be determined by a simple integration.

$$\vec{E} = -\nabla\, \psi \tag{2-7}$$

Since the material is polar in the *c*-plane direction. So, considering the two components of polarization *i.e.* spontaneous (P_{SP}) and piezoelectric (P_{PE}) are considered then the modified third law of Maxwell's equation can be represented as:

$$\vec{D} = \overrightarrow{P_{SP}} + \overrightarrow{P_{PE}} + \varepsilon_0 \vec{E}\ , \tag{2-8}$$

where $\vec{D}$ is the electric displacement vector.

$$\vec{\nabla} \cdot (\overrightarrow{P_{SP}} + \overrightarrow{P_{PE}} + \varepsilon_0 \vec{E}\ ) = e(N_D^+ - n) \tag{2-9}$$

The evolution of electron density can be determined by continuity (2-10) and transport equations.

In case of the absence of any generation and recombination process, the electron transport continuity equations can be expressed as:

$$e\frac{\overrightarrow{\partial n}}{\partial t} = \frac{d(\overrightarrow{J_n})}{dz} \tag{2-10}$$

where $\overrightarrow{J_n}$ is the electron current density.

The motion of the carriers in the semiconductor device is determined by the electric field ($\vec{E}$) and by the gradient of carrier densities ($\vec{\nabla}n$) as in our case electrons. So, the semi-classical current expression comprising drift and diffusion terms is:

$$\overrightarrow{J_n} = -(en\mu_n\vec{E} + e\mathrm{D}_n\vec{\nabla}n) \tag{2-11}$$

where μ_n is the electron mobility, D_n diffusion coefficient of electron.

Many assumptions were applied to the Boltzmann equation to obtain the current relations (2-11) and are summarized* by Selberherr *et al.*[101]

In the presence of an external electric field, not all the electrons present in a semiconductor participate in carrier transport. For a one-dimensional simulation, the availability of carriers for transport is governed by Fermi-Dirac distributions:

$$n = n_{ie}\, exp\left[\frac{e\psi - E_{F,e}}{kT}\right] \tag{2-12}$$

where n_{ie} is the effective intrinsic carrier concentration, $E_{F,e}$ is the quasi-fermi level for electrons and T is the lattice temperature.

The semiconductor mathematical foundation developed till now, to understand the drift-diffusion transport calculations, requires further implementation of methods which can address the boundary physics, and generate a grid on which calculations can be carried out while finding a numerical solution.

2.2.1.2 Practical considerations for numerical solving

In this work drift-diffusion transport equations (2-11) for a UPHS device were solved in a computational tool (Atlas-SILVACO)[102]. The device geometry defines the boundary and the bounded domain in which the numerical solution to all the above semiconductor equations (2-6(2-11) is desired. The treatment of the semiconductor equations can vary depending on the input model in these two regions but it is important to have consistency in the numerical solution. The boundary can be

* In chapter 2 pages 22-23

again subdivided into two parts i.e. physical boundaries like contacts, interfaces, etc. or artificial boundaries which separate two devices. Having a priori information regarding the functioning of the device can ease the implementation of boundary conditions as this is associated with various factors such as materials and interfaces. The most commonly implemented types of boundary conditions are Ohmic, Dirichlet, Schotkky and Neumann boundary conditions. Selberherr *et al*. has discussed this in detail in Chapter 5[*] of his book[101]. In Silvaco, boundary conditions are implemented automatically by Atlas solver. In the simulation of the UPHS device model, homogenous Neuman boundary conditions[102†] were implemented in the lateral direction at the device boundaries. In this condition, current only flows out of the device through the contacts.

The analytical representation of the model is in the form of a system of partial differential equations which forms the basic semiconductor equations together with appropriate boundary conditions. In general, this system cannot be solved explicitly. So, numerical approaches were utilized to obtain a solution. A numerical approach for the solution of a system consists of three tasks. First, the domain i.e. the simulation geometry of the device, has to be partitioned into a finite number of subdomains, in which the solution can be approximated easily with a desired accuracy. Secondly, the differential equations are approximated by algebraic equations in each of the subdomains. This results in a large system of nonlinear algebraic equations with unknowns comprised of approximations of the continuous dependent variables at discrete points. Finally, the task is to determine the solution of this system of equations.

At this point, it is clear an exact solution cannot be obtained for the analytically formulated problem. The solution represents a good approximation to the solution of the analytically formulated problem depending upon the fineness of the partitions of the simulation subdomains and the suitability of the approximating functions for the dependent variables within the subdomains.

There exists more than one way of partitioning (discretization) these domains and choosing functions to approximate the dependent variables within the subdomains. The selection of a partitioning method is dependent on the complexity

[*] Page 149-158
[†] Page 168

level type of the problem. With this understanding, we would briefly discuss the finite difference method (FDM) and finite element method (FEM).

2.2.2 Finite difference method (FDM)

In FDM, a region (domain) of a particular material (preferably rectangular in shape) is further partitioned into small subregions by a rectangular mesh in such a manner that the external boundaries of edge subregions coincide with the domain boundaries. For each mesh point, the differential equations are replaced by the respective difference approximations, details of which are covered in Ref [101] (P. 182).

In the next chapter, a custom one-dimensional FDM code developed in MATLAB® is used to study the AlGaN barrier. In my code, Poisson's equation (2-9) is solved using the matrix inversion method. The values from Table 5 (mesh details) and Table 6 (material properties) were used in these FDM calculations, and the result was in the form of potential, electric field and polarization charge profile across the GaN/AlGaN/GaN interface.

Table 5: Mesh parameters used in FDM simulation of GaN and AlGaN

Parameter	Symbol	Units	Value	Ref.
Grid spacing	*gs*	Å	2.833	[103]
Epsilon of vacuum	ε_0	F/m	8.85418×10^{-12}	-

Table 6: Polarization Parameters for GaN and AlN
(All parameter values are from Ref.[104] unless otherwise mentioned.)

Parameter	Symbol	Atlas syntax	Units	GaN	AlN	Silvaco Table No. / Ref.
a-Lattice constant	a_0	ALATTICE	Å	3.189	3.112	B-21
Spontaneous polarization	P_{sp}	PSP	C/m^2	-0.034	-0.09	
Piezoelectric const.(z)	e_{33}	E33	C/m^2	0.67	1.5	
Piezoelectric const.(x,y)	e_{31}	E31	C/m^2	-0.34	-0.53	
Elastic const.	*C13*	C13	GPa	100	127	B-17
Elastic const.	*C33*	C33	GPa	392	382	
Permitivity	ε_r	-	-	8.9	8.8	B-24c
c-Lattice const.	c_0	-	Å	5.188	4.982	[24]

2.2.3 Finite Element Method (FEM)

A procedure similar to FDM is followed when partitioning a domain into a finite number of sub-regions in Atlas. However, in this case, each sub-region is referred to as a finite element (thus finite element method, FEM), and the shape of the partitioned subregions is, in contrast to FDM, triangular. All these elements (subregions) are approximated by a partial solution and the summation of all these partial solutions, results in a total approximate solution of the device. In general, a partial solution is a smooth polynomial function used to approximate the behaviour within an element and should be easily manipulatable while being computationally less expensive. Further details regarding the FEM mesh generation can be found in Ref [101] (P. 215).

A 2D FEM mesh is generated by Atlas for a device structure following the input design and the mesh control parameters. It should be mentioned that while the designers have control over some design aspects, complete control over the mesh generation process and optimization of the mesh is not available. Transport calculations are carried out on the obtained device mesh structure. The solution for the system of nonlinear algebraic equations is then obtained using Newton and/or Gummel methods.

In all simulations, the lateral dimension of the device structure shown in the Figure 46 was kept at 10 nm to maintain a reasonable simulation time of ~ 4 hr per random alloy map. Since it was found to scale with the lateral dimension of the UPHS device and due to limitations in computational resources. Further details regarding the actual implementation of these approaches are provided in the next chapter (subsection 3.1.1).

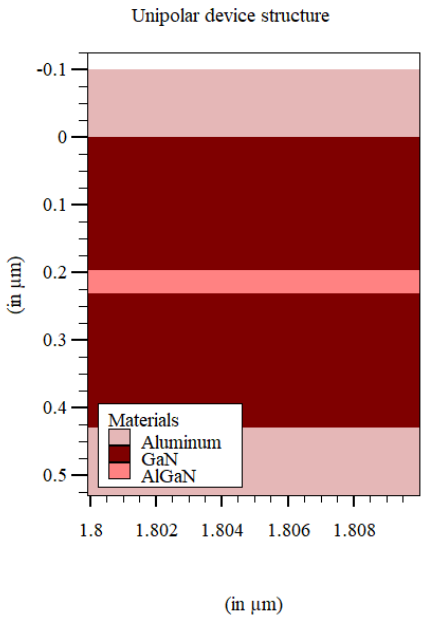

Figure 46: Simulation device structure

Chapter 3 Vertical electron blocking effect of *i*-AlGaN

In Chapter 1 (subsection 1.2.4.5), the design and importance of an AlGaN EBL in UVLED structure have been described in detail. However, previous studies using unipolar heterostructures (UPHS) have questioned its effectiveness as a barrier for vertical electron transport. To the best of my knowledge, this matter has been addressed both theoretically and experimentally at least twice[82,83]. Both works failed to demonstrate the rectifying properties of the AlGaN barrier in a UPHS. This seemingly contradicts the routine use of AlGaN as an EBL in UV and Visible III-nitride-based LEDs. This sets a scientific topic aiming to investigate this apparent discrepancy. So, efforts here were directed to understand the reason behind this alleged ineffectiveness of AlGaN as a barrier and whether it is possible to achieve an efficient barrier and if yes, then how.

In previous experimental works, it has been speculated that the ineffectiveness of the AlGaN as a barrier might be a consequence of its compositional inhomogeneity. So, in our research, we initially focused on studying carrier transport through the *i*-AlGaN layer described by various compositional descriptions using numerical simulations. In general, commercial technology computer-aided design (TCAD) solvers lack a built-in functionality describing inhomogeneous compositional variations. Therefore, a custom adaptation of standard TCAD functionality was required to describe alloy fluctuations in barrier material. Some time therefore was spent on the development and testing of a framework which can generate and transfer a compositional landscape into the TCAD solver. Transport calculations were then carried out on the transferred landscape.

In this study, simulation results build the initial theoretical foundation upon which our understanding relies and based upon these conclusions, a follow-up experimental study by the realization of UPHS samples has been conducted. The parameters which define the barrier effect of an AlGaN layer such as average aluminium content and thickness were studied and conclusive suggestions are presented.

3.1 Theoretical background and model description

As already mentioned in Chapter 1 (subsection 1.1.1), the hexagonal crystal structure of III-nitride materials imparts them with unique properties compared to conventional III-V materials. By virtue of crystallography, some crystal orientations have an intrinsic electric field which is absent in 001 oriented zinc blende III-V materials. Due to this, a standard theoretical homogenous description as used for III-V (e.g. $In_xGa_{1-x}As$) semiconductor materials cannot be directly applied to III-nitride materials[105].

The presence of disorder in III-nitride materials is well known and there exists significant evidence to support that compositional inhomogeneity is present[83,106–110]. The presence of these compositional fluctuations induces large polarization-related local electric fields, resulting in band offsets between group-III rich and poor regions[111,112]. This consequently, affects the conduction and valence band potential profile causing a reduction in knee voltage of an LED[108,113].

Nevertheless, it is important to study both (homogenous and inhomogeneous) descriptions and compare the results to have an in-depth understanding of the effect of compositional inhomogeneity and how it impacts the electrical characteristics of a unipolar heterostructure.

3.1.1 Representation of *i*-AlGaN in a unipolar structure by three different compositional models

In general, most device computational tools (Atlas Device Simulator from Silvaco Group, Inc. was used here) describe a ternary material like AlGaN as a homogenous material with uniform composition i.e. with fixed composition at all the grid points within a single block. This description of a material is referred to as virtual crystal approximation (VCA, Figure 47, *a*). It is extensively used because of its ease of

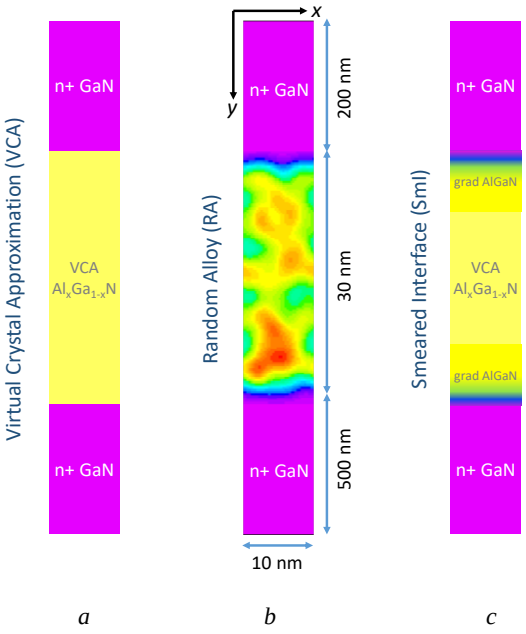

Figure 47: Model Description
a) Virtual crystal approximation (VCA)
b) Random Alloy (RA)
c) Smeared Interface (SMI)

implementation and is computationally less expensive. This approach to represent the composition of a material can be considered as a reference description but does not allow us to incorporate compositional inhomogeneity. So, a framework is required which can generate a compositional map and transfer it into the Atlas TCAD solver.

3.1.1.1 Framework Development

Compositional inhomogeneity in real devices based on ternary compounds sets the potential landscape in 3D, which can be any random shape. However, solving an inhomogeneity on just a 2D grid can still capture the effect in a lateral direction while minimizing computational complexity in calculation and still provide insightful results[108]. Here, this is implemented by dividing a larger map into smaller regions and declaring each region with specific declaration statements for its parameters e.g. mole fraction, size (dimension of the region), etc. All of this is incorporated within a framework (Figure 48) which can generate and transfer a two-dimensional compositional landscape (2D-CL) into the device editor (DevEdit) module of the SILVACO Atlas solver. DevEdit module generates a structure file containing the meshing information and other parametric definitions. The structure file is an input to SILVACO Atlas, which runs transport calculations on the transferred 2D-CL using the drift-diffusion (DD) method. Further details have been described in Chapter 2 (subsection 2.2.1).

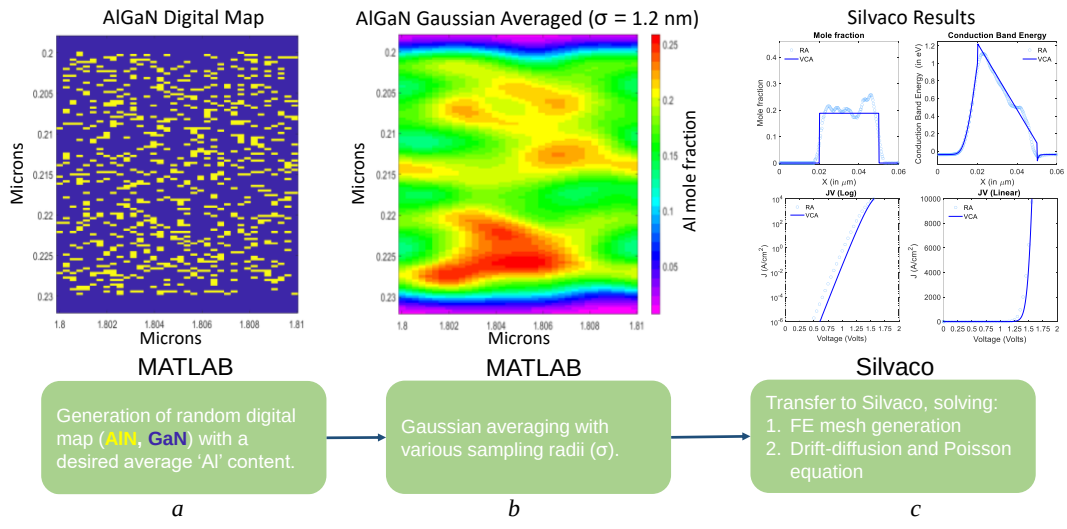

Figure 48: Framework for generation and transfer of alloy fluctuation landscape
a: Digital random map in matlab;
b: Gaussian averaging (same map as in 'a') in Matlab;
c: Results of transport calculation generated from Silvaco.

Initially, the framework was developed to generate and transfer a digital random alloy (RA) map (Figure 47, *b*) of a desired average composition consisting of GaN regions represented by 0's (blue colour in Figure 48, *a*) and AlN regions represented by 1's (yellow colour in Figure 48, *a*). The transport calculation on this type of digital landscape did not go through (i.e. met convergence issues) for aluminium composition ≥ 40%, this is due to the strong fluctuations in the conduction band energy profile. Besides such a representation is far from actual alloy fluctuations in real-world devices. Mainly this is because, firstly, our grid size in Atlas solver was still much larger than one crystal cell, and, secondly, carrier wavefunction size is also much larger to 'see' such abrupt compositional changes.

To address this problem Wu *et al.*[103] implemented Gaussian averaging which "smooths" the digital landscape making it computationally solvable. To implement a similar approach, the following formula was used for averaging:

$$x(i,j) = \frac{\sum_{n=j-3\sigma/gs}^{n=j+3\sigma/gs}\sum_{m=i-3\sigma/gs}^{m=i+3\sigma/gs} x(m,n)\times e^{-\frac{(m-i)^2+(n-j)^2}{2\sigma^2}}}{\sum_{n=j-3\sigma/gs}^{n=j+3\sigma/gs}\sum_{m=i-3\sigma/gs}^{m=i+3\sigma/gs} 1\times e^{-\frac{(m-i)^2+(n-j)^2}{2\sigma^2}}}, \quad (3\text{-}1)$$

where $x(i, j)$ is averaged composition at an arbitrary location (i, j); m, n are coordinates of cells among which a summation takes place; gs* is the grid spacing; σ is the effective radius of Gaussian averaging i.e. a half-width of the Gaussian smoothening parameter. The value of $3\sigma/gs$ therefore defines the number of cells before and after the cell in question that are taken into account during averaging. At this, it is considered that contributions from cells further away are negligible.

With this in mind, the workflow of the framework was amended and the Gaussian averaging step was implemented to achieve a softened landscape. On this note however, before implementing the averaging procedure, three questions need to be addressed: i) what value of the sigma should be used, ii) how to treat the interfaces in a vertical transport during softening, iii) which boundary conditions to implement in the horizontal direction.

Firstly, before defining the value of sigma (i.e. degree of softening), one has to define the maximum length scale over which averaging should be applied such that

* Grid spacing (*gs*) of 2.833Å is considered as it represent the average distance between cation atoms in GaN[103].

the effect of disorder can be preserved. Baranovskii *et al.*[114] estimated the spatial length scale for an electron by using the de Broglie wavelength $\lambda = \hbar/\sqrt{m^* E_0}$, where $m^*$is the electron effective mass[103] and E_0 the Urbach energy for AlGaN[115]. The estimated lower bound for the spatial size of the fluctuation for $Al_{0.2}Ga_{0.8}N$ is in the range of 1.38-3.08 nm*, which is of the order of exciton Bohr radius in this material system. We chose a value of sigma σ =1.2 nm which is low enough on the length scale of a disorder to incorporate the effects of compositional fluctuation on the carrier transport. This value was kept fixed for all of the simulations.

Regarding GaN/AlGaN or AlGaN/GaN interfaces†, there exists experimental evidence[106,116–121] that they are smeared rather than abrupt. There can be many reasons for this effect. However, as it will be shown later (sub-section 3.2.1) this smearing reduces the effective barrier height seen by an electron. So, to take this effect into account, the averaging procedure mentioned above was also implemented at these interfaces by expanding the AlGaN layer by 2 nm inside the GaN region on both sides of the *i*-AlGaN barrier. When averaging with pure GaN, graded composition AlGaN/GaN interfaces where the aluminium composition gradually reduces to zero are formed (Figure 47, *b*). While the physics of this interface smearing is different from the one defining the compositional landscape inside the AlGaN region, for simplicity, the same (isotropic) sigma was used.

Finally, in the horizontal direction, periodic boundary conditions were implemented on the left and right interface in the averaging code, to maintain distributional uniformity at the edges. It was later realized the effect of the left and right interface is fairly minimal on the calculation because Atlas solver defines these boundary/edges with Neumann boundary conditions avoiding current flowing outward.

At this point, simulation results from RA and VCA models suggested that the behaviour of carriers through a compositional inhomogeneous landscape is mainly affected by two regions i.e. at both the interface and in the central inhomogeneous region (between two interfaces). So, to understand the effect of a smeared interface on the carrier transport on its own (i.e. decoupled from the compositionally

* The band edge broadening of $Al_xGa_{1-x}N$[115] ($0.1 \leq x \leq 0.8$) varies E_0= 40-220 meV. Calculation of the lower bound of the spatial size of a disorder using m^*= 0.2[103] led to a range of 1.38-3.08 nm.

† In the UPHS model used in our simulation, the top (*n*-GaN/*i*-AlGaN) and bottom (*i*-AlGaN/*n*-GaN) interfaces are those through which current enters and leaves the *i*-AlGaN layer.

inhomogeneous landscape), a (just) smeared interface model (SMI) was also introduced with the inhomogeneous landscape replaced by a uniform composition (fixed aluminium content) in the central region but implementing the same averaging procedure spanning also by 2 nm outside of the barrier. This results in a UPHS with smeared interfaces but a flat potential profile inside the AlGaN barrier (Figure 47, *c*).

3.1.1.2 Comparison of integrated polarization charge in a UPHS at the interface using FDM and Atlas (Silvaco)

As was described in Chapter-1 (subsection 1.1.2), III-nitrides are polar crystals and so polarization charges generated at heterointerfaces define many properties of corresponding heterostructures. In particular, in UPHS, they will define the internal electric field which results in significantly increased barrier heights than what could be predicted from simple energy band offsets.

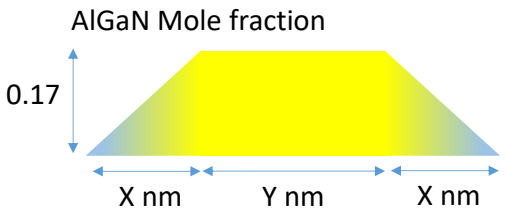

#	X (in nm)	Y (in nm)	Interface
a	0	30	Abrupt
b	3	27	Linear graded
c	5	25	
d	7	23	

Figure 49: Schematic of UPHS for total integrated polarization charge.

In the Atlas solver of the Silvaco package, the polar scale is set as a free-parameter. This typically is used to tune the polarization charges in modelling to match simulation results with experimental data. This can be justified in some cases, e.g. to describe partially relaxed quantum wells where the piezoelectric component of internal electric field might be only a fraction of what can be predicted from a direct comparison of corresponding lattice parameters.

Since the polar scale is a free parameter, varying it between simulations can change the outcome significantly. To decide which polar scale value is to be used in our simulations, a set of independent FDM calculations was carried out as described in chapter-2 (subsection 2.2.2). The FDM calculations produce charge densities based on theoretical values of polarization constants presented in Table 6. These values were compared to analogous figures from calculations using Atlas, and the polar scale was amended accordingly to match both results. Details of these preliminary calculations are presented below.

In a standard UPHS, the polarization charges are generated at the abrupt interface of the two materials; in our case GaN and AlGaN. To address this issue, a slightly modified standard UPHS (Figure 49) with linearly graded interfaces was simulated in Atlas and was compared with the results from the custom FDM code[122] mentioned above. The thickness at the interface varied from 3-7 nm as shown in Figure 49, while the uniform composition region in the structure was also amended to achieve consistency between the four structures. Since the calculations were conducted in two different computational environments, consistency in the material parameter value was achieved by using the same dataset (Table 5 and Table 6) from the Silvaco library for both FDM and Atlas calculations.

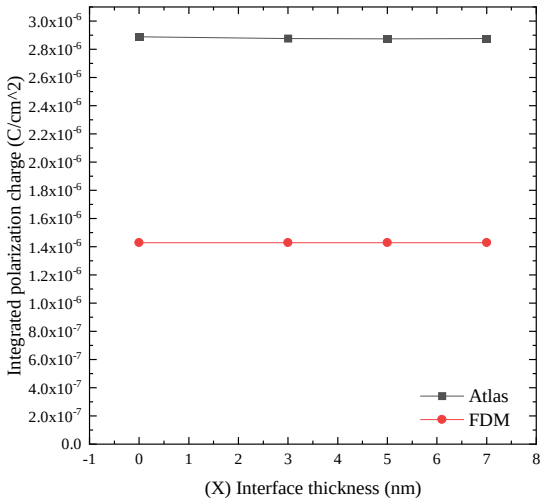

Figure 50: Effect of grading layer thickness on the integrated polarization charge in a modified UPHS with of a linear graded interface.

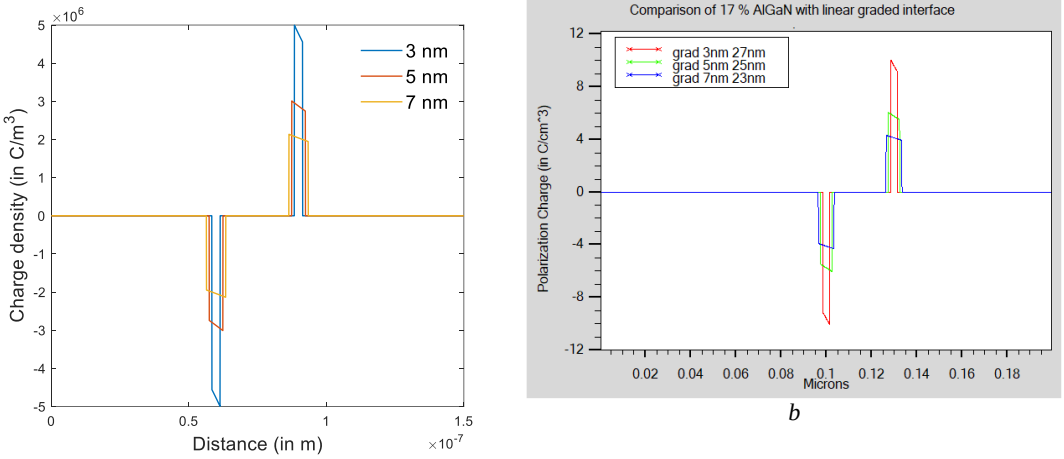

a *b*

Figure 51: Polarization charge (fixed) profile for AlGaN barrier with graded interface (3, 5, 7 nm) a: Finite difference method generated; b: Atlas-Silvaco

Thus, the integrated polarization charges shown in Figure 50 calculated using Atlas for the polar scale value of one (our default assumption) appeared to be higher by a factor of two compared to those obtained by FDM calculation. This is reflected

in the variation of interface polarization charge with thickness as shown in Figure 51*, effectively resulting in a higher conduction band energy profile (Figure 52) than reported in literature[82,83]. Simply, reducing the polar scale value to 0.5 is required to match the interface charges between the two solutions. This value was kept fixed for the rest of our simulation study.

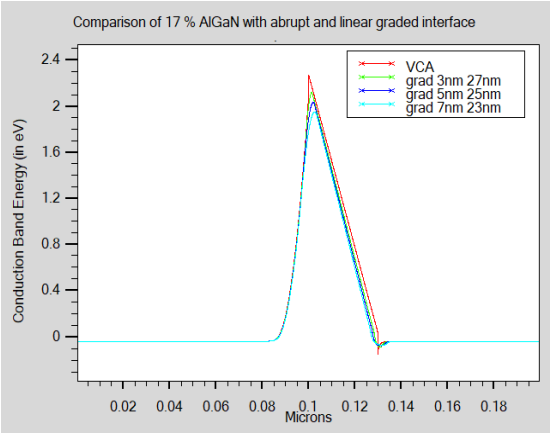

Figure 52: Effect of interface grading on the conduction band profile of a UPHS. (GaN/AlGaN/GaN interface shown)

3.1.1.3 Choice of transport method for simulation

Carrier transport calculation over a FEM grid is carried out using a method which solves the discretized transport differential equations. In Silvaco's Atlas, methods such as standard drift-diffusion (sDD) and self-consistent Schrodinger-Poisson drift-diffusion (SP-DD) are available for selection. Initially, an assessment of the optimum method between sDD and SP-DD was carried out. A simulation result by the sDD method was found to take significantly less time compared to SP-DD. Little to no difference in the thermal equilibrium band profile of a test structure (VCA-type) was found using sDD and SP-DD methods. Because of being computationally less expensive, sDD was preferred over SP-DD to study carrier transport in our *n*-GaN/*i*-AlGaN/*n*-GaN UPHS.

* The scale on the y-axis in FDM calculation is C/m^3 whereas in Atlas-Silvaco is C/cm^3.

3.2 Simulation results

In a standard transport simulation two types of results are generated i.e. a) thermal equilibrium and b) quasi-equilibrium. The thermal equilibrium characteristics of a structure show the behaviour without applied bias and can be used to study parameters related to the material and/or an interface e.g. conduction band energy profile, potential profile, maximum barrier height, etc. On the other hand, quasi-equilibrium characteristics display the behaviour of the structure which is subjected to applied bias between the contacts and is used to study device parameters e.g. JV characteristics, current density maps, etc.

In the next sections, simulations conducted to study the effect of material parameters such as 'Al' content and barrier thickness of *i*-AlGaN in a UPHS are presented.

3.2.1 Thermal equilibrium conditions

In general, the barrier height of an AlGaN layer is associated with the composition as can be seen from the interface of *n*-GaN/*i*-AlGaN/*n*-GaN shown in Figure 53. The increase in barrier height is attributed to an increase in the total polarization of the AlGaN layer which is directly proportional to the Al content in the layer.

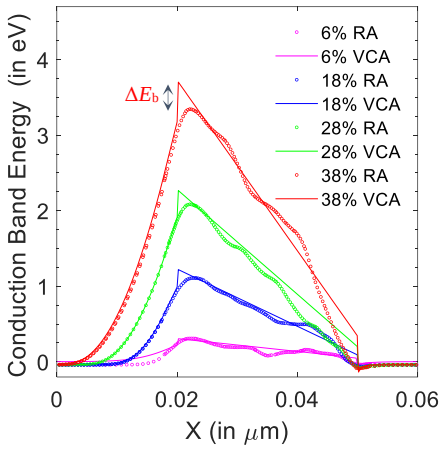

Figure 53: Effect of 'Al' content on the conduction band energy profile at n-GaN/i-AlGaN/n-GaN interface with barrier thickness of 30 nm.
(Linescan was taken at the center of the simulation cell)

It was observed that the difference (ΔE_b) between the estimated barrier height from RA and VCA models increases with aluminium content. While in RA models there is a certain degree of randomness as will be shown later, this effect can be understood in terms of a proportional decrease of barrier height in the RA model compared to the VCA one. In other words, on average RA model gives only a fraction of VCA barrier height; as a result, as barrier height increases the difference also increases.

On the other hand, an increase in AlGaN barrier thickness (Figure 54) is also associated with an increase in barrier height. This behaviour is due to the fact that the field is applied over a longer distance in the AlGaN layer resulting in a larger potential drop. Comparing the estimated barrier height from the SMI and VCA model, it is clear that the smearing of the interface on itself is the reason behind the lowering of the barrier height at the *n*-GaN/*i*-AlGaN interface in Figure 54. This is caused by the spreading of the polarization charges over a thickness at the respective interfaces in an SMI model compared to the delta profile of these polarization charges generated at the abrupt interfaces implemented in the VCA model.

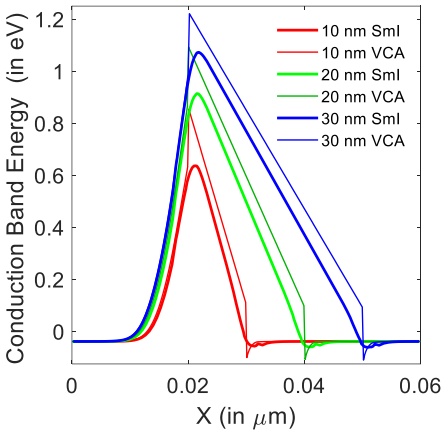

Figure 54: Effect of barrier thickness on $Al_{0.18}Ga_{0.82}N$ conduction band energy profile at n-GaN/i-AlGaN/n-GaN interface.
(Linescan was taken at the center of the simulation cell)

Another important observation in Figure 54, is the reducing difference between the estimated barrier heights (peak of conduction band energy profile) of the two models with an the increase in barrier width. This suggests that the reduction in barrier height due to smearing gets weaker as the barrier thickness increases (i.e. the effect of the interfaces reduces) and vice-versa. This can be understood from a stronger relative distortion of thinner barriers by the same smearing procedure implemented (fixed sigma value).

3.2.2 Quasi-equlibrium conditions

In general (purely geometrically), a UPHS appears to be symmetric. Nevertheless, the presence of a polarization field in III-nitride materials along the *c*-direction introduces an asymmetry in the energy profile (only conduction band energy is considered here) at thermal equilibrium as can be seen in Figure 55. Because of this asymmetricity, when an external field (bias) is applied across a UPHS, the JV characteristics should have different knee voltages in the forward and reverse bias conditions.

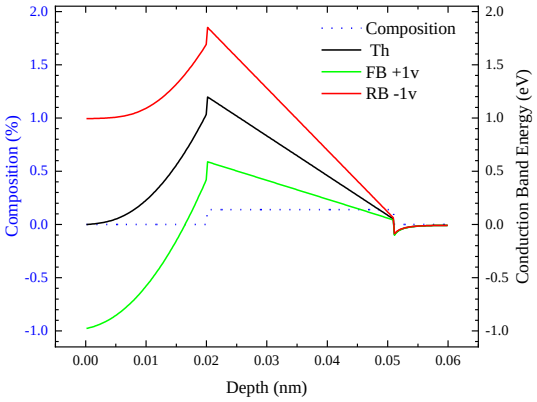

Figure 55: Effect of applied bias on the conduction band energy profile at n-GaN/i-AlGaN/n-GaN interface. (Linescan was taken at the center of the simulation cell)

Besides that, as was shown previously (sub-section 3.2.1), the effective barrier height seen by a carrier during transport is dependent on the composition of the AlGaN barrier and its thickness. Below, these effects are being considered theoretically and experimentally.

3.2.2.1 Effect of alloy fluctuation

Previously, Nath *et al.*[82] had conducted simulations using virtual crystal approximation and random alloy models in which the authors observed rectifying behaviour. So, consistently with the above study, our VCA model also shows rectifying behaviour (Figure 56, thin solid curve). When the JV characteristics were generated from the multiple landscapes of our RA model (symbols in Figure 56), they showed also rectifying behaviour. The calculated JV characteristics are characterized by

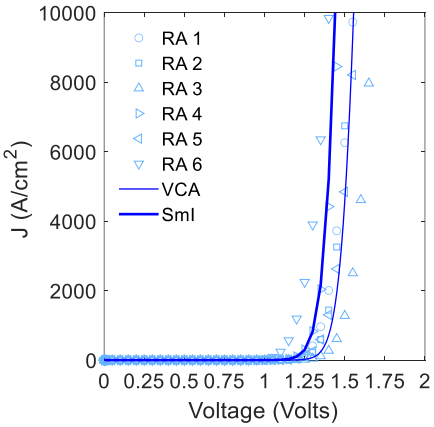

Figure 56: Effect of various compositional model on JV-charactertsics of a UPHS. (RA) Random alloy model landscape 1-6, (VCA) Virtual crystal approximation, (SmI) Smeared Interface model

slightly different knee voltages tending to be smaller than that for the VCA model. The varying knee voltages for six different RA landscapes show a spread which indicates an underlying statistical nature.

To compare a true RA model to a simplified SMI approach, the corresponding JV characteristics were also plotted in the same figure. While in the ohmic region, it tends to be more conductive compared to most of the RA maps, it is able to capture the general trend for the previously observed statistical nature in various RA landscapes in the knee region which is best visible data presented in the log scale (Figure 57). A significant lowering in knee voltage for the SMI compared to the VCA model was observed. This is due to the fact that smearing is attributed to a reduction in the barrier height as was shown above. Even this reduction in knee voltage is not enough to explain non-rectifying behaviour (observed experimentally in the previous studies[82,83]) i.e. SMI model also shows rectifying behaviour as was previously observed in the above models.

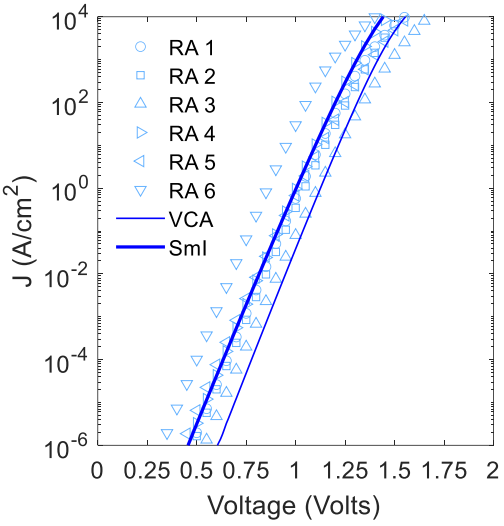

Figure 57: Effect of various compositional model on log JV-charactertsics of a UPHS. (RA) Random alloy model landscape 1-6, (VCA) Virtual crystal approximation, (SmI) Smeared Interface model

Overall it can be concluded that even the incorporation of compositional inhomogeneity (RA model) in *i*-AlGaN layers leads to rectifying behvaiour and not ohmic. A simpler model using just the smearing of the interfaces can capture a general trend of plurality of more complex RA models of UPHSes.

3.2.2.2 *Effect of 'Al' content in the AlGaN layer*

In section 3.2.1 (Figure 53), the influence of Al content in the AlGaN layer on the barrier height has been highlighted. From this, congruence can be drawn that VCA and RA models will show similar behaviour as the aluminium content in the barrier increases. Exactly this is demonstrated in Figure 58 although one needs to keep in mind the statistical nature of the RA model.

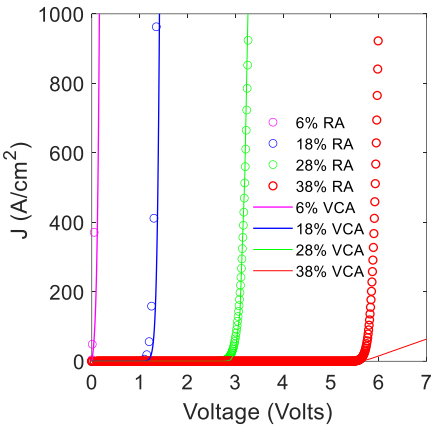

Figure 58: Effect of aluminum content in AlGaN barrier on JV-charactertsics of a UPHS. AlGaN layer thickness was 30 nm. (RA) Random alloy model, (VCA) Virtual crystal approximation

It is interesting to note that on one hand the knee voltage superlinearly increases with barrier height and on the other hand, has a certain threshold so that almost non-rectifying behaviour is observed for UPHS with no 0% barrier (which would be intuitive) but up to 6% Al content in UPHS barrier, which corresponds to potential barrier height of ~0.3 eV. The exact reason for such behaviour is not known, so I can only state that, according to my simulations, there exists a minimal barrier height leading to no essential obstacle for vertical carrier transport in UPHS.

The super-linear increase in rectifying nature with the increase in aluminium content (Figure 58) once the rectifying is established can be at least partly explained by the increase in barrier height with aluminium content, which is also super-linear (Figure 53).

It is worth noting that while the differences between the JV characteristics of low aluminium content UPHSes ($\leq 28\%$) obtained by RA and VCA models have mostly statistical nature and the overall deviations between these models are rather small, for the 38% case, it is relatively high, particularly in the series resistance region. This behaviour is only apparent though. Deviation of models, including the averaging procedure from the "pure VCA" one, occurs eventually at any composition of barriers (not shown). For lower compositions, this deviation happens later i.e. at higher biases above knee voltages corresponding to current density levels that are not even realistic and thus are not visible in Figure 58 which is limited to 1 kA/cm^2. At this stage, the nature of this deviation is unknown.

3.2.2.3 *Effect of Barrier Thickness*

In section 3.2.1 (Figure 54), it was shown that AlGaN barrier thickness directly influences the barrier height and is attributed to the observed rectifying behaviour shown under bias conditions by SMI and VCA models in Figure 59. The reducing difference between the JV characteristics of the two models suggests that interface smearing can be neglected for thicker barriers. Similarly to the decreasing difference in barrier height between VCA and SMI models for thicker barriers, this can be understood from a stronger relative distortion of thinner barriers by the same smearing procedure implemented (fixed sigma value).

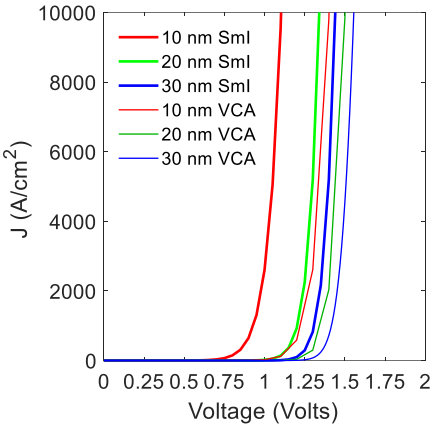

Figure 59: Effect of $Al_{0.18}Ga_{0.82}N$ barrier thickness on JV-charactertsics of a UPHS. (SmI) Smeared Interface model, (VCA) Virtual crystal approximation

3.2.3 Conclusion of simulation

In our 2D-transport simulation, irrespective of the compositional description of *i*-AlGaN (VCA, SMI or RA), a rectifying behaviour of UPHS were observed routinely except for UPHS with low aluminium content (less than ~8%) in their barriers. This observation is similar to the previously reported simulation results but deviates from previously reported experimental data, which shows a non-ohmic but not particularly rectifying behaviour.

It was found that aluminium content in the barrier of a UPHS is a more critical parameter defining the rectifying behaviour as knee voltage increases superlinearly with aluminium content but sublinearly with thickness. Real UPHSes need to be modelled with the RA approach whereas the inhomogeneity in the particular landscape sets its statistical deviation. As a result, multiple landscapes must be modelled to understand the general trend of a particular design (composition and thickness). In this regard, the SMI model was found useful to capture exactly these general trends.

While RA/SMI models give routinely lower knee voltages compared to VCA, the exact value by how much lower is expected to depend on the sigma value used in our smoothening procedure. This matter was left out of the scope of my study but the

effect of sigma used here (1.2 nm) was found to diminish for thicker barriers which leads to a conclusion that for thick enough barriers smearing of interfaces can be ignored and vice-versa is crucial for thinner barriers.

Since there is a discrepancy between our simulation results with previously reported data, further experimental verification of these results needs to be carried out.

3.3 Unipolar transport: Experimental results

Simulation results reported in the previous section indicate that the applied averaging procedure leading to UPHS with smeared interfaces reduces knee voltage but preserves the rectifying behaviour of *i*-AlGaN barrier disregarding both the presence of alloy fluctuations in it and their absence. As was mentioned above, this seems to contradict the published experimental results[82,83] and therefore requires independent experimental assessment. Here, I investigated this subject by MOCVD growth of UPHS samples on *c*-plane GaN templates (Figure 60), fabricated and characterized devices from the grown epi structures to either validate my simulation results or confirm previously published findings.

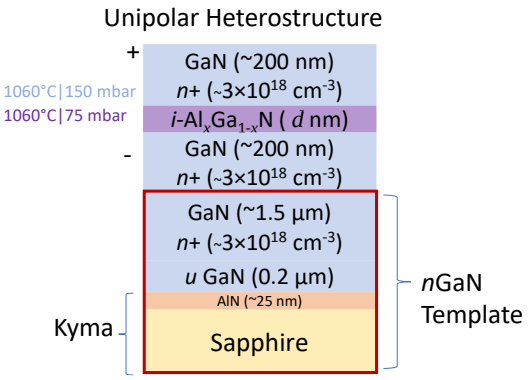

Figure 60: Schematic of UPHSs grown.

3.3.1 Initial assessment

To assess the effectiveness of the AlGaN barrier in UPHS, a test structure was grown according to the schematic in Figure 60. To deposit it, an *n*-type GaN template was initially grown on a Kyma substrate (25 nm of PVDNC™ AlN on sapphire). In a separate run, the template was heated up to a target temperature of 1060°C and a ~200 nm *n*-GaN connecting layer was grown. The growth was then stopped, and reactor conditions were ramped to AlGaN conditions. After AlGaN barrier growth, reactor conditions were ramped back to *n*-GaN conditions, and the growth was reinitiated to deposit the top *n*-type layer.

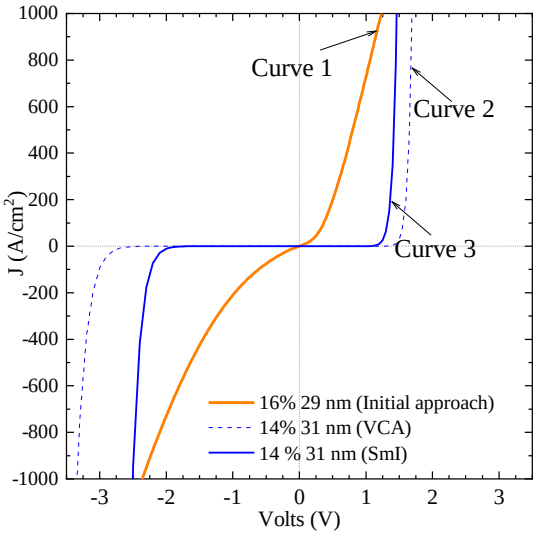

Figure 61 Experimental JV-characteristics of UPHS sample grown using the initial (straightforward) approach.

Upon device fabrication as described in Chapter 2 (subsection 2.1.6), the UPHS sample was characterized electrically, and its JV-characteristics are shown in Figure 61 (Curve *1*, x_{Al} ~16 % and d_{AlGaN} ~29 nm). As can be seen, the UPHS exhibits a non-ohmic but also not particularly rectifying behaviour, which is in agreement with the previously published results[82,83]. At the same time, it is in striking contradiction with our simulation results based on VCA (ibid., Curve *2*, x_{Al} ~14 % and d_{AlGaN} ~31 nm) which shows clear rectifying behaviour. Although the model involving the smearing of interfaces (which as shown above, is a good estimation of the alloy fluctuation effect) has somewhat lower knee voltage (ibid., Curve *3*, x_{Al} ~14 % and d_{AlGaN} ~31 nm), still the difference with experimental results is significant. At this stage, we are in the position of authors who addressed this topic previously[82,83]. To advance beyond it, further investigation is required to understand the mechanism behind this disagreement.

One possibility is that rectifying property suffers from growth interruptions implemented when grown UPHS is in question. At this point, there can be more than one possible reason for this non-rectifying behaviour, for example, incorporation of contaminants atoms or point defects at the interface and/or accumulation of silicon on the *n*-GaN layer during desorption before the growth of the AlGaN layer. Some damage to AlGaN during the transition from AlGaN to *n*-GaN conditions seems to be less likely due to its higher thermal stability. Nevertheless, the formation of fissures in the low aluminium content AlGaN layer during growth interruption was previously observed in our group by Smith *et al.*[123] and recently reported by Hinz *et al.*[124].

Detection of native point defects or accumulation of silicon atoms at the *n*-GaN/*i*-AlGaN interface is problematic, particularly requiring SIMS analysis in the latter case, which is not available internally. On the other hand, it was possible to check the effect of growth pause on the AlGaN surface. For this, two test structures were grown with no top *n*-GaN layer. The first test structure was grown using the same growth approach as the full UPHS sample i.e. with a 60 s-long annealing step before cooling down (simulating growth pause after AlGaN barrier in the UPHS sample). The second test structure did not have such an annealing step; moreover, the carrier gas was switched to nitrogen to avoid any possible damage to AlGaN [123].

After growth, both samples were analysed by SEM, and the corresponding SEM micrographs are presented in Figure 62.

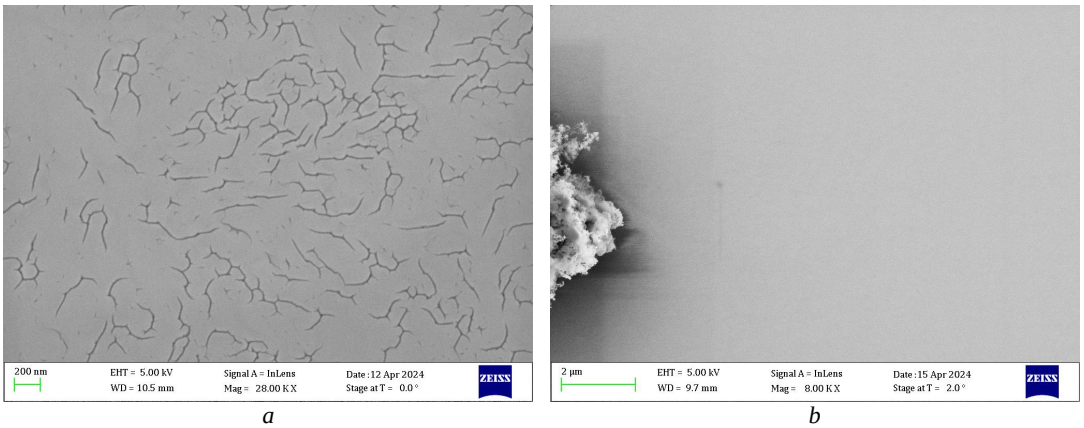

a *b*

Figure 62: SEM (secondary electron) images of AlGaN surface of test structures grown with (a) and without (b) 60 seconds of post-growth annealing. Note that the image (b) was intentionally taken with a particle at the edge to show focus.

As can be seen from Figure 62, *a*, nanoscale fissure gets formed on the AlGaN surface after exposure to an H_2/NH_3 environment (60 s at 1060°C followed by cooling in the same environment). According to literature [123, 124], this occurs due to the desorption of gallium from the top surface leaving behind an Al-rich crust. The reason for the desorption of gallium adatoms from the surface is due to the low binding energy of gallium with nitrogen compared to aluminium.

On the other hand, the second test sample had very smooth surface morphology (Figure 62, *b*) so to measure it by SEM, we had to include a particle within the micrograph frame to show that the image is in focus.

The growth of *n*-GaN on an AlGaN layer with a fissured surface might result in the diffusion of silicon atoms into fissures, creating regions with conductive paths that have lower or higher bandgap/conductivity which might effectively compromise the effectiveness of AlGaN as a barrier. To check if this is the case, our initial approach to growing UPHS was modified in such a way that growth pauses are avoided. This results in continuous growth (during the AlGaN layer) which prevents the formation of fissures in the AlGaN surface while simultaneously minimising the impurities and native defects incorporated into the material. As growth conditions for *n*-GaN and AlGaN are different and cannot be changed instantaneously, one of the layers has to be grown in sub-optimal conditions.

Since the AlGaN layer is the crucial one in this structure, *n*-GaN kept growing during the transition of growth parameters. This 60-second transition time (which now is filled with *n*-GaN growth) was the only difference between this modified approach

compared to the original one (Figure 63). This resulted in a UPHS with slightly thicker *n*-GaN layers but theoretically, it should have no impact on the JV characteristics.

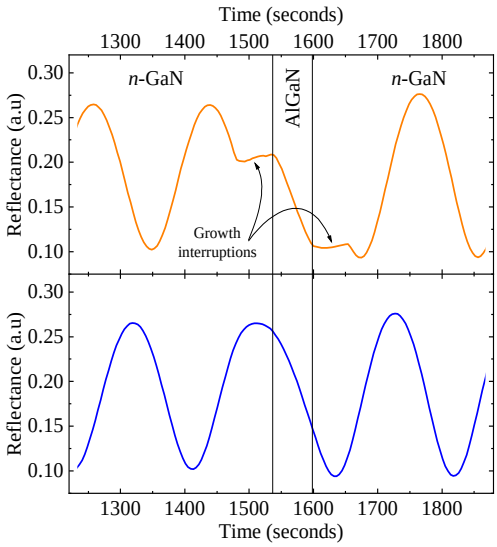

Figure 63: In-situ reflectance of UPHSes grown with and without interruptions.

The UPHS sample grown using the modified approach was fabricated and characterized in the same way as the previous one. Despite nominally identical AlGaN barriers implemented in these two samples, XRD analysis shows that their estimated Al contents and thicknesses non-insignificantly deviate from each other (x_{Al} ~16.3 % and d_{AlGaN} ~29.3 nm vs x_{Al} ~13.5 % and d_{AlGaN} ~36 nm). Based on simulation results, these two barriers should result in roughly equivalent rectifying properties as higher aluminium content is compensated by a thinner barrier and vice-versa. However, from the resulting JV-characteristics of both structures presented in Figure 64, a striking difference is evident. As can be seen from the figure, prevention of AlGaN barrier nano-fissuring resulted in quite obvious rectifying behaviour of UPHS (compare curves *1* and *2*[*]).

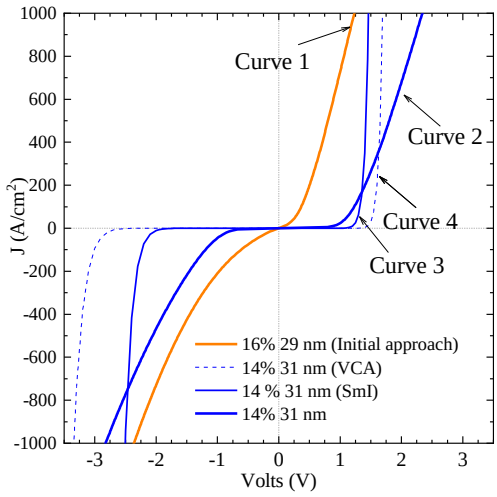

Figure 64 Comparison between simulation and experimental JV-characteristics of sample with and without growth pause
Experiment: thick continuous line;
Smeared interface (SmI) simulation: continuous line;
VCA simulation: dashed.

With now "normal" behavior of the UPHS with undamaged AlGaN barrier, it is possible to test our simulation results against experimental data. For this, curves *3* and *4* are added to the figure ('VCA' and 'smeared interface' models, respectively) Although the VCA estimation of barrier knee voltage gives a much higher value, the agreement is fairly good for the model

[*] Sample aluminium content and thickness is x_{Al} ~14 % and d_{AlGaN} ~31 nm.

taken into account smeared interfaces of AlGaN barrier. It is worth noting that a standard sigma value of 1.2 nm was used in this simulation i.e. it was not used as a free parameter to achieve the best fitting with experimental data. Further study would be required to understand whether just a larger sigma value is required or if there are some other effects in play which are not captured by our models.

Besides the knee voltage difference, there are other discrepancies between the experimental data and our simulation. The first one is the ohmic region of JV characteristics (above the knee voltage): observed in the experiment series resistance is larger compared to the simulation results. This can be easily explained: experimental series resistance is determined by lateral conduction (tens of micrometres) between UPHS contacts which is not taken into account in simulation.

Another discrepancy lies in the symmetricity of experimental JV-characteristics (curve *1*) while as discussed earlier, the presence of polarization field in III-Nitride material along the *c*-plane direction introduces an asymmetry in the conduction band profile (section 3.2.2, Figure 55), which translates also into asymmetric JV-characteristics in simulation. Unfortunately, there is no satisfying explanation for this observation presently. It can only be speculated that it is due to the smearing of GaN/AlGaN or AlGaN/GaN or both the interfaces [106,116–121]. As can be seen from comparing the JV characteristics of Curve *1* and Curve *4* in Figure 64, which was obtained from a smeared interface model with similar aluminium content to the experimental sample shows better agreement in both forward and reverse bias conditions. As was mentioned above, it predicts forward bias knee closer to experimentally observed value as well as somewhat decreased asymmetricity compared to VCA simulation although still by far not as symmetric as in the experiment.

Observation of fissures at the top *n*-GaN/*i*-AlGaN interface does not rule out other effects occurring in the AlGaN layer or at the bottom *i*-AlGaN/*n*-GaN interface which might affect the effectiveness of AlGaN too.

One such effect can be the natural chemical ordering of group-III atoms in AlGaN[126–128] and is attributed to the formation of so-called "*superstructures*"[127]. This effect goes against our conventional understanding of $Al_xGa_{1-x}N$ which is usually considered as a purely disordered alloy. These superstructures are not formed homogeneously throughout the entire material[127]. Formation of these structures is

associated with a) reduction of lattice symmetry, b) localization of the wavefunction (carrier localization) in the GaN layers and c) bandgap reduction[128]. Overall literature[126–129] suggests that the formation of these ordered regions impacts the electronic and optical properties of $Al_xGa_{1-x}N$ alloy. Since, formation of these superstructures breaks crystal symmetry, the observation of otherwise forbidden reflections (000*l*, where *l* is an odd number) in diffraction measurements may result.

I have also observed the forbidden (0001) reflection in the UPHS (Figure 65, *b*) studied here, where such a forbidden peak is present for the AlGaN layer but not for *n*-GaN (Figure 65, *d*). This observation supports the presence of ordered regions within the barrier layer of our UPHSes which have effectively narrower bandgaps compared to the purely disordered regions of similar average compositions that can act as percolation paths which are not captured by my theoretical models (all three: VCA, SMI and RA).

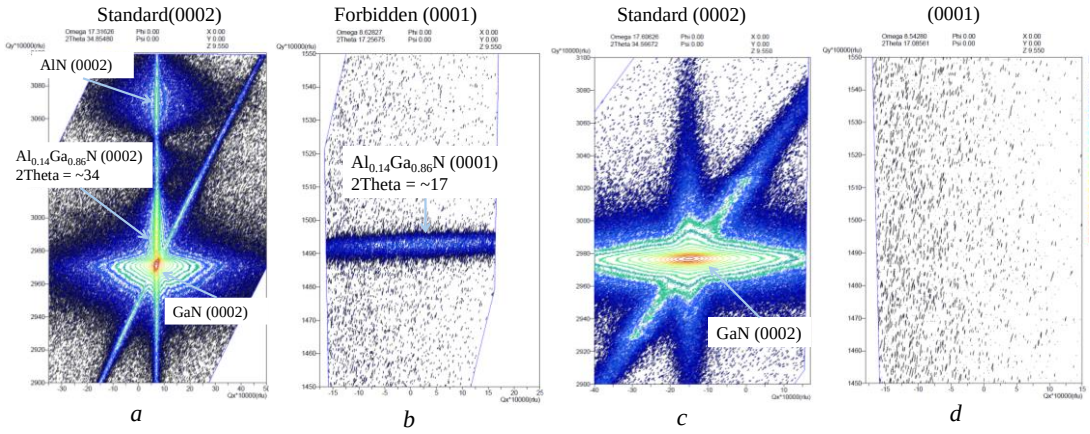

Figure 65 Comparison of reciprocal space map of $Al_{0.14}Ga_{0.86}N$ layer in a UPHS with a typical thick n-GaN layer.
a) Standard (0002) reflection of UPHS, b) Forbidden (0001) reflection of UPHS,
c) Standard (0002) reflection of a n-GaN, and d) Forbidden (0001) reflection of a n-GaN.

Further investigation is required to find out: a) the exact reason for the non-rectifying behaviour; b) why the JV-characteristics are symmetric; c) what is the impact of natural ordering in AlGaN; and d) how the growth pause at the bottom interface impacts the barrier effect of AlGaN. Nevertheless, to the best of our knowledge, this is the first experimental observation of AlGaN behaving as an effective barrier for vertical electron transport. Hence, its effectiveness as a function of Al content and barrier thickness can be studied and our simulation models can be tested accordingly.

3.3.2 Sample description

Since the barrier effect by the AlGaN layer has been observed, it makes it possible to further study this as a function of aluminium content and barrier thickness to correlate with the trends observed in our simulations. To investigate this, besides the already mentioned early samples (UPHS sample grown with growth interruption and two test samples), two additional series of samples were prepared (Table 7): In the first series (samples 1-3), aluminium content was varied; in the second series (samples 1, 4, 5), barrier thickness was varied. To grow these samples, the optimised approach was used involving no growth interruptions: the reactor pressure was changed from 150 to 75 mbar and back for AlGaN growth while GaN kept growing during these pressure ramps.

Table 7: UPHS sample details

Sample #	x_{Al}, % (Target)	d_{AlGaN}, nm (Target)	x_{Al}, % (XRD)	d_{AlGaN}, nm (XRD)
I*	20	25	16.3	29.2
II†	20	25	-	-
III‡	20	25	-	-
1	20	25	13.5	36
2	10	25	~8	~23
3	30	25	~33.5	~31
4	20	15	~14	~18
5	20	35	~17	~42

Notably high discrepancies between the target and actual values of aluminium contents and thickness in these samples are caused by the fact that no calibration layers were grown before the sample series.

* Sample was grown with 1 min growth pause at both sides of its AlGaN barrier.
† Test structure (without top *n*-GaN) grown using the same approach as sample I.
‡ Test structure prepared without growth interruptions and cooled down in N_2 ambient.

The total dislocation densities in the material samples estimated from X-ray diffraction was found to be ~10^9cm^{-2}. This values suggests that ~19,625 dislocations is present in each fabricated UPHS device with a circular diameter of 50 µm. The estimation of Al content was carried out by fitting the experimental 0002 ω-2θ scans in Xpert Epitaxy software assuming fully strained AlGaN. This was confirmed by measuring 105 reciprocal space map (Figure 66) for the sample with the highest Al content (≈33%): the AlGaN-related peak is perfectly vertically aligned relative to the GaN peak.

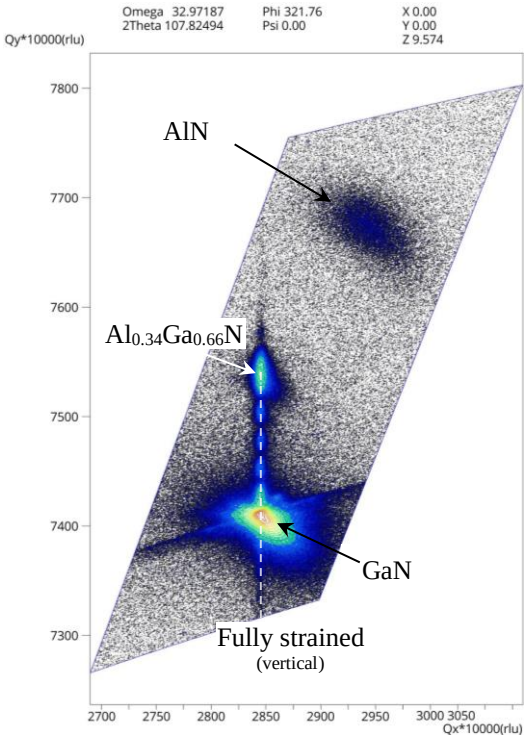

Figure 66 Reciprocal space map (105) of UPHS with the highest content of Aluminium ($Al_{0.33}Ga_{0.63}N$ strained to GaN)

3.3.3 Effect of Al content in AlGaN barrier

The sample series in which Al content was varied shows as expected rectifying behaviour for two higher aluminium contents as can be seen in Figure 67. This trend is similar to what we observed in our simulated results (Figure 58, sub-section 3.2.2.2), i.e. the rectifying nature increases with Al content in the barrier. A knee voltage of ~4.9 V was observed in the sample with Al content of ~34 % and 31 nm shown with a red continuous line, which matches fairly well with ~3.5 V for 28% AlGaN and 5.9 V 38% AlGaN UPHSes modelled in 3.2.2.2.

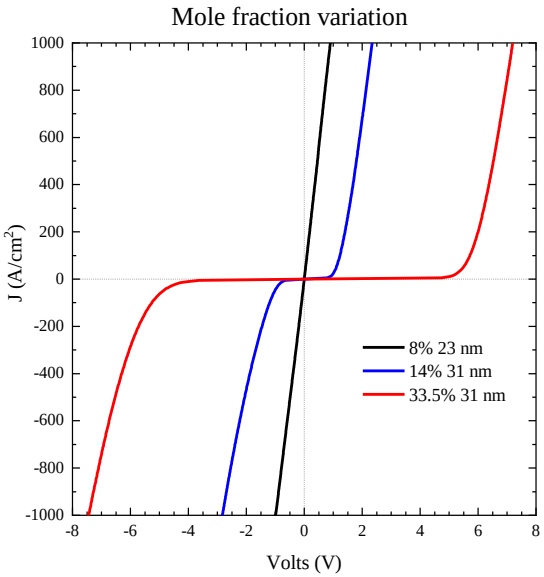

Figure 67: Experimental JV-characteristics of sample with varying 'Al' content.

The sample with only 8% aluminium content, however, shows no rectifying behaviour, which cannot be predicted by our simulation. There is obviously another mechanism not covered by our theoretical description allowing carriers to pass through low aluminium content AlGaN layers of UPHSes without feeling a barrier. The exact mechanism for that is not known at this time, but already from this observation, one can conclude that for a reliable barrier effect in an LED EBL, its compositional contrast with the adjacent layer (typically the last quantum barrier) should be enough large (at least 12-15%[*]).

[*] The exact value might also depend on EBL thickness.

3.3.4 Effect of AlGaN barrier thickness

For the thickness series, 20% of the aluminium was targeted for the UPHS barrier. While the actual aluminium content in the barriers was lower, it was still possible to capture the thickness effect as the resulting aluminium content did not vary too much between samples (remained within the range of 14-17%). All samples from this series demonstrate rectifying behaviour (Figure 68), and the knee voltage increases with barrier thickness, which is correlated to our simulation study on this matter (sub-section 3.2.2.3, Figure 59). However, there is also a discrepancy between our simulation and experimental data. Besides the already mentioned overestimation of knee voltage by our simulation in general, the dependences of knee voltage on barrier thickness differ. In our simulation, this dependence is significantly sublinear (not shown) while it is linear in the experiment (not shown). The slight superlinearity probably can be explained by somewhat higher aluminium content for the thickest barrier UPHS and therefore can be ignored. While there is no explanation for this difference in behaviour (sublinear vs linear), the absolute discrepancy between the experiment and model for UPHS with the thickest barrier actually decreases. From this observation, one can conclude that factor(s) causing overestimation of knee voltages in our simulation model become(s) less significant for UPHS with thick barriers.

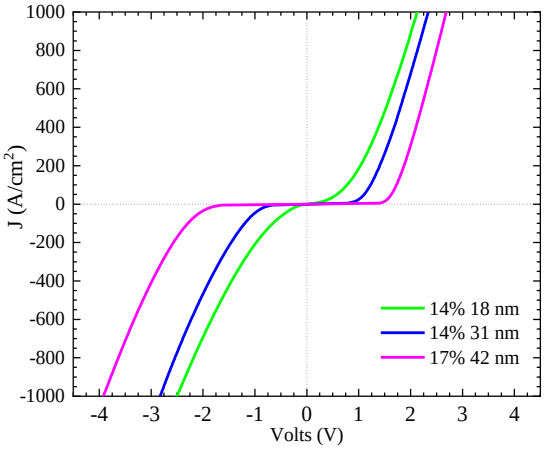

Figure 68: Experimental JV-characteristics of sample with varying barrier thickness.

From the above data, it can be concluded that at a fixed height of a barrier, there exists a certain thickness below which rectifying properties of an EBL will start to suffer (18 nm sample in Figure 68). On the other hand, excessive thicknesses of EBL might be not so helpful as, besides detrimental effects on hole transport, their ability to stop electron saturates. Nevertheless, in an actual experiment, this effect could not be observed up to ~40 nm.

3.4 Conclusion

In conclusion, this chapter is composed of simulations and experiments conducted to study vertical electron transport through an *i*-AlGaN barrier layer in UPHS.

Our results, summarized in Figure 69, show that both rectifying and non-ohmic behaviour are possible, unlike the previously published reports which failed to demonstrate the barrier effect of an UPHS. In most samples, the rectifying nature was observed and increased with increasing Al content in the AlGaN layer and its thickness. Some of the trends of experimental results are intuitive and can be explained by similar trends observed in simulations.

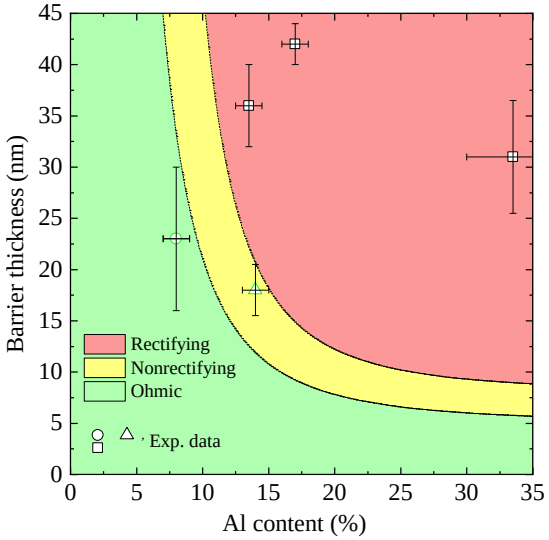

Figure 69: Experimental behaviour of AlGaN layer as a function of Al content and thickness in a UPHS. (Qualitative boundaries are drawn to show transition between different behaviours)*

Non-rectifying behaviour is also observed in our results in three specific conditions, i.e. a) at low 'Al' content (≤10 %) in the barrier; or b) at thin barrier thickness (≤15 nm); or c) if interruption is incorporated during growth of AlGaN layer. We have shown that fissures are formed on the top AlGaN surface during growth pause and can be the most probable cause for the ineffectiveness of AlGaN as a barrier obtained by previous researchers looking into this matter. Still, investigation is required to understand the impact of growth pause at the bottom interface and how it affects the AlGaN barrier efficiency.

Summarising our experimental results, it can be speculated that for an AlGaN layer, there exists a particular value of mole fraction and/or thickness nearing which the rectifying nature tends to reduce. Below these values, electrons stop seeing a barrier altogether, and ohmic behaviour is observed instead. At this point, it is hard to

* It was determined that the simulated data can be fitted to the experimental data (from XRD), for a limited range of values of aluminum content and barrier thickness. So, the scatter plot was constructed using the best fitted values used as centered for the same. Since, it was observed that the same data can be fitted by slightly increasing the alumnium content and decreasing the barrier thickness, so error bars were incorporated to convey the spread in the values.

come up with an assertive reason which can explain this behaviour. While it is intuitive, the transition from rectifying to non-rectifying behaviour occurs sharper than the simulation predicts. I can only speculate that there is more than one effect cumulatively affecting the current transport such as a reduction in Al content reduces the barrier height for an electron and the increased gallium content might increase the regions of low Al content providing the carriers with the number of passes while smearing interfaces can make it even easier in case of thin barriers.

However, significant disagreement between experimental results and simulation still exists. The simulations are still unable to predict the exact knee voltage in forward and reverse conditions. Even the model with smeared interfaces cannot match the experimentally observed behaviour, which suggests further work is required to understand the cause of symmetric behaviour. Furthermore, an open-ended question is the amount of smearing which needs to be incorporated into the smeared interface model.

Thus, the inability of basic models to replicate experiments shows the necessity for the incorporation of more complex models (e.g. 3D vs 2D) or additional effects (e.g. tunnelling, localization landscape theory) in addition to the existing ones needed to achieve further understanding and agreement with the experiment. Further study is required to fill this knowledge gap in our fundamental understanding of vertical electrons at the GaN/AlGaN interface which is beyond the scope of this qualification work.

A practical suggestion from the results presented in this chapter would lie in minimal compositional contrast with adjacent layers and thickness of EBL to assure its effectiveness in electron blocking. These values should be about ~15% and ~20 nm respectively. Furthermore, the effectiveness of an EBL would gain from its uninterrupted growth.

Chapter 4 Template development.

The absence of native substrates for low aluminium content AlGaN necessitates to growth of AlGaN heteroepitaxially. This is because available (although expensive!) bulk substrates of GaN and AlN are not suitable for direct growth of AlGaN on them, as it results in cracking in the former case and poor crystalline quality and surface morphology in the latter case, as has already been explained in chapter 1 and 2.

In this chapter, the core aspects of AlGaN growth, such as reactor conditions and the constraints of heteroepitaxy on quality and surface morphology of the buffer layer for an LED are described.

4.1 Planar Template Development

In our study of planar AlGaN templates, the following have been tried based on the literature: influence of an AlN-connecting layer, and low temperature (LT) AlN interlayers as a dislocation filter. Additionally, two new approaches have been attempted: nano-roughening to enhance the conductivity of the *n*-AlGaN layer and compositional grading for strain management of tensile stress caused by doping with silicon. Below, the results of these experiments are discussed and summarized.

Generally, epitaxial growth of ~2-2.5 µm *u*/*n*-AlGaN using MOCVD was grown on planar substrates under various conditions (Table 8). Our standard substrate is a "Kyma AlN/sapphire" which comprises a thin layer (~25 nm) of PVDNC™ AlN on a *c*-plane sapphire. Analysis of the quality and surface morphology of the AlGaN epilayer was carried out using X-ray diffraction (sub-section 2.1.3.2) and Normaski microscopy as described in Chapter 2 (sub-section 2.1.3.4). Specific details about the samples will be elaborated in each section, as well as a description of any variation in growth conditions.

Table 8: Growth parameter used for planar template development

Growth parameters	Values
Susceptor Temperature	1060-1160 °C
Reactor pressure	75-150 mbar
NH_3 flow / Total Flow	10-33%
Carrier gas	H_2, (15 %) H_2 + N_2

4.1.1 Substrates and initial attempts to grow on them

During heteroepitaxial growth of *u*-AlGaN layers directly on sapphire or on thin AlN/sapphire (Kyma Tech.), or on thick AlN/sapphire, it was found that the TDD is a function of AlGaN composition and thickness. Increasing the thickness of the epilayer, however, results in surface morphology deterioration and build-up of tensile strain (when doped with silicon) as seen from in-situ reflectance and wafer curvature monitoring. This limits the maximum thickness of a crack-free *u*-AlGaN layer, with the material quality of such layer being in the range of ~1-3×10^{10} cm^{-2}, which is not satisfactory. This is somewhat different from the behaviour observed in the past in others and our group for high aluminium-content AlGaN grown on moderate-quality AlN templates [20,130]. While surface morphology also deteriorates with thickness, its crystal quality is initially much better (defined by the initial AlN template) but deteriorates and does not improve with thickness [20,131].

According to Kyma, PVDNC AlN is columnar in nature i.e it comprises of oriented crystalline islands/columns[132]. A consequence of this inherent morphology is the existence of nanoscopic voids between individual islands which potentially results in a non-periodicity in the effective "lattice parameter". Epitaxial growth of AlGaN directly on the columnar AlN structure of Kyma substrates seemingly also initiates as a columnar one with the generation of excessive amounts of dislocations as these columns coalesce and join into a single crystal layer as reported by O'Connell et al.[133]. These effects combined together the considerable lattice mismatch which exist between AlGaN and AlN results in formation of "nano-pipes" and is attributed as the cause of high dislocation density of $1–2\times10^{10}$ cm^{-2} observed in an AlGaN epilayer.

The poor quality of AlGaN directly grown on our substrates leads us to explore several approaches described below.

4.1.2 AlN connection layer

An AlN connection layer as shown in the schematic Figure 70, was incorporated, between the Kyma substrate and AlGaN epilayer to refresh the surface and eliminate the non-periodicity. Details of the growth of these samples are provided in the sub-section 2.1.2.2 (P.51).

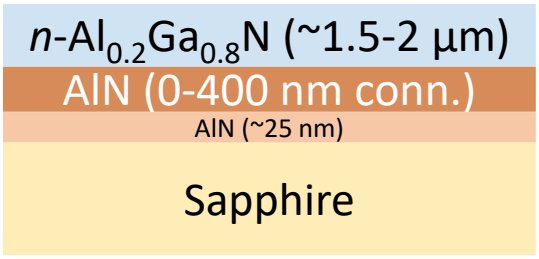

Figure 70: Schematic of the sample studied in the optimization of the AlN connection layer.

AlGaN material quality improves with the insertion of the AlN connection layer in both types of templates: i.e. either thin (~25 nm Kyma) or thick (~2 µm Tyndall template) as shown in Figure 71. In the case of AlGaN growth on thin AlN templates, insertion of an AlN connecting layer results in slight broadening in the FWHM of the 0002 reflection which suggests increase in the screw component of the dislocations. However, I can not assertively claim this because there are various other factors* such as wafer curvature, strain relaxation, etc. which can cause such small

* Factors elaborated by Moram et al. in P.19, Ref. 18.

deviations, whereas the significant reduction of screw dislocations in the case of a thick AlN template by the growth of an AlN connecting layer can be due to some other mechanisms, i.e. either removal or overgrowth of native oxides present on AlN surface[134]. These results indicate that the use of good quality thick (~1 µm) AlN as a buffer layer or template cannot be immediately justified as the quality of AlGaN epilayer degrades (cannot be retained) due to lattice-mismatch between AlGaN and AlN.[130]

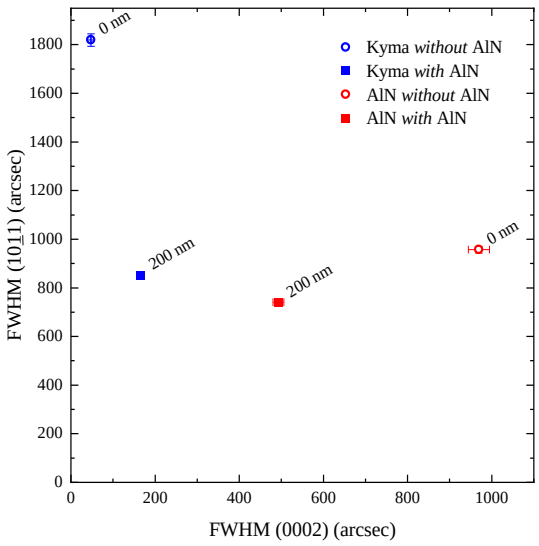

Figure 71: Effect of the initial substrate and the presence (w for with)/ absence (wo for without) of AlN connection layer on the material quality of AlGaN layer grown using conditions described in subsection 2.1.2.2 (P.51).[*]*

On the other hand, the reduction in edge dislocation density in the case of the Kyma template can be related to overcoming the initial non-periodicity of the lattice parameter, whereas for the thick AlN template, the reduction is marginal (i.e. the edge dislocation density difference between the two samples is susceptible to a typical variation observed in material quality over the sample). It can be largely said that the insertion of AlN helps reduce edge dislocation density. Further study of the influence of the AlN connection was studied in terms of the layer thickness as it is the only parameter which can lead to this effect.

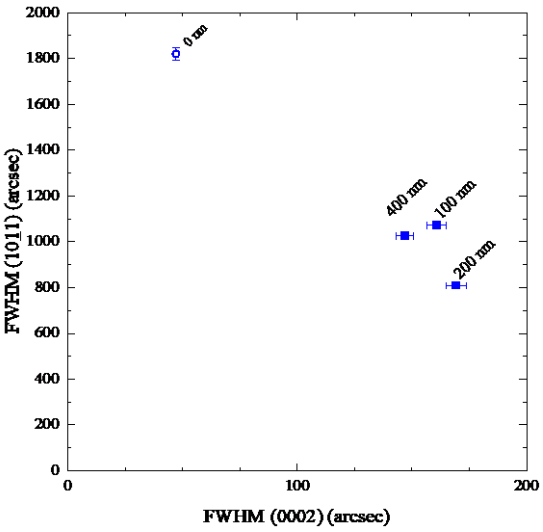

Figure 72: Effect of AlN connection layer thickness on the material quality of AlGaN layer.
*The thickness of AlN is shown as a label next to data points.**

The effect of an increase in the thickness of the AlN connection layer on the material quality of AlGaN is shown in Figure 72. The reduction in dislocation density

[*] Error bars on the FWHM values are based on the measurement described in the appendix.

is somewhat dependent on the thickness of the connection layer and gives the best results for connection layers of ~200 nm in thickness as shown in Figure 72. The data is limited to assertively assess the effect of AlN connection layer thickness but the results reported by Jayasakthi et.al.[135] instill confidence in our observation.

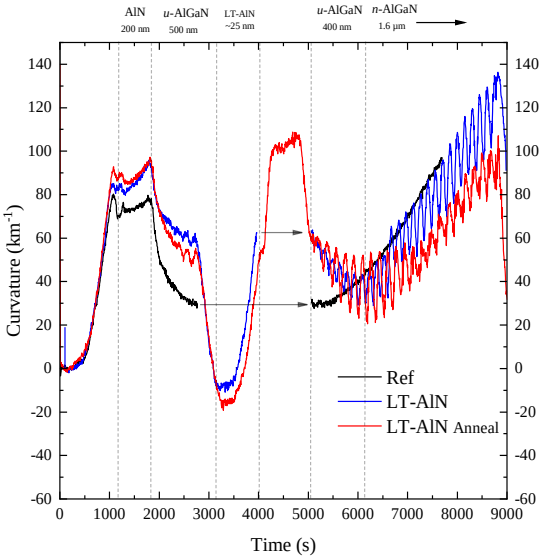

Figure 74 In-situ curvature during growth of LT-AlN interlayers.

Nevertheless, it can be confirmed (concluded) that an AlN connection layer enables a reduction in dislocation density, and it is better than the direct growth of AlGaN on AlN/sapphire templates (Kyma) as shown in Figure 72. This allowed us to reduce the dislocation density by more than ~4 times down to $<4\times10^{9}$ cm^{-2}.

Going further, implementing a 200 nm AlN connecting layer becomes our default approach for starting AlGaN growth on planar templates.

4.1.3 Low Temperature - AlN or AlGaN Interlayer (LT-AlN)

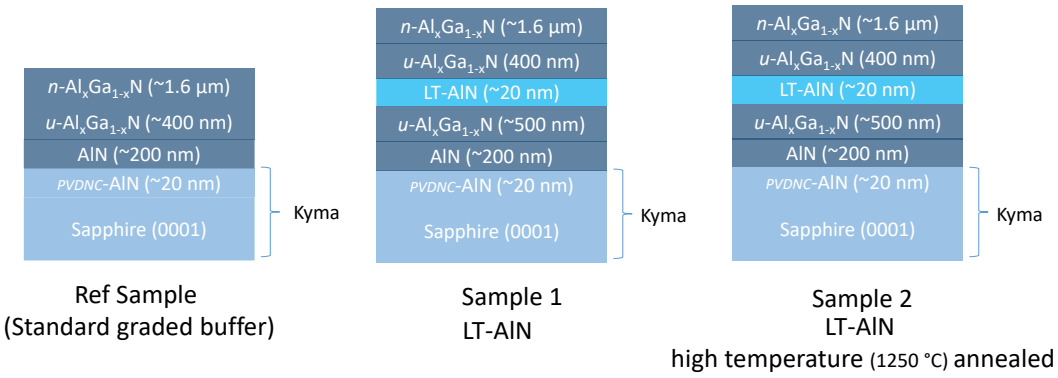

Figure 73: Schematic of samples with inserted LT-AlN in the undoped AlGaN region

In the early days of the development of epitaxial growth of GaN or AlGaN on sapphire, LT-AlN interlayers were extensively studied and were shown to be promising in reduction of screw dislocations [61,93–95]. Some reports also highlighted the tensile strain management [90–92] ability of LT-AlN/AlGaN interlayers when grown on

GaN. So, on this front, we studied a) prospects of dislocation reduction and b) tensile strain management behaviour. The specifics of the sample growth procedure followed are provided in sub-section 2.1.2.2 (P.51).

Using the ~200 nm AlN connecting layer approach described in the previous section, a low temperature (~600°C) AlN interlayer was inserted after 0.5 µm *u*-AlGaN grown at standard temperature, as shown in Figure 73. Two modifications of this approach were attempted; in one case growth of AlGaN was restarted immediately after bringing the temperature back to the AlGaN standard value (1060°C), while in the second case, the sample with AlN interlayer was annealed at a high temperature (1250°C) before restarting the growth of AlGaN (again at 1060°C). After both annealed and unannealed LT-AlN, we observed a reduction in the tensile strain as shown in Figure 75 where in-situ curvature measurements are presented, which matches previous reports[90] of LT-AlGaN interlayers on GaN. However, a dislocation density reduction could not be confirmed. On the contrary, a considerable increase in dislocation density was observed (Figure 75). AlN has a lower *a*-lattice constant than AlGaN and grown at LT it relaxes immediately so that AlGaN grown on top of it is subject to compressive strain initially, which however is overcome by doping-induced tensile stress as the material is heavily dislocated. So, from observed behaviours, one can conclude that only limited strain management is possible but without the possibility to improve the crystal quality of the final AlGaN, it has only limited use. Due to not promising results, it was concluded that it was not worth pursuing this approach any further.

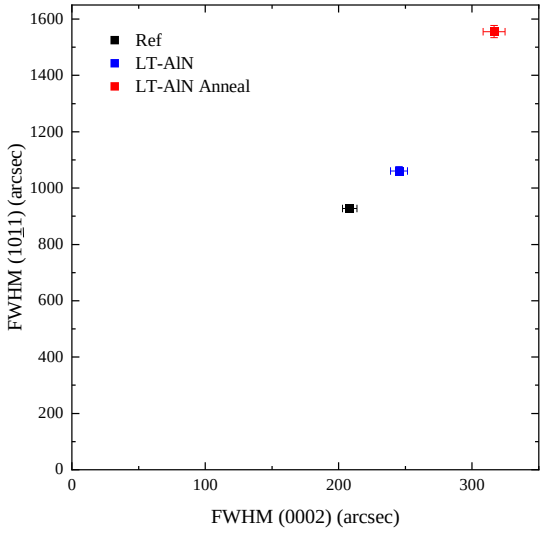

*Figure 75: Effect of LT-AlN interlayer on the material quality of the AlGaN epilayers.**

4.1.4 Compositional Graded Buffer

So far, I have not succeeded in significant reduction of dislocation density, in the previous approaches to grow *n*-AlGaN, since the critical thickness before the layer cracks was insufficient for substantial improvement of its quality.

A typical growth of a uniform composition relaxed *u*-AlGaN layer has residual tensile strain and can be observed in the in-situ curvature plot of Figure 76, *a*. This presence of initial residual strain is detrimental and is amplified during doping of the AlGaN buffer resulting in the generation of cracks upon exceeding a critical thickness as can be seen from Figure 76, *b*. The reasons for the building up of residual tensile stress and cracking of highly dislocated *n*-doped material were discussed in detail in Chapter 1 (subsection 1.2.4.3). A total thickness of ~1.5 µm was obtained, which is similar to what has been reported by Wang *et al.*[58]. It would be enough to mention here that the cracking is more severe in material with higher dislocation density.

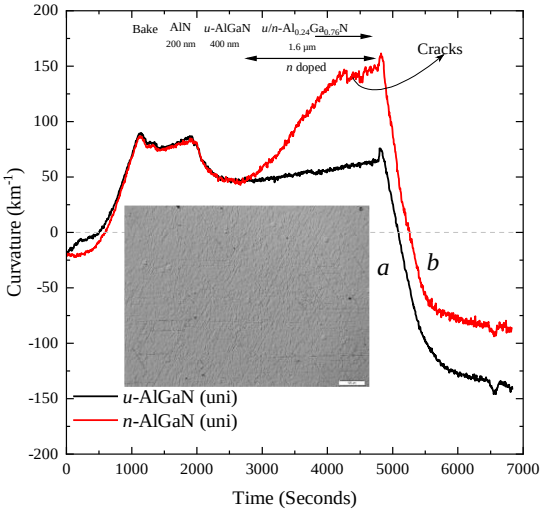

Figure 76: In-situ curvature measured during growth of (a) uniform u-$Al_{0.24}Ga_{0.76}N$ compared to (b) n-$Al_{0.24}Ga_{0.76}N$ (inset: showing cracks on the surface).

For lateral conductivity in UV LEDs, a thick *n*-AlGaN buffer is required, to achieve this without cracking during *n*-AlGaN growth. This leads to a kind of vicious circle, where increased thickness can help dislocation density but in itself lead to cracking. To escape from this "vicious circle" another approach needs to be implemented not directly involving dislocation density reduction.

Due to the greater in-plane lattice constant of $Al_xGa_{1-x}N$ compared to $Al_yGa_{1-y}N$ for $x < y$, compressive strain is generated when the former is coherently (fully strained) grown on the latter. Based on this principle, Khan *et al.*[136] devised and experimented with an approach, in which "step-like" discrete grading was implemented at $Al_xGa_{1-x}N/Al_yGa_{1-y}N$ interface. It is hard to say whether the approach is useful in managing the tensile strain of AlGaN without a detailed analysis. However, we implement a continuous grading approach, in which AlGaN composition is graded

over the buffer thickness (~1.6 µm), our logic behind the continuous grading of the composition is to gradually generate the compressive lattice mismatch while the lattice of overgrown material (low Al-content AlGaN) adjust to the lattice of under layer (high Al-content AlGaN) material. To test the impact of grading the AlGaN buffer layer, samples with graded AlGaN buffer were implemented with and without doping.

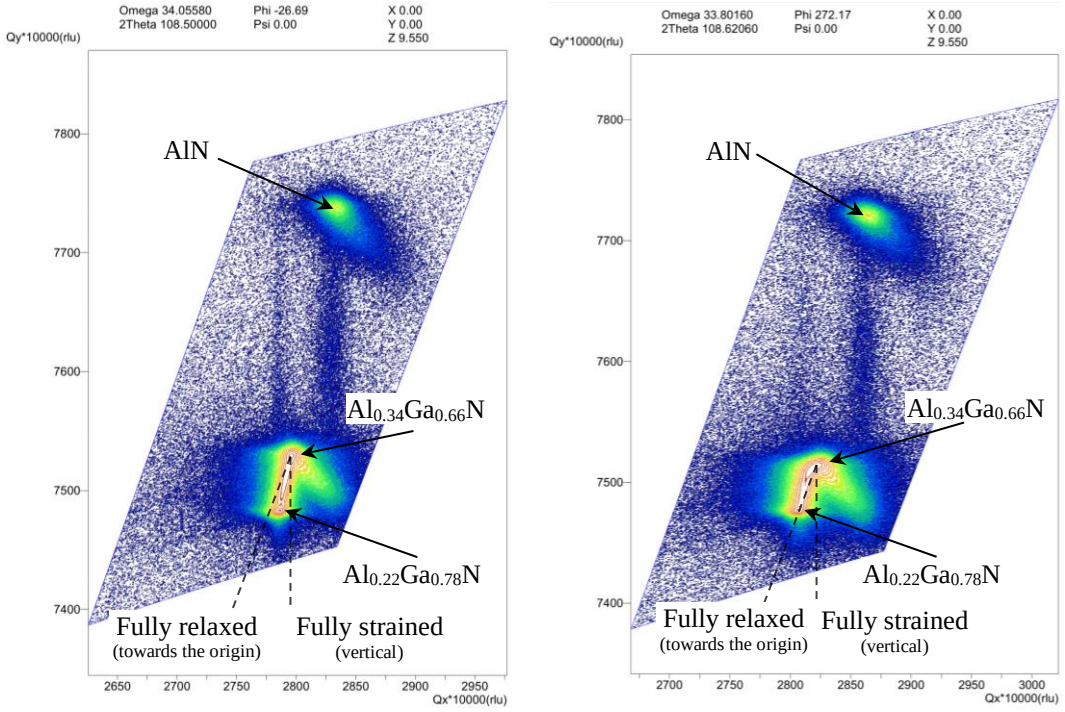

a *b*

Figure 77: Reciprocal space map (105) a) u-AlGaN buffer layer and b) n-AlGaN buffer layer. The Al Content in the AlGaN layer is linear graded from ~33-22%.

First, an undoped graded AlGaN buffer was grown and its corresponding reciprocal space map is shown in Figure 77, *a*, in which initially an unintentionally doped ≈34% AlGaN is grown on top of our optimised AlN connecting layer on Kyma (AlN/sapphire) substrate with the aim to let it almost fully relax with respect to AlN to its natural in-plane lattice constant. In reality, only partial relaxation (of 50-70%[*]) was achieved. For this reason, AlGaN with aluminium content gradually ramped down to our target of ≈22% and is not fully strained with respect to the ≈34% AlGaN. It relaxes further and the corresponding peak elongates neither along a fully strained

[*] In the undoped graded AlGaN buffer (Figure 77, *a*) the relaxation value changes from 50% for the high aluminium content material to 53% for the low Al content region, whereas in the case of doping of the graded buffer (Figure 77, *b*) this varies from 60 to 70%.

direction nor fully relaxed as can be seen from the reciprocal space map in Figure 77, *a*. Nevertheless, as a result, grading of aluminium content led to the building up of some compressive strain which is also clear from curve *1* (green curve) in Figure 76.

In the second test sample, silicon doping was implemented together with grading. In this case, according to the reciprocal space map in Figure 77, *b* AlGaN "overrelaxes*" i.e. goes beyond the fully relaxed direction causing a lot of tensile stress which is manifested in an in-situ curvature increase (curve *2* in Figure 76). Weinrich *et al.*[57] and Forghani *et al.*[137] have explained this as a dislocation-climb effect caused due to doping with silicon. Despite the strong tensile stress, it was not enough to generate cracks, and the main reason for that is that it is partially compensated by the compositional gradient inducing some compressive stress. Overall, the thickness within which aluminium content is graded was optimised aiming to maximise the total thickness of *n*-AlGaN before it cracks.

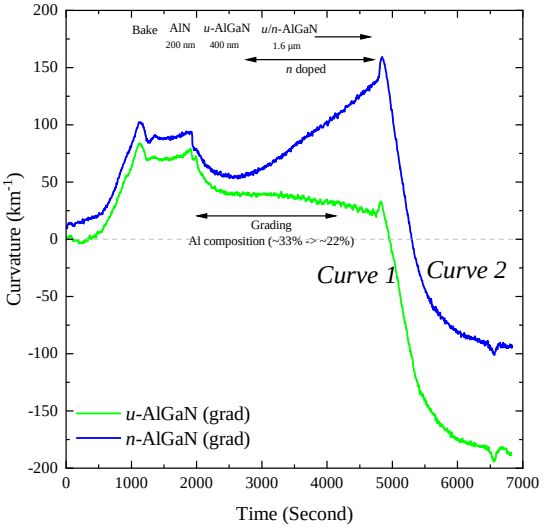

Figure 78: In-situ curvature measured during growth of graded u-AlGaN (curve 1) compared to n-AlGaN (curve 2). The Al Content in the AlGaN layer is linear graded from ~33-22%.

As a result, up to 2 µm crack-free *n*-AlGaN has been prepared with a total thickness of up to 2.5 µm. This was achieved for layers with electron concentration up to ~2×10^{18} cm^{-3} which were found to be suitable as buffers for UVA LEDs.

* In the reciprocal space map for the undoped sample with only compositional grading (Figure 77, *a*) lies between the strained (pseudomorphic) and relaxed lines shown on the plot suggesting that some degree of relaxation occurs in the film but still the final strain state of the film has some amount of residual compressive strain. On the contrary, the sample with doping (Figure 77, *b*) is completely relaxed in the RSM plot. This can be observed from the centre of the compositional distribution going over the drawn relaxed line and finally ending on the relaxed line as well. This explanation is empirical in nature and lacks quantitative values as it is very hard to completely separate out the effect of relaxation from compositional change at various growth stages in the sample.

4.1.5 Surface morphology issues

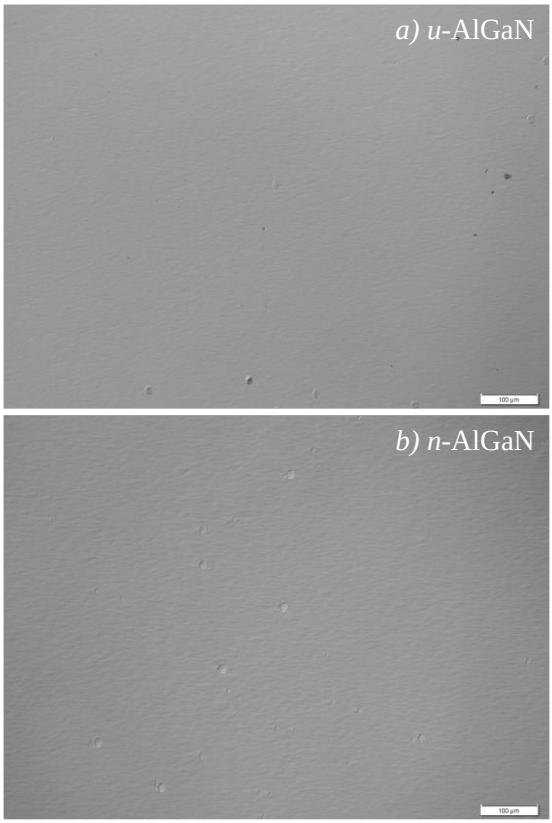

Figure 79:Normaski images of graded AlGaN buffer: a) without and b) with doping.

Although reasonably thick and heavily doped crack-free *n*-AlGaN was achieved as described above, their ultimate surface morphology was found to be roughened (Figure 79). The driving force of these µ-features is the surface relaxation of compressive stress in a low aluminium-content AlGaN layer grown on AlN. During the relaxation process spiral growth occurs around a screw-type threading dislocation resulting in the formation of hillocks[138]. The hillock density is dependent on various material and growth parameters such as screw dislocation density, doping, V/III ratio[20,139], etc. Hillocks are detrimental to a device's performance and should be minimized. This raises the question of why hillock density is less in standard GaN conditions.

AlGaN here was grown using growth conditions typical for GaN (V/III = ~1000, p =150 mbar, T = 1060°C). The resulting layers though were found with much better surface morphology but were ~2 times thinner than initially expected. These conditions have been found to be non-optimal for AlN/AlGaN growth due to ammonia and TMAl pre-reaction[140]. Also, achieving a high aluminium fraction was problematic as the pre-reaction rate scales with the absolute flow of TMAl.[141–143] To mitigate this issue and to achieve more optimal utilization of precursors, the reactor pressure was reduced to 75 mbar, which is equivalent to halving the absolute concentrations of both TMAl and ammonia. Later, it was found that a similar approach was also suggested by Lobanova et al.[143]

Overall, the surface morphology (Figure 80, *a*) at standard AlGaN conditions (75 mbar with a low V/III ratio) is much worse than standard GaN conditions (150 mbar with a high V/III ratio) shown in Figure 80, *b*. On the other hand, the newly introduced "hybrid", - because they share features of GaN (high V/III ratio) and AlGaN (75 mbar), - conditions give both good surface morphology (Figure 79, *b*) and decent control of aluminium content. For this reason, these *hybrid* conditions became our default conditions for growing buffer layers for UVA LEDs.

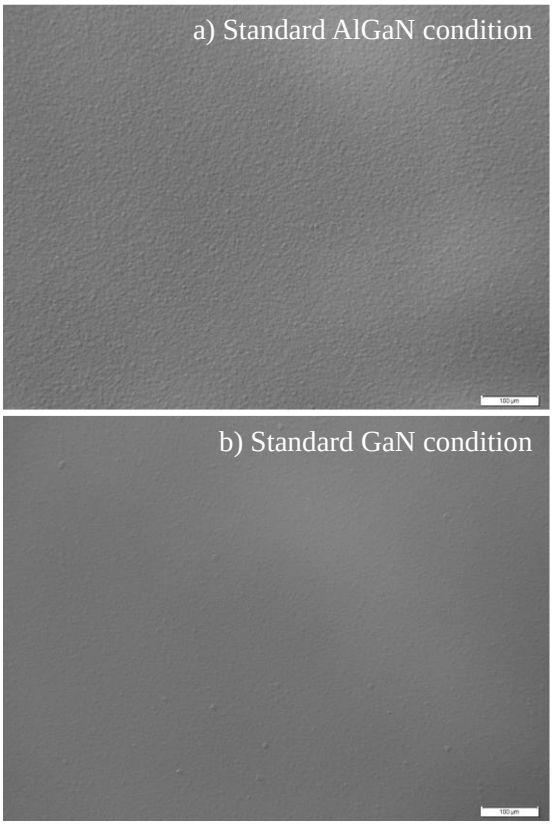

Figure 80:Normaski images of AlGaN buffer grown in a) standard AlGaN and b) standard GaN conditions.

4.1.6 Conclusion of Planar Template Development

In conclusion, direct growth of $Al_{\sim 0.2}Ga_{\sim 0.8}N$ on Kyma substrate is better in quality compared to sapphire. This quality can be further improved, i.e. dislocation density can be reduced with the incorporation of an AlN connection layer. Another planar technique to improve quality such as LT-AlN interlayer, did not give promising results. Since it was realized that the scope for quality improvement using planar techniques is very limited.

To improve the quality further, an increase in the total thickness was understood as a straightforward way. For this, however, one needs to manage the doping-induced build-up of tensile strain to avoid cracking of the material. For this, grading of the composition during the growth of the buffer layer was explored. It was shown to be able to increase the thickness of the doped part of the buffer from ~900 nm to ~1.6 µm.

Another aspect that was addressed in this section was surface morphology and particularly efforts to reduce hexagonal hillock density. Typical GaN growth conditions (high V/III ratio, 150 mbar) were identified as inhibiting hillock formation

but had the drawback of strong NH_3-TMAl pre-reaction and limited range of composition achievable. As a compromise, mixed growth conditions referred to as "hybrid" were successfully implemented to both achieve good surface morphology (provided by a high V/III ratio) and suppress the pre-reaction (provided by low pressure).

The learning from all the above approaches and using "hybrid" conditions for *n*-doped AlGaN allowed us to achieve smooth, crack-free, conductive, and thick enough buffers that later were successfully implemented in planar *c*-plane LEDs for 320-340 nm spectral range.

4.2 Patterned Template Development

Irrespective of whatever planar techniques we have attempted/implemented in the previous section, we were unable to reduce the dislocation density to values less than ~4×10^9 /cm^2 for $Al_{\sim0.2}Ga_{\sim0.8}N$ buffer. In order to further improve the quality of the template by reducing edge dislocations, we explored the overgrowth of AlGaN on µ-patterned templates.

As mentioned in Chapter 1 (subsection 1.2.4.4), in view of the inability to reduce the dislocation density of heteroepitaxial AlGaN grown using standard planar techniques, extensive work has been carried out in the area of template development using micro/nano-patterning. The intent of these previous studies was generally quite focussed on quality improvement, and less detailed on the overgrowth mechanisms defining the evolution of surface topology under various growth conditions. While my target also was to improve the quality of AlGaN templates, the additional goal of this study is to explore the topological evolution of a patterned surface and understand the growth mechanisms behind it.

The overall idea of the patterning-overgrowth approach is to remove as large a portion of the original (poor quality) material as possible, and then drive coalescence of the patterned structure back to a planar layer (ideally of much better quality). For this reason, the first objective in this study was finding growth conditions which favour *c*-plane expansion. As the second objective was to study overgrowth mechanisms and to get more insights into the competition of various crystallographic orientations, the patterned structure should contain a plurality of concave and convex surfaces. In this regard, µ-holes are a good model pattern, and triangular arrays of them in the form of a µ-honeycomb (µ-HC) were chosen to conduct this study.

In this study, initial templates for overgrowth were obtained using patterning of low/moderate quality AlN and relaxed AlGaN grown as described in the previous section. In the process of patterning, the removal of ~25-90 % of the dislocated material is achieved by a combination of dry and wet etch forming µ-HC structures. These templates are then used as an initial substrate for lateral overgrowth of AlGaN. The exact fabrication procedure is detailed in Chapter 2 (P. 66).

Attributes (such as quality, composition, surface morphology, etc.) of an AlGaN epilayer are influenced by various growth parameters (such as substrate temperature, V/III ratio, reactor pressure, growth rate, carrier gas, etc.). This suggests

that AlGaN has a huge multi-variable growth parameter space and exploring it is time-consuming and expensive. So, our approach would iteratively explore various regions of the growth parameter space while optimizing the epilayer thickness aspect ratio of the µ-pattern and growth conditions. This will help us learn and progress towards our objective.

4.2.1 AlGaN overgrowth of AlN µ-honeycomb (~1 µm holes)

4.2.1.1 Sample Description

In this first iteration (Iteration-1) of our overgrowth experiments, the µ-HC structure was prepared from AlN epilayers. The µ-HC structure is a triangular array of hexagonal holes (~1 µm in diameter with nearly vertical *m*-oriented sidewalls) with 3 µm pitch and oriented in such a way that the rows of holes are aligned along AlGaN *a*-direction (Figure 81). Details of the fabrication of these samples were described in Chapter 2 (P. 67).

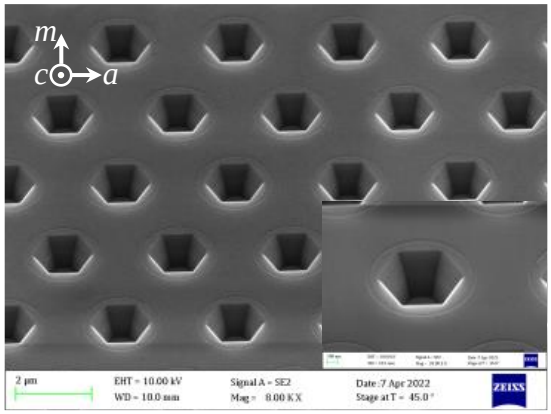

Figure 81: SEM (secondary electron) image of as fabricated AlN µHC.

4.2.1.2 Scope of experiment

In this experiment, various AlGaN overgrowth conditions shown in Figure 82 were studied on AlN µ-HC. Close observation of Figure 81, shows that only a small fraction (~15%) of the original material is removed in this structure. Since, our main objective in this experiment was to investigate a range of growth conditions, to find ones suitable for their coalescence into smooth planar layers rather than to obtain a reduction in dislocation density. This was driven by the idea that smaller holes should be easier to coalesce. In this sample set (iteration-1), the growth parameters studied centred around our standard AlGaN conditions (1060°C,

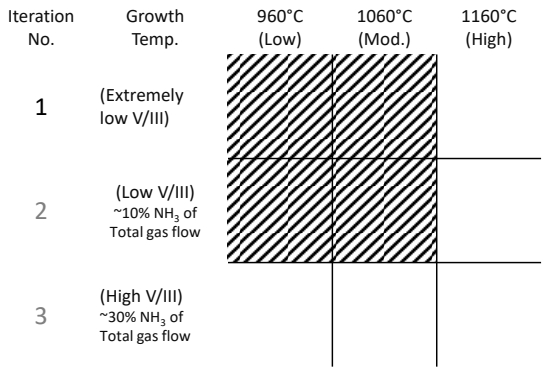

Figure 82: Growth parameter space explored in Iteration-1.

75 mbar, low V/III ratio, carrier gas H_2): the growth rate, V/III ratio, substrate temperature, and carrier gas were varied. Figure 82, shows the selected region of V/III ratio and growth temperature studied in Iteration-1.

4.2.1.3 Results and discussions

Since our samples are still effectively *c*-plane dominated, the initial growth of AlGaN on them is similar to that on purely planar (not patterned) templates. Initially, the growth of AlGaN shows strong roughening which was observed using in-situ reflectance (not shown). This is due to AlGaN trying to grow pseudomorphically which initially happens. However, this builds up significant compressive strain, which the material tries to release through 3-D growth. Further, even this is not enough, and plastic deformation of material happens through the generation of plurality of dislocations as described in Chapter-1 (sub-section 1.2.4.2) in more detail. Once the compressive strain is mostly released, there is no more driving force for 3D growth and thus surface morphology improves to a degree.

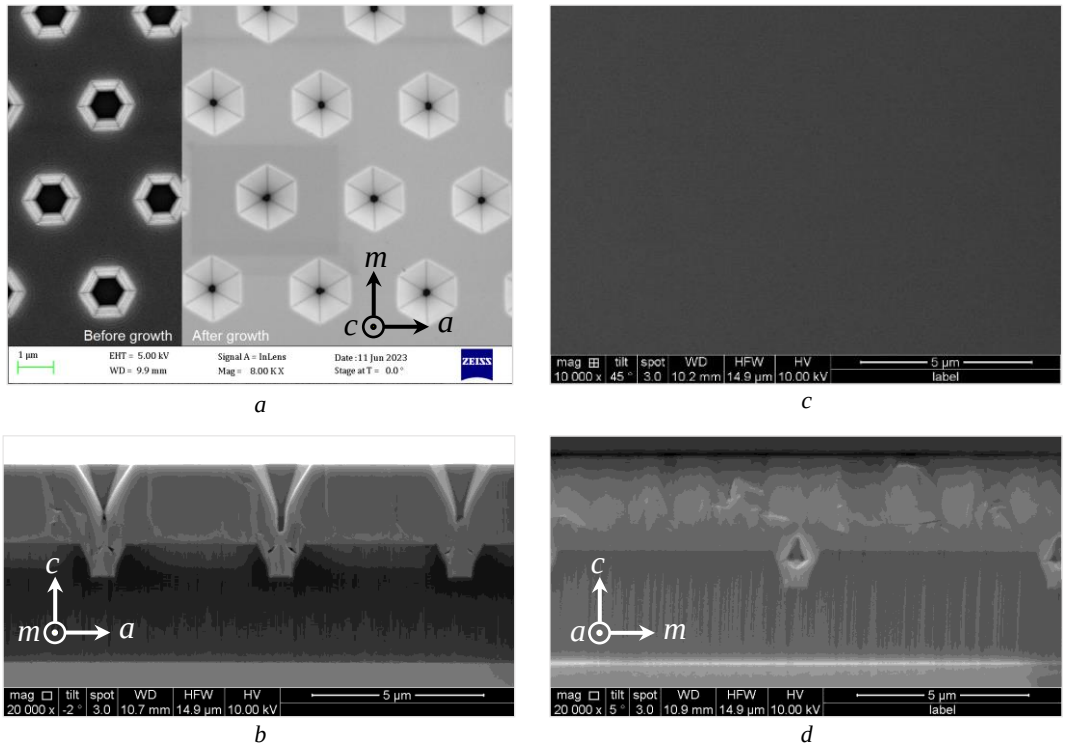

Figure 83: SEM (secondary electron) images of two samples grown in two different growth conditions are shown in top- and cross-section view.
Formation of V-pits with semi-polar facets (a: top-view of a sample before (leftside) as fabricated and after over-growth (rightside) shown for ease of comparison and to illustrate rotation of the V-pit, and b: cross-section along $(11\bar{2}0)$) and,
Coalescence conditions (c: top-view, d: cross-section view along $(10\bar{1}0)$).

Overall, the topological evolution of µ-holes can be categorised into two types: a) semi-polar facet formation and b) coalescence (*c*-plane expansion). Across a broad range of growth parameters, the initial µ-HC structure evolves into an array of hexagonal holes with semi-polar facets {11$\bar{2}$2} i.e. *a*-plane tilted as can be seen from Figure 83, *a*. In other words, a transformation of the initially hexagonal hole occurs so that it apparently "rotates" by 30°. The exact mechanism of such a transformation will be discussed in more detail later, in the section semi-polar facet formation (P. 139). So, the majority of growth conditions favour the formation of semi-polar facets.

The only sample from this series which showed coalescence of AlN µ-patterns was the one grown at a moderately low temperature of 960°C and rather extremely low V/III of ~38 (Figure 83, *c* and *d*). Similar results were also observed by Armstrong *et al.* for AlN µ-holes[144]. The growth is lumpy in nature but nevertheless leads to *c*-plane expansion. The exact mechanism of AlGaN coalescence at these conditions is not clear but as it will be shown later, the relative growth rate between *c*-plane and semi-polar facets tends to reduce. Further speculation on this matter will be given in P. 149. Strong supersaturation of group-III adatoms (in deficiency of N adatoms) causes the formation of additional steps through the nucleation of islands. This is similar to the growth of nitrogen polar GaN on low miscut substrates[145]. While the surface morphology was found to be recoverable by increasing temperature upon full coalescence of the µ-HC structure, the sample appeared brownish upon ex-situ visual inspection. Most probably, the coloration is due to high concentration of N vacancies or incorporation of other impurities in these extreme low V/III ratio conditions. The crystal quality of all the samples showed marginal or no change. This might be due to the low volume of material being replaced by overgrowth, as well as AlGaN relaxation on lattice mismatched AlN µ-HC templates.

In conclusion, growth parameters suitable for conversion of as fabricated holes into inverted µ-pyramids (V-pits) with well-defined semi-polar {11$\bar{2}$2} facets were identified. The conditions enabling coalescence were also obtained however were found to be not suitable for practical use due to non-transparency for visible (and most probably UV) light. So, we further continued our work on µ-HC structures to explore a wider space of growth parameters. In an attempt to achieve an improved quality template, we increased µ-hole size to significantly reduce the fraction of left original (poor-quality) material.

4.2.2 AlGaN overgrowth of AlGaN µ-HC (~1 µm holes, expanded)

To avoid the generation of dislocations as a result of plastic deformation of AlGaN due to its lattice mismatch compared to AlN when grown on the latter, in this second iteration (Iteration-2), the AlN base template was replaced by 1.6 µm-thick already* relaxed $Al_{0.2}Ga_{0.8}N$ layer (Figure 84) patterned into a µ-HC structure. Another difference here was an increased diameter of µ-holes. The idea here was to take a relaxed AlGaN template with whatever dislocation density is naturally occurring in it because of its plastic relaxation and pattern it in such a way that the majority of the poor-quality material (with dislocations in it) is removed. The resulting µ-HC structure is then overgrown, and the newly grown material should ideally be of a much better quality.

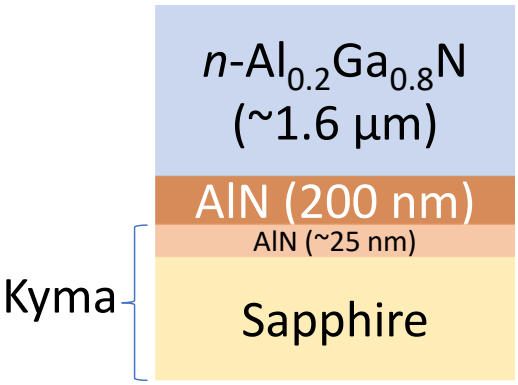

Figure 84: Schematic of base template used.

4.2.2.1 Sample description (AlGaN 1+µ-HC)

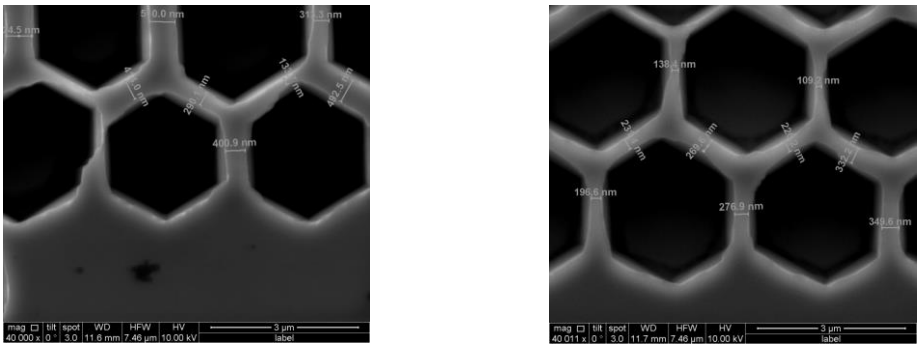

a *b*

Figure 85: SEM (secondary electron) image of the initial AlGaN µ-HC sample A(a) and B(b).

AlGaN overgrowth experiments were carried out on two samples, referred to as A and B (Figure 85). The intent behind the experiment was to study two major aspects of the µ-HC patterns, i.e. effects of a) the amount of residual material, and b) the aspect ratio of individual µ-holes on surface morphology evolution and overall quality of the resulting material. For this reason, sample A has on average smaller size of µ-holes and a greater aspect ratio of the µ-holes (relatively deeper rather than wider) whereas sample B has on average larger lateral size but shallower µ-holes. The growth

* As opposed to the AlN µ-HC where AlGaN relaxes as it grows.

was carried out in AlGaN conditions optimised for semi-polar facet formation in the previous experiment (Iteration-1).

4.2.2.2 *Scope of experiment*

Another aim of this experiment was to study surface morphology evolution during growth where conditions favour semi-polar facet formation (Figure 86). So, a series of growth runs was carried out aiming for AlGaN thicknesses from 0.5 to 2.5 µm, with a step of 0.5 µm, where both samples were co-loaded next to each other. The exact growth conditions were chosen based on the experiments of AlN µ-HC structures with the only difference of reduced growth rate by a factor of 2 (1060°C, 75 mbar, low V/III ratio, carrier gas H_2).

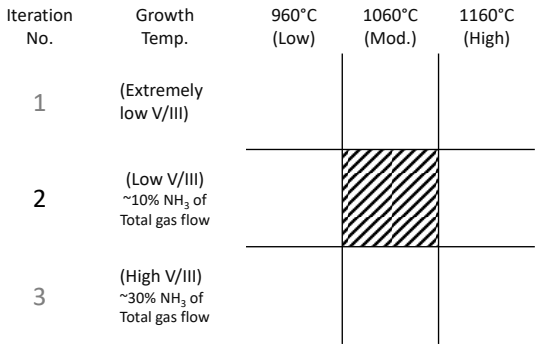

Figure 86 Growth parameter space explored in Iteration-2

4.2.2.3 *Results and Discussion*

As expected, semi-polar plane formation during overgrowth was observed in both samples (Figure 87). The overall area of the semi-polar plane increases with increasing in AlGaN thickness from 500 nm to 2.5 µm*. In the initial stage, this happens due to inward growth along non-polar orientations and *c*-plane area shrinking. Due to the particular orientation of the µ-HC array relative to the wafer flat (rows of µ-holes are orientated along the AlGaN *m*-axis), *c*-plane shrinkage only occurs until it is locked into triangular areas in between three adjacent µ-holes. This happens around a thickness of ~1.5 µm and forces semi-polar facets (Figure 87, *c*) to be locked to a particular crystallographic orientation of $\{11\bar{2}2\}$. At the same time, initially irregular/circular shape of µ-holes convert into hexagons. In more detail, semi-polar plane formation i.e. growth evolution in a µ-hole will be discussed in the next section.

Another feature of overgrowth on µ-HC structures with different aspect ratios of µ-holes consists of the development of parasitic/unwanted growth in the tunnel region when it is close to closure (arrowed Figure 87, *f*). Such unwanted growth on semi-polar facets was observed in sample B after about 1.5 µm whereas it was not

* Only a subset of the entire dataset is shown in Figure 87.

observed in sample A even till 2.5 µm. A closer look at this issue indicates that the main cause lies in competition between growth on µ-HC sidewalls and in the bottom of µ-holes. In sample B as the growth exceeds about 1.5 µm, the distance between the bottom edge of the semi-polar facets and the surface of the material grown inside the µ-hole decreases to zero so that parasitic growth starts "crawling" up the semi-polar facets. The exact mechanism of this will be discussed in the next section. It is enough to say here that to avoid the "parasitic" growth the initial pattern needs to satisfy certain conditions i.e. etch depth should approximately be equal to or greater than the hole diameter. This was implemented in the next series of the experiment (Iteration-3).

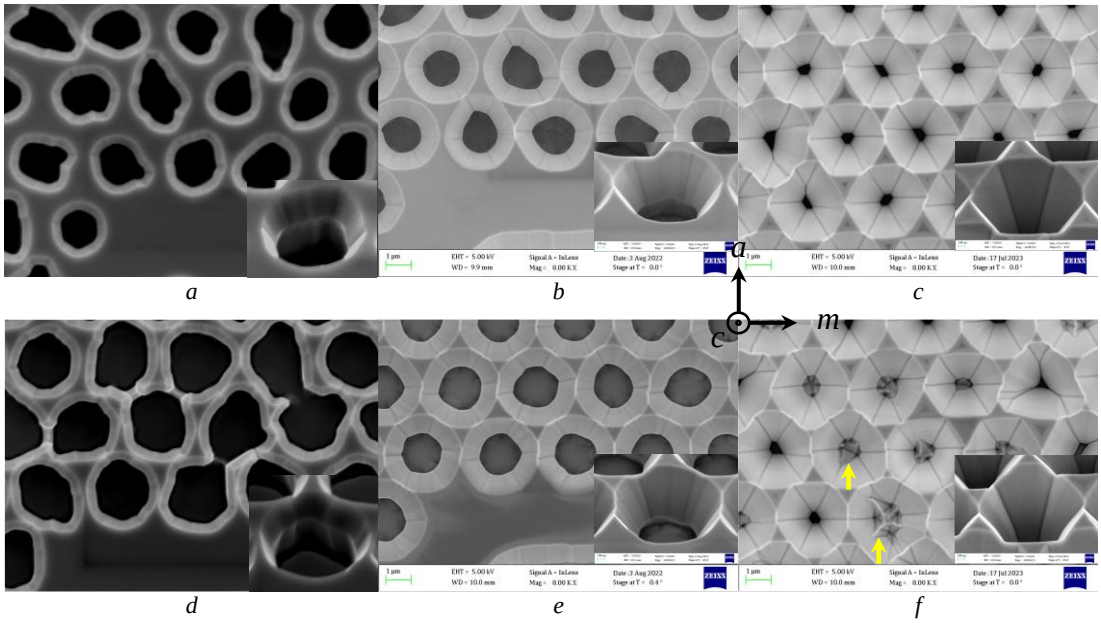

Figure 87: SEM (secondary electron) images of µ-HC topology for sample A (a-c) and B (d-f) after 0.5 (a, d), 1.0 (b, e), and 2.0 µm (c, f) of AlGaN growth.

XRD and PL results for these samples are ambiguous. On one hand, we did not observe radical improvement in the FWHM calculated from the ω-scan of either 002 or 101. This is probably because the samples did not coalesce and had non-uniform features in the initial patterns. Nevertheless, there is some improvement in the XRD quality when compared to a planar reference (Kyma substrate) sample grown in parallel and compared to the initial AlGaN template from which the µ-HC structure was fabricated. On the other hand, photoluminescence (PL) measurement suggests an improvement in the optical quality of the overgrown (new) material. Peak PL intensity increases with the effective area of the semi-polar planes compared to the reference

planar sample. So, this makes it difficult to judge whether is it appropriate or not to conclude the direct XRD characterization of this type of structure.

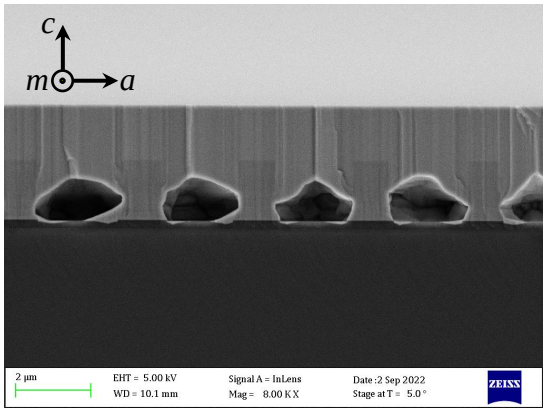

Figure 88 Coalescence of GaN grown on sample B. (image acquired using secondary electron detector)

Since none of the samples coalesced when overgrown with AlGaN using our standard AlGaN conditions, an additional standalone experiment was carried out where the same µHC structure (sample B) was overgrown with GaN. Sample B (µ-holes deeper rather than wider) was chosen for overgrowth with 2 µm thick GaN to avoid potential issues with parasitic growth. This growth resulted in the formation of a completely coalesced layer, a cross-section view of which is shown in Figure 88.

In conclusion, standard "AlGaN" growth conditions favour the evolution of µ-HC structures with initially nearly vertical sidewalls into structures with hexagonal V-pit-like holes with crystallographic facets of $\{11\bar{2}2\}$ orientation. It was found that the aspect ratio of µ-HC is an important parameter which can prevent unwanted growth on the semi-polar facets. The etch depth of a µ-pattern should be at least not much less (no more than approx. 20%) or (better) greater than the hole diameter. Although overgrowth allows some curing of initial pattern non-uniformities, for best results it is desired to minimize them in the initial patterns. Furthermore, it was evident that coalescence of a concave µ-structure is possible if suitable growth conditions can be found within the growth parametric space.

These learnings were implemented in the next iteration where a hole diameter of more than 2 µm was achieved using a suitable optical lithography mask and thus resulted in much more regular initial µ-HC structures.

4.2.3 µHoles- ~2 µm (Diameter)

In the previous iterations, the explored AlGaN growth parameter space favoured semi-polar plane formation. We also learned that to avoid "parasitic" growth, an optimized aspect ratio of the µ-pattern with respect to the template thickness is required.

Another reason behind pursuing µ-hole of 2 µm is based on the premise that lateral growth of material generates minimum or no dislocation, leading to an increased volume of low dislocation density (good quality) material in the template. However, the literature highlights that the point of coalescence (coalescence front[14, 15]) may generate a dislocation or a pit. Overall, the total dislocation density generated in this case, considering one dislocation at the core of each hole will be still only ~10^7 cm^{-2}. This should result in a two orders of magnitude less dislocation density than our initial material is grown conventionally (heteroepitaxial on sapphire or Kyma).

The results of this section and their discussion are mostly based on my published journal paper[100] authored by me and co-authored by my supervisors and where my contribution is substantial (I am the first author).

4.2.3.1 Sample description.

Based on the above reasons, in the third iteration a new mask with larger µ-holes (of 2 µm in diameter) was used for the fabrication of µ-HC on ~2 µm *u*/*n*-AlGaN grown on AlN/sapphire Kyma wafers with average dislocation density of ~4×10^9 cm^{-2} was used as a base template. As described in Chapter 2 P. 69, µ-HC structures with hexagonal µ-holes that are adjacent to each other with their apexes (Δ-type) and with their sides (Y-type) were fabricated (Figure 89).

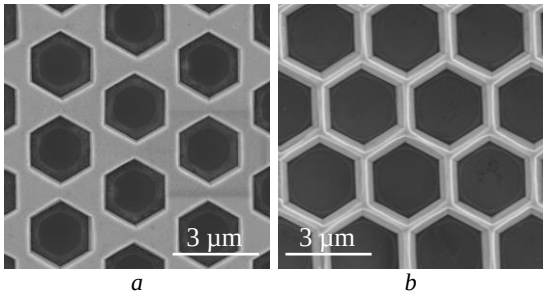

Figure 89 SEM (secondary electron) image of AlGaN µ-HC
a) Δ-type and b) Y-type[100]

So, since we had a more refined, regular and optimized new µ-HC template. Our initial plan was to test and reproduce the results of previous experiments.

4.2.3.2 Scope of the experiment

To start where we left off the second iteration, the first experiment was to carry out GaN overgrowth. The result (coalesced layer see below) made us believe that it is worth to investigate an expanded space of growth parameters while trying to identify conditions suitable for the coalescence of AlGaN. So, the revised plan was to understand these two possibilities: a) regular crystallographic semi-polar planes with

funnel closure and b) coalescence (recovery to a planar layer) through *c*-plane expansion.

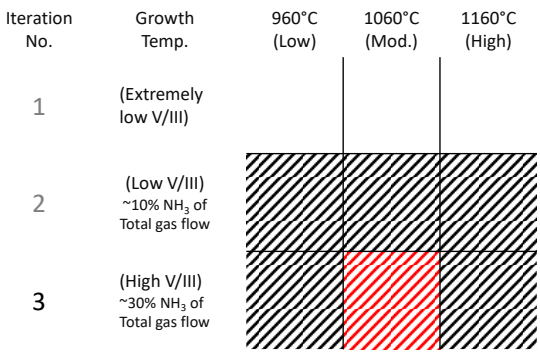

Figure 90: Growth parameter space explore in Iteration-3

Since the growth parameter space is huge, there exists a large number and ranges of parameter variation possible in principle. To optimise the search process in Iteration-3 to find conditions suitable for the planarization of AlGaN µ-HC structures, it was decided to start from GaN growth conditions (red box in Figure 90), which were proven to be suitable for coalescence of at least GaN. Further growth parameter space was expanded as shown in Figure 90.

The effect of substrate temperature, V/III ratio, and carrier gas on the overgrowth of AlGaN on µ-HC are studied to find conditions favouring either *c*-plane expansion leading us to the coalescence of µ-HC, or single crystallographic orientation semi-polar facet formation. These conditions are then to be further pursued in a systematic manner to understand the growth morphology evolution during coalescence and semi-polar facet formation.

4.2.3.3 *Results and Discussion*

GaN overgrowth

Initially, a series of test growths of GaN on Δ-type samples using standard GaN conditions (1060°C, 150 mbar, NH_3: 33% of total flow, which corresponds to a V/III ratio of ~1000) was undertaken to study the evolution of surface morphology. This experiment resulted in a straightforward *c*-plane expansion and complete coalescence of µHC structure into a planar layer within ~2.5 µm of total growth (Figure 91). This result is rather expected as it had already worked in Iteration-2. Moreover, exactly these conditions are used in standard GaN on sapphire growth after annealing the low-temperature nucleation layer (NL)[48], and lead to the coalescence of NL islands into planar layers.

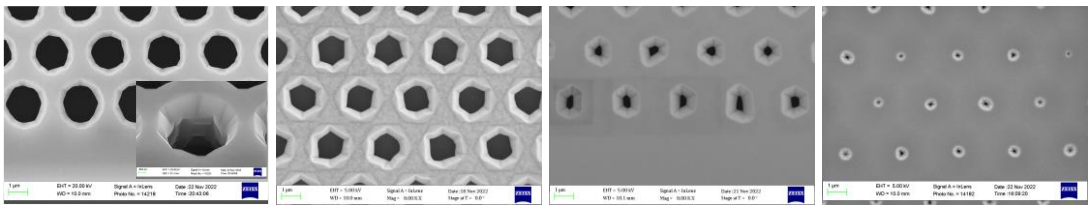

a *b* *c* *d*

Figure 91 Topology evolution on Δ-type during GaN overgrowth.
a) 0.25 µm, b) 0.5 µm c) 1.0 µm, d) 2.0 µm
(image acquired using secondary electron detector)

These GaN conditions were then used as a starting point for our study of AlGaN overgrowth since the main aim of this study initially was to coalesce µ-HC, and our target material contains only about 20% of nominal (corresponding to that in a planar reference sample) aluminium content.

AlGaN overgrowth using standard GaN conditions.

When an attempt to implement the above growth conditions was undertaken to deposit 2 µm of AlGaN (on a planar reference wafer co-loaded together with a patterned sample), no coalescence was observed instead V-pits with hexagonal base were formed with well-defined crystallographic semi-polar facets (Figure 92) with almost complete elimination of the original *c*-plane. The formation of semi-polar facets occurs as a result of competition between pluralities of crystallographic orientation present in the initial µ-HC. While detailed data on surface evolution will be presented later, it is worth noting already now that growth initiates along *c*-plane and non-polar planes. A semi-polar plane appearing in between them can indicate its relatively slow growth rate. This can be better understood from a consideration of Figure 93.

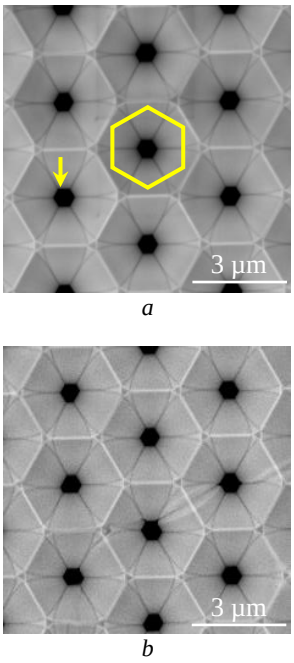

Figure 92: SEM (secondary electron) images of (a) Δ- and (b) Δ+-type samples after growth of ~2 µm AlGaN at 1060°C and 150 mbar in high V/III ratio[100]. The yellow hexagon in figure (a) shows the orientation of µ-hole base prior to growth. The arrow points to the part of a V-pit, which is referred in the main text as 'tunnel' region.[100]

For an arbitrary structure with pre-existing three facets: polar, semi-polar and non-polar, to preserve its shape i.e. points $A_{i>0}$ stay at the same x as the initial point A_0 and points $B_{j>0}$ stay at the same y as the initial point B_0, the growth rate ratios along these three directions should be in the following relationship with each other:

$$G_c \cos(\omega) = G_{sp} = G_{np} \sin(\omega), \qquad 4\text{-}1$$

where G_c, G_{sp} and G_{np} are the growth rates along *c*-, semi-polar and non-polar planes, respectively, and ω is the angle between the semi-polar and *c*-planes. In the case of the semi-polar plane growth rate G_{sp} being larger than both left and right sides of equation(4-1), its area will shrink (or will not appear if it did not pre-exist as in our case). This is not what is observed in our experiment (Figure 92), and therefore, the opposite relation should take place confirming our postulation of slow semi-polar plane growth rate made in the previous paragraph.

From the same considerations, it is also clear that coalescence can be achieved when points $A_{i>0}$ move to the right relative to the initial point A_0, i.e.,

$$G_{sp}/G_c > \cos(\omega) \qquad 4\text{-}2$$

From a cross-section SEM measurement (not shown), the angle of the semi-polar facets was found to be close to 60° with respect to the *c*-plane. This means that to achieve coalescence, we need to identify growth conditions at which the growth rate along the semi-polar facet is faster than approximately half of the growth rate along the *c*-plane.

On another note, from the angle between semi-polar facets and *c*-planes being ~60° we can speculate that their crystallographic orientations should be either from the {1101} or {1122} of planes (theoretical values of 62° and 58°, respectively[148]). From the comparison, for example, of Figure 42, *c* and Figure 92, *a*, it is clear that they are {1122} planes as the orientation of the hexagon rotates by 30° after growth (as was noted early, the original µ-HC holes had almost vertical i.e. nearly *m*-plane sidewalls).

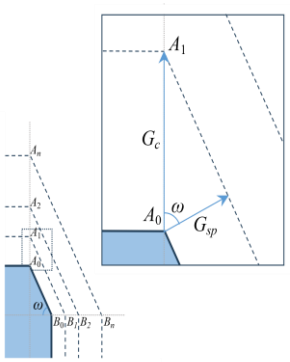

Figure 93. – Schematic of one possible surface evolution of a µ-HC sidewall where its initial top horizontal c-plane facet neither expands nor shrinks. Material of the µ-HC sidewall is represented in light blue colour[100].

Without going into detail, the rotation of hexagons after growth is defined by the ratio between growth rates along competing semi-polar facets. For growth inside apertures, the *dominant* planes are those that are faster growing. Based on considerations analogous to those we introduced while discussing Figure 93 and considering the competition between {1101} and {1122} facets, it is possible to show that the growth rate along $11\bar{2}2$ needs to be faster by approx. 1.155 (1/cos(30°)[*] for this twist to happen. So, while as it will be shown

[*] This rough estimation is based on the hexagonal geometry of the initial µ-holes. Here, we consider the ratio of the distance from the hexagon apexes to the µ-hole centre to the lateral component of growth rate along *a*-plane tilted facets {$11\bar{2}2$}. This time is then compared to the ratio of the distance from the middle of the hexagon side to the µ-hole centre to the lateral component of growth rate along *m*-plane tilted facets {$1\bar{1}01$}. For simplicity, we assume that both of these semi-polar

later this is not always the case, we have to conclude that in these growth conditions, this requirement is satisfied which is why this transformation takes place.

On the final note to these results, it is worth mentioning that some imperfections and irregularities are observed for the Δ+ sample (Figure 92, *b*) grown in the same run which suggests that disjointed patterns will require more time to develop uniform semi-polar regions, or will have a hard time to converge into a uniform regular structure.

Despite the promising results in terms of realising such novel faceted structures, AlGaN growth using the standard GaN conditions appears to be non-optimal because of the requirement to apply a high trimethyl-aluminium (TMAl) to trimethyl-gallium ratio in the gas phase to reach the aluminium content in the solid around 20% (our target). As a result of the significant pre-reaction of trimethyl-aluminium with ammonia[140], a heavy deposition of white particles (most probably AlN or high aluminium content AlGaN) on the quartz parts of the reactor was observed. Lowering growth pressure is one of the ways to reduce unwanted pre-reaction and utilize precursors more efficiently. From these considerations, the effect of the reduction of pressure was evaluated.

Effect of low pressure

While reducing pressure can suppress the unwanted pre-reaction of TMAl with ammonia[140], the reduced pre-reaction will increase the growth rate (with more aluminium incorporation) and thus the aluminium content of AlGaN. To bring it back to the original ~20%, the TMAl/TMGa ratio was reduced accordingly. Figure 94 shows the µ-HC sample grown at a reduced growth pressure of 75 mbar.

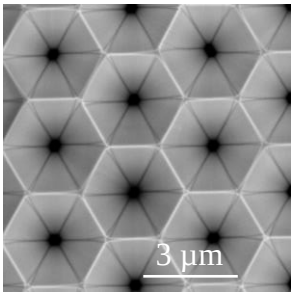

facet families are tilted by ~60° from the *c*-plane. It is considered that the plane that reaches the centre of the µ-hole earlier will become the dominant plane. A more precise analysis considering the individual (for each plane family) tilt angles gives a factor of 1.114 instead of the above-mentioned 1.155.

Comparing Figure 92, *a* and Figure 94 one can see that no significant impact of pressure reduction on the surface morphology takes place. Based on this finding and to prevent pre-reactions while achieving optimum utilization of precursors, we will treat 75 mbar growth pressure as default in our further experiments unless otherwise specified.

Figure 94: SEM (secondary electron) image of Δ-type sample after growth of ~2 µm AlGaN at 75 mbar in high V/III ratio condition.[100]

Effect of V/III ratio

Another way to reduce pre-reaction between TMAl and ammonia is through the reduction of ammonia partial pressure. For this reason, but also to find whether the reduced V/III ratio changes relative growth rates between the *c*-plane and semi-polar planes, this direction was chosen for further expanding of explored space of growth parameters (~3.3 times reduced ammonia flow: from 33% down to 10% of total flow). To account for the corresponding change in AlGaN composition, the TMAl/TMGa ratio was once again adjusted by modifying the TMAl flow, based on separately grown planar calibration samples, to maintain aluminium content around the target 20% which led to minor shifts in the effective V/III ratio in each case. The rough V/III ratio was originally ~700, and hence around ~230 for the reduced ammonia partial pressure growth.

The effect of the reduced V/III ratio on surface morphology can be seen in Figure 95 where top-view SEM images of Δ-, Δ+- and Y-type samples are presented. The following factors are noted. First of all, a lower V/III ratio also favours semi-polar facet formation resulting in hexagonal V-pits rotated by 30° with respect to the wet etched µ-holes as can be observed from Figure 95, *a*. Secondly, it appears that a lower V/III ratio makes it harder to preserve/recover the facet morphology of semi-polar facets. This can be seen from the curvature of the border/intersection of slanted facets with the *c*-plane (one of which is highlighted with a yellow curve in Figure 95, *a*). Their curved shape (rather than being a straight line) indicates a slight concavity in the horizontal direction of $\{11\bar{2}2\}$ planes.

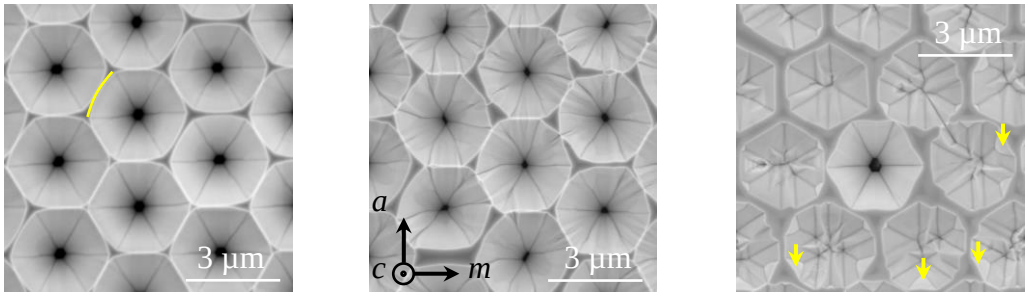

a b c

Figure 95 : SEM (secondary electron) images of a) Δ-type b) Δ+-type c) Y-type samples after growth of ~2 µm AlGaN at low V/III ratio of ~232 and 75 mbar. Yellow arrows in figure (c) point to some of the residuals of {11$\bar{2}$2} facets.[100]

Despite shrinkage of the *c*-plane, this process is apparently slower for regions located next to the intersections between adjacent {11$\bar{2}$2} planes. This may indicate slightly faster growth rate of semi-polar facets in these regions close to their mutual intersection compared to those in the middle, which exactly defines their above-mentioned concavity. A possible mechanism defining such a behaviour is that these intersections may act as origins of easier nucleation of steps in the horizontal (lateral) direction. Note, that acceptance solid angle for precursors to land in this corner regions is smaller compared to the centres of {11$\bar{2}$2} facets and so growth rate there should be slower without lateral adatom surface diffusion. While moderate surface diffusion in the case of high V/III ratio can only compensate for this effect so that no significant gradient is observed (Figure 94), the increased surface mobility at lower V/III ratio diminishes the difference in amount of adatoms obtained directly from the ambient while the easier nucleation of steps becomes more significant factor resulting in a locally increased growth rate.

With the reduced crystallographic quality of semi-polar facets of the Δ-type sample at low V/III ratio, our Δ+-type sample could not form sharp crystallographic {11$\bar{2}$2} facets (Figure 95, *b*), while it was possible at high pressure/high V/III ratio conditions (see Figure 92, *b*).

Further consequences of the enhanced diffusion length of group-III adatoms are: a) improved non-polar growth rate due to more (mostly gallium) adatoms reaching non-polar planes inside the tunnel from the slower growing semi-polar planes, and b) enhanced parasitic growth directly on sapphire substrate at the bottom of the µ-holes. The former has manifested itself in a smaller diameter of the tunnel for samples of all three types. The latter resulted in the Y-type sample V-pits being filled with material grown at the bottom.

In general, due to the high 'stickiness' of aluminium species, AlGaN growth starts everywhere: at *c*-plane, at non-polar planes and even on sapphire in the bottom of µ-holes (the parasitic growth mentioned above). As growth progresses, non-polar planes expand inward forming a vertical V-pit 'tunnel' region in the middle (with its upper part being the intersection between non-polar and semi-polar facets). As the V-pit tunnel shrinks, the solid angle at which the sapphire surface at the bottom of it 'sees' the ambient reduces. This leads to a decrease in the direct supply of precursors there due to a *shadowing* effect[149] suppressing further parasitic growth. However, if parasitically grown material reaches the upper part of the tunnel before it is sufficiently 'closed', then parasitic growth can take over, climbing up the semi-polar facets. For all samples at high V/III ratio, their V-pit tunnels shrink enough before this happens because the width-to-depth aspect ratio of the initial µ-holes was optimised for that, based on preliminary experiments not reported here. While for Δ/Δ+-type samples, parasitic growth is suppressed even at a low V/III ratio, most of the V-pit tunnels of the Y-type sample do not have time to close early enough. This is due to µ-holes of the Y-type sample being of higher than critical width-to-depth aspect ratio for these growth conditions. As seen from Figure 42, *b*-*d*, wet etched µ-holes of the Y-type sample are slightly larger laterally than those of Δ- and even Δ+-type samples while being of the same depth.

Normally, under these growth conditions, µ-holes should evolve into V-pits with *a*-plane-tilted semi-polar facets $\{11\bar{2}2\}$, as is observed for the Δ-type sample (Figure 95, *a*). However, the orientation of the semi-polar facets for most of the µ-holes of the Y-type sample is ultimately *m*-plane tilted (compared to Figure 42, *d*). The generally reduced crystallographic quality of their facets is due to the randomness of the undesired parasitic growth and in this regard can be ignored. Residuals of *a*-plane-tilted semi-polar facets are visible where parasitic growth did not have time to climb up all the way from the tunnel to the *c*-plane (marked with yellow arrows in (Figure 95, *c*). As an extreme example of that, one V-pit in the centre of Figure 95, *c* has no parasitic growth and so its semi-polar facets are oriented as expected for these growth conditions (*a*-tilted: $\{11\bar{2}2\}$).

It is interesting to speculate about the crystallographic orientation of the parasitic growth and why it differs from the one dictated by growth conditions. While it is clear from the general principle that the crystallographic orientation of V-pit facets

is defined by the relative growth rates of the concurring semi-polar orientations, further and more detailed analysis of this observation will be given later (in P. 139, subsection semi-polar facet formation).

Effect of growth temperature

Reactor temperature defines many critical parameters during growth starting from ammonia cracking efficiency, and continuing to adatom diffusion lengths, desorption/decomposition rate, chemical activity of precursors and unwanted impurities. As low V/III ratio conditions (NH_3 constitutes only 10% of total flow) in general, and Δ+-type sample in particular, showed degraded crystallographic quality of µ-HC structures a temperature series of samples was grown at high V/III ratio (NH_3 constitutes 33% of total flow) and only for Δ- and Y-type samples.

The surface morphology of Δ- and Y-type samples grown at different temperatures are presented in Figure 96. From this series, it is obvious that higher temperature favours coalescence, as for both Δ- and Y-type samples *c*-plane area significantly increased after ~2 µm AlGaN growth. As before, the shape of what was left of the µ-holes is hexagonal with an orientation of 30° rotated versus its original (before overgrowth) orientation. Among the two concurrently grown samples the Δ-type has a relatively larger *c*-plane region compared to Y-type because of the initial overall larger *c*-plane area to begin with.

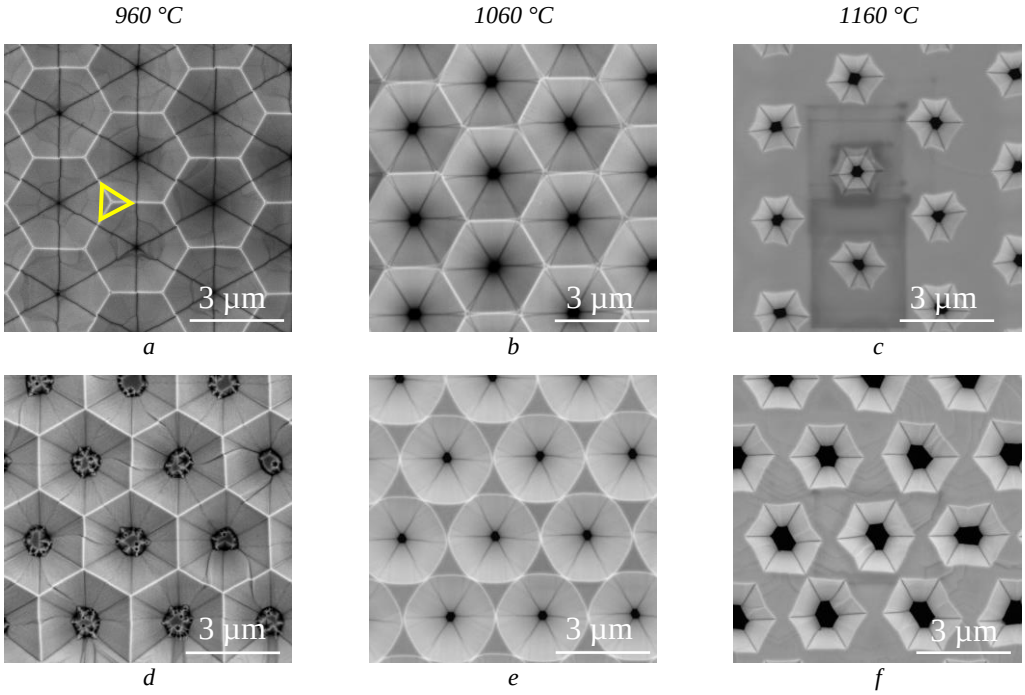

Figure 96: Top view SEM (secondary electron) images of Δ-(a-c) and Y-type (d-f) samples after growth of ~2 µm AlGaN at high V/III ratio, 75 mbar and growth temperatures of 960°C (a, d), 1060°C (b, e), and 1160°C (c, f). Yellow triangle in figure (a) highlights a pyramidal feature.[100]

Conversely, low-temperature growth of AlGaN results in absolute extinction of the *c*-plane even in the Δ-type sample which completely loses triangular *c*-plane regions having instead pyramidal regions where the *c*-plane use to be (marked with yellow triangle in Figure 96. *a*; compare to Figure 42, *b*). What is more remarkable, no rotation of the semi-polar facets happens at this low temperature i.e. *m*-tilted semi-polar facets (Figure 96. *a* and *d*) and not *a*-tilted are formed, so that unlike at higher temperatures Δ-type (before growth) µ-HC stays Δ-type in orientation, and similarly for the Y-type µ-HC. By tilting samples in SEM, it was possible to measure the angle of the *m*-tilted facets which was found to be ~60° from which we conclude their crystallographic orientation to be $\{1\bar{1}01\}$. This is a very common crystallographic orientation of 3D GaN nano/micro structures, although those of a convex shape e.g. nanocolumns[150], micro-fins[151], etc.[20]. As was speculated in P. 129 (section about AlGaN overgrowth using standard GaN conditions), which semi-polar plane forms in the apertures is defined by their relative growth rates. From preserving the original orientation of the µ-hole hexagonal shape we can conclude that the growth rate along $(11\bar{2}2)$ direction is not faster by at least ~15% ((1/cos(~30°) – 1)×100%) than that along $(1\bar{1}01)$ direction at this growth conditions. The mutual competition of these two planes will be further discussed in one of the next sections (P. 139).

While it is clear that high temperature favours coalescence, it is still interesting to understand how it will be affected by V/III ratio at this elevated temperature. For this reason, an attempt was made to prepare low V/III ratio samples, and their SEM pictures are shown below (Figure 97).

From the comparison of Figure 96, *c*, *f* and Figure 97, *a*, *b*, respectively, one can see that to target coalescence, both high temperature and a high V/III ratio are required. While the higher temperature seems to be able to 'cure' the low V/III ratio's effect of deteriorated crystallographicity (observed in Figure 95), it (high temperature) on its own cannot significantly increase the *c*-plane area compared to that before growth. Triangular regions of the Δ-type (before growth) sample convert into Y-type regions after growth, but the overall *c*-plane area does not seem to significantly increase. For the Y-type (before growth) sample, triangular regions formed after growth have a combined area seemingly larger than that of initial Y-regions. We believe this is the effect of geometry (*c*-plane expansion is easier while converting Y-

regions into triangles) but further expansion of these triangular regions is expected to be much slower.

One of the possible explanations why the *c*-plane is not expanding as fast as at a high V/III ratio lies in the increased group-III (mostly Ga) adatom surface diffusion, whereby adatoms diffuse from the semi-polar to *c*-plane, increasing the *c*-plane growth rate (G_c) and consequently reducing the semi-polar growth rate (G_{sp}). From consideration of the equation(4-2) inequality this means the G_{sp}/G_c ratio will decrease, making it harder to achieve the threshold value of 0.5 for coalescence. Further discussion on this point as it is impacted by growth temperature will be made later (in the section on possible mechanism of change in growth rate ratio, P. 146).

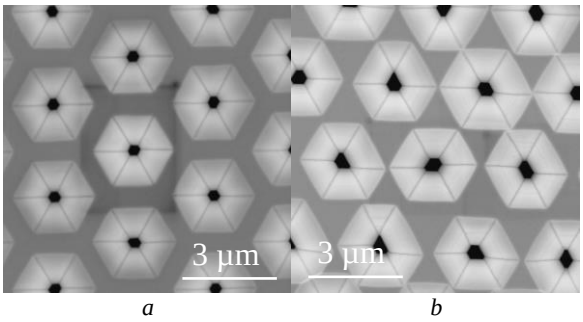

Figure 97: Top view SEM (secondary electron) images of (a) Δ-and (b) Y-type samples after growth of ~2 µm AlGaN at low V/III ratio, 75 mbar and growth temperatures of 1160°C.[100]

Effect of carrier gas.

Having identified the coalescence growth condition, with the view of further expansion of the explored area in the space of growth parameters, the effect of switching carrier gas from hydrogen to nitrogen was examined. It is known that nitrogen carrier gas promotes lateral growth on non-polar planes[150]; however, a pure nitrogen ambient in our experiments can lead to V-pit formation even in planar *c*-plane regions. It was found that adding ~15% of hydrogen to the nitrogen/ammonia ambient can completely suppress spontaneous V-pit formation. This mostly nitrogen-rich ambient was used to repeat our high temperature and high V/III ratio growth (Figure 98, *a*). Generally, similar *c*-plane expansion has been achieved in these N_2 rich conditions. The only

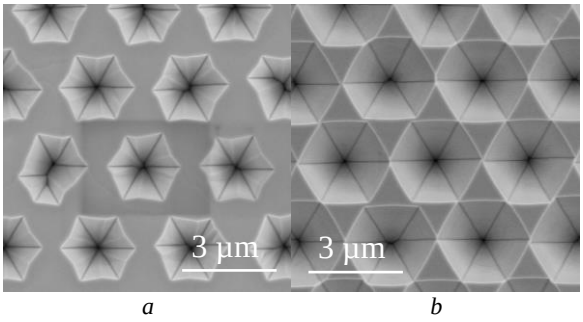

Figure 98: SEM (secondary electron) images of Y-type samples after growth of ~2 µm AlGaN in nitrogen rich ambient (only 15% of total flow composes H_2) at 1160°C & 75 mbar with (a) high and (b) low V/III ratios (ammonia constitutes ~33% and ~10% of total flow, respectively).[100]

noticeable difference was the almost complete closure of the tunnel, which can be explained by the above-mentioned improved non-polar growth rate.

Similarly, to the pure hydrogen conditions, the reduction of the V/III ratio significantly slows down *c*-plane expansion.

4.2.3.4 Discussion

After having explored the growth parameter space and identifying suitable conditions favouring the formation of V-pits with semi-polar {11$\bar{2}$2} facets and *c*-plane expansion (coalescence), to draw a comprehensive picture of overgrowth mechanisms, a systematic study of the surface morphology evolution at the corresponding growth conditions has been undertaken.

Semi-polar facet formation

From the above presented data, it is observed that at high enough temperatures initially 'nearly *m*'-plane-faceted (1$\bar{1}$00) µ-holes transform into {11$\bar{2}$2}-faceted V-pits (e.g., Figure 94, *a*). Furthermore, at sufficiently low temperatures this transformation does not occur (Figure 96. *a* and *d*).

On the other hand, a 'reverse' transformation to some form of *m*-plane-tilted semi-polar facets occurs when the V-pits get infilled with parasitic growth (Figure 95, *c*). This can be seen by the 30° rotation of the facet boundaries within these pits compared to the pit in the centre of the Figure where parasitic growth did not occur. To understand these behaviours, a series of samples were grown with different nominal thicknesses (0.25 – 4 µm) in conditions (1060 °C | high V/III | 75 mbar | H_2) favouring semi-polar facet formation, and the corresponding SEM images are presented in Figure 99.

In the first stages of growth, the *m*-plane-tilted semi-polar planes {1$\bar{1}$01} form which is defined by the initial geometry of the µ-holes. The semi-polar plane angle of ~60° was confirmed by tilted SEM analysis meaning this is the same family of planes that we observe at lower temperatures (e.g. Figure 96. *a*). Once these planes are fully developed, another semi-polar plane starts to form at the intersection between adjacent {1$\bar{1}$01} planes. It is interesting to note that the intersection of two adjacent semi-polar planes of {1$\bar{1}$01}-family is oriented relative to the *c*-plane at an angle exactly equal to that of [11$\bar{2}$2] relative to the *c*-plane. The formation of {11$\bar{2}$2} semi-polar planes is visible at 0.5 µm of nominal thickness. Further (at 1 µm of

nominal thickness), an even more complicated crystallographic configuration is observed: V-pits form a distinct dodecagonal shape for the Δ-type sample (Figure 99, *d*) and a less obvious but still recognisable octadecagonal shape for the Y-type sample (Figure 99, *j*). The twelve semi-polar facets in the Δ-type sample (Figure 99, *d*) are two families of semi-polar planes which, assuming the angle of these facets with *c*-plane stays ≈60° (not measured) can be indexed as {12$\bar{3}$3} and {1$\bar{3}$23} as they are azimuthally oriented just in between *a*- and *m*-directions. Their non-polar versions {12$\bar{3}$0} and {1$\bar{3}$20} according to GaN Wulff plot should be faster growing than even *a*-planes which 'sit' in local minima[152] while maxima correspond roughly to these two families of non-polar planes. These non-polar planes are predicted to be typical for growth of wurtzite materials in apertures[153], and have been reported previously for wurtzite InP nanostructures[154]. So, the appearance of expectedly fast-growing semi-polar versions of these planes in our μ-holes is not completely surprising. In the Y-type sample, in addition to these twelve, also six residual *a*-plane-tilted {11$\bar{2}$2} are present (Figure 99, *j*), which are located next to residual triangular regions.

In the absence of data between 1 and 2 μm, it is hard to speculate about how exactly the competition between {12$\bar{3}$3}+{1$\bar{3}$23} and {11$\bar{2}$2} takes place, but the outcome is clear, at least for the Δ-type sample: the {11$\bar{2}$2} family of planes becomes dominant by the nominal thickness of 2 μm and remains dominant after another 2 μm of AlGaN growth (Figure 99, *e, f*)). While both {12$\bar{3}$3}- and {1$\bar{3}$23}-facets are expected to be faster growing than {11$\bar{2}$2}[152], there is an argument in favour of a combination of these families of planes being less stable. There is an inherent asymmetry for these facets in terms of their mutual intersections: some of these intersections are tilted versus the *c*-axis towards *m*-planes (horizontal in Figure 99, *d* and those at ±60° to them) while others are tilted towards *a*-planes (vertical and those at ±60° to them, *ibid.*). As was discussed before, mutual intersections of semi-polar facets may act as origins of growth steps, so it is logical to assume that the step-generating efficiency of intersections along *a*- and *m*-directions is significantly different (higher for those oriented along *a*-axis as it is faster growing[152]). This should lead to a locally faster growth rate and gradual inclination of two neighbouring facets corresponding {11$\bar{2}$2} e.g. [32$\bar{1}$3] and [21$\bar{3}$3] towards [11$\bar{2}$2]. This is seemingly how {11$\bar{2}$2}-facets eventually reappear in Δ-type sample at nominal thicknesses of overgrowth over 1 μm.

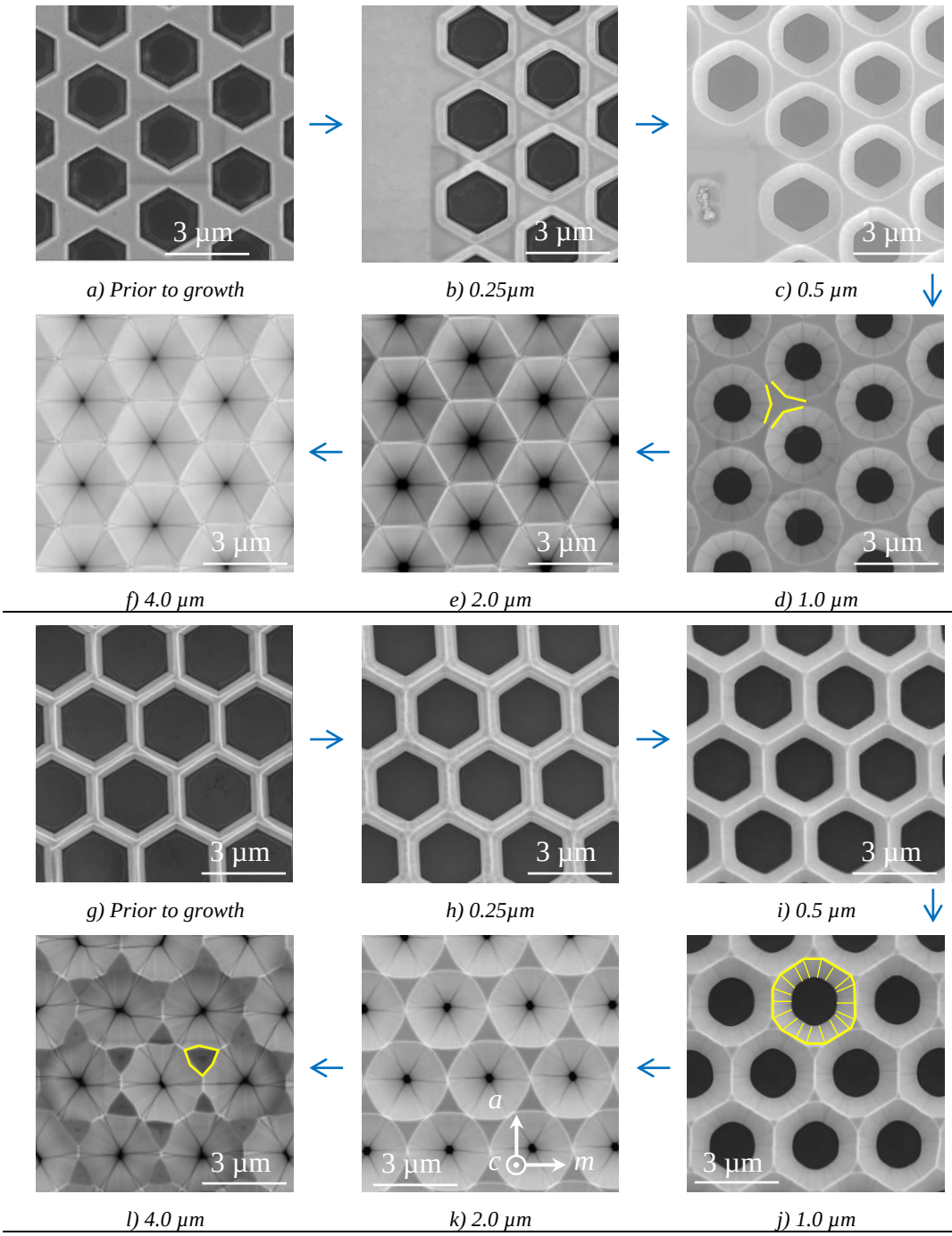

Figure 99: Surface morphology evolution of Δ- and Y-type µ-HC structures grown in conditions favouring semi-polar facet formation. [100]
(all images acquired using secondary electron detector.)

Despite a moderate temperature of 1060°C favouring *c*-plane shrinkage for our Δ-type µ-HC sample, the Y-type (before growth) sample (Figure 99, *g*) seems to be able to develop triangular *c*-plane regions as growth progresses, whose area increases in the process of conversion of the V-pit facets from *m*-plane-tilted ($\{1\bar{1}01\}$) as in Figure 99, *i* , to *a*-plane-tilted ({1122}) ones, as in Figure 99, *k*. In general, this

seems to be defined by the geometry of the array (after the growth, the initial Y-type HC sample effectively converted to a Δ-type one). The growth rate ratio between *a*-plane-tilted ({1122}) facets and the *c*-plane in this 1060°C case seems to be not much lower than 0.5 (cos(≈60°), see equation(4-2) which allows observed flat triangular *c*-planes to form (Figure 99, *k*) as opposed to the pyramidal regions that occur in the Δ-type sample at low temperature (Figure 96, *a*).

The 'final' shape of these 'triangular' *c*-plane regions (one of which is highlighted in Figure 99, *l*) suggests that facets of the V-pits after 4 µm of nominal growth are not exactly *a*-plane tilted ($\{11\bar{2}2\}$) ones, but instead, each of the six fundamental a-tilted facets is split into two sub-facets with slightly different crystallographic orientations. We can speculate that these belong to $\{12\bar{3}3\}$ and $\{1\bar{3}23\}$ families of planes already mentioned above (in the discussion concerning Figure 99, *d*). However, in this case, these sub-facets intersect with each other making the fundamental V-pit facets convex-shaped (as can be seen from the comparison of highlighted shapes in Figure 99, *l* and Figure 99, *d*). It is hard to assertively conclude why the dominant crystal planes are different in Δ- and Y-type samples. One possibility is that it has something to do with the presence and absence of *c*-plane regions in the 'final' topologies, which is defined by the orientation of the µ-HC array.

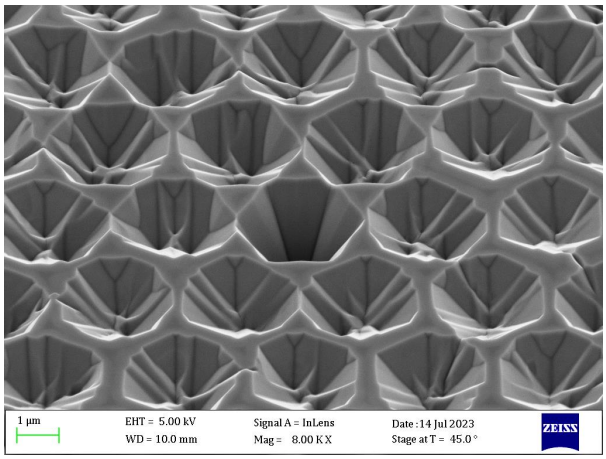

Figure 100: Tilted view SEM (secondary electron) of the sample shown in Figure 95, c.[100]

The final topology of the Δ-type sample (Figure 95, *a*) is still an indication that growth along $(11\bar{2}2)$-direction (*a*-plane-tilted) is more than 15% faster compared to that along $(1\bar{1}01)$-direction (*m*-plane-tilted). However, this appears to contradict the 'reverse' transformation back to a form of *m*-plane-tilted facets when parasitic growth fills the V-pits (Figure 95, *c*). To consider this further, a 45°-tilted view of the relevant sample (Figure 100) was examined. In the figure, a rare V-pit that did not get infilled is shown in the centre. One can see that while the bottoms of all infilled V-pits are visible, that of the one in the centre is not (as is expected given the depth of an $\{11\bar{2}2\}$-faceted V-pit). From

this, it is clear that the angle of the 'new *m*-plane tilted facets' to the *c*-plane is significantly smaller than that of {11$\bar{2}$2}. As the base of all the infilled (with parasitic growth) V-pits is still visible, we conclude that the angle of the infill *m*-plane-tilted facets to the *c*-plane is close to or less than 45° (our SEM tilt angle). Hence these infill *m*-plane-tilted facets cannot be {1$\bar{1}$01} that were observed at lower growth temperatures when there is no *m*-plane-tilted to *a*-plane-tilted facet transformation. We believe that these new dominant planes are *r*-plane ({1$\bar{1}$02}) in nature, whose angle with the *c*-plane is ~43°. While the competition (in terms of growth rate) between {11$\bar{2}$2} and {1$\bar{1}$01} at these high-temperature growth conditions is won by the former, that is not the case when the *r*-family of planes {1$\bar{1}$02} comes into play, which the parasitic growth allows. V-pits get infilled when this occurs because the growth rate of the *r*-planes is faster than that of {11$\bar{2}$2} and probably even {12$\bar{3}$3}/{1$\bar{3}$23}. Considering the exact geometry and applying a similar approach to that used to calculate the threshold growth rate ratio (equation (2)) based on schematic information in Figure 93, it is possible to show that the precise ratio between these two semi-polar plane growth rates should be at least approximately 1.391 for the observed taking over to happen (i.e. $G_{\{1\bar{1}02\}} > 1.391 \cdot G_{\{11\bar{2}2\}}$).

The reason why *r*-planes, despite being seemingly the fastest growing semi-polar planes considered so far, do not dominate the surface morphology of V-pits when there is no parasitic growth is an interesting question. However, a discussion of the matter requires further investigation which is beyond the scope of this thesis.

Coalescence conditions

The morphological development of the surface under conditions favouring coalescence is shown in Figure 101. As discussed earlier for semi-polar facet conditions, initially *m*-plane tilted facets ({1$\bar{1}$01}) form. However, the formation of *a*-plane tilted facets ({11$\bar{2}$2}) starts earlier, being observable after already 0.25 µm of nominal growth, and by 0.5 µm they are dominant (Figure 101, *c*, *i*). This indicates that the competition between these two semi-polar families of planes is very much in favour of {11$\bar{2}$2} one.

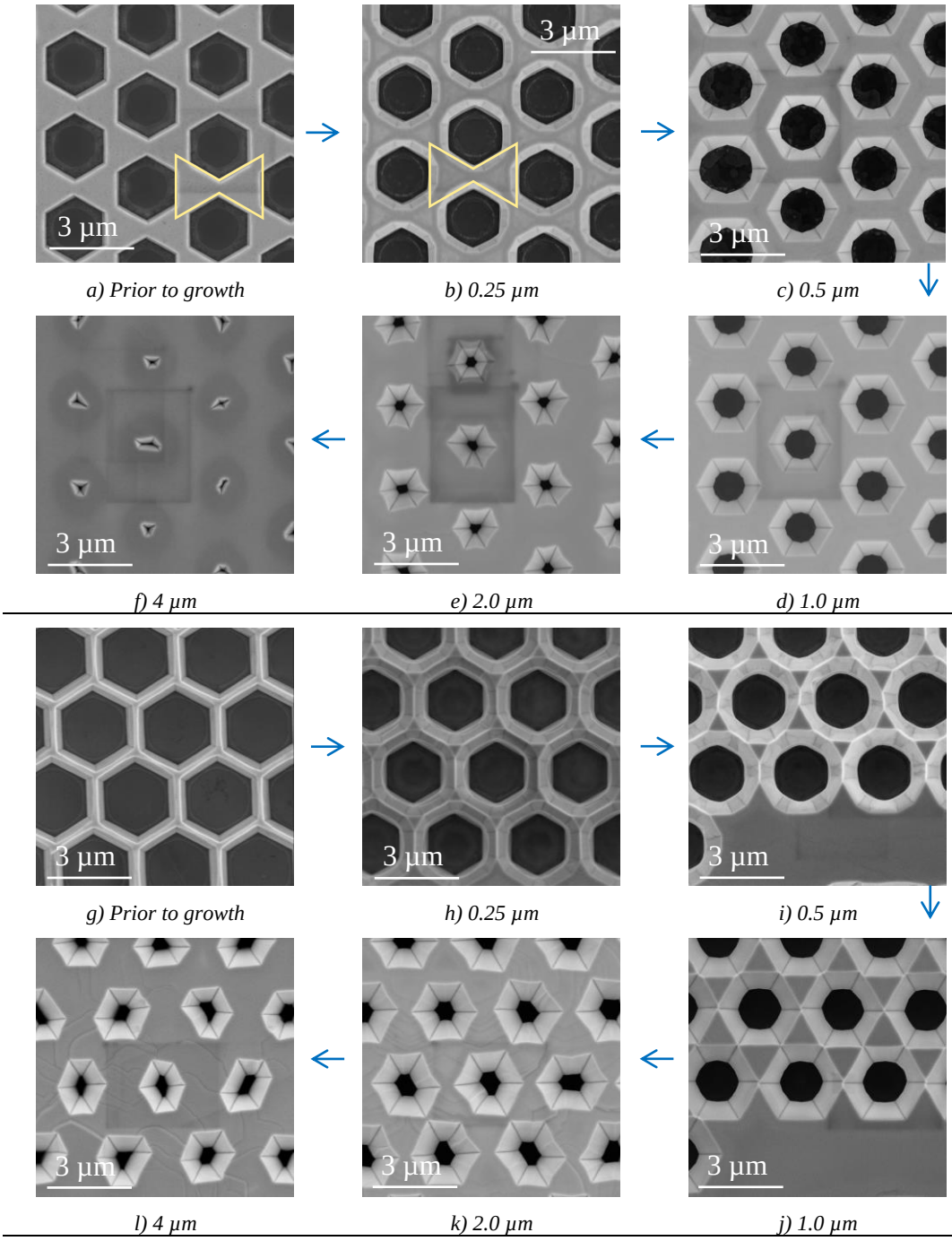

Figure 101: Surface morphology evolution of Δ- (a-f) and Y-type (g-l) µ-HC structures grown in condition favouring c-plane expansion.[100]
(all images acquired using secondary electron detector.)

While in general high-temperature and high V/III ratio conditions favour *c*-plane expansion, things are not as trivial as they may seem at first glance. Although narrow, *c*-plane regions in our Y-type sample are present and continuous before growth (Figure 101, *h*), after 0.25 µm of nominal growth the continuity in the *c*-plane regions disappear, and very small (and thus isolated) triangular regions form instead.

Similarly, the rather large triangular regions of the Δ-type sample initially shrink, while *c*-plane regions between them expand.

As was mentioned above, in a competition between a *c*-plane and a semi-polar plane tilted at an angle ω, for a stable topology (no *c*-plane expansion or shrinkage), the corresponding growth rates should satisfy the left part of the equation(4-1). Since soon after the start of overgrowth, two types of semi-polar planes ($\{1\bar{1}01\}$, $\{11\bar{2}2\}$) coexist, the above condition applies to both families of planes separately. From what we observe (the *c*-plane shrinks opposite to *m*-plane-tilted $\{1\bar{1}01\}$ facets, while it expands opposite to *a*-plane-tilted $\{11\bar{2}2\}$ ones), for both semi-polar planes the stability equation is not satisfied, but in different ways. For *m*-plane tilted facets $G_{0001}\cdot\cos(\omega_{\{1\bar{1}01\}}) > G_{\{1\bar{1}01\}}$ (i.e. $G_{\{1\bar{1}01\}}/G_{0001} < \cos(\omega_{\{1\bar{1}01\}})$ in contrast to expression (4-2) meaning coalescence is not favourable) and $G_{0001}\cdot\cos(\omega_{\{11\bar{2}2\}}) < G_{\{11\bar{2}2\}}$ (i.e. $G_{\{11\bar{2}2\}}/G_{0001} > \cos(\omega_{\{11\bar{2}2\}})$ in accordance with expression (4-2) and coalescence can be favoured). From the above, it is also clear that $G_{\{1\bar{1}01\}} < G_{\{11\bar{2}2\}}$, which is in line with our overall description of the growth behaviour.

Furthermore, the fast growth rate along $(11\bar{2}2)$ eventually (after 2 μm of nominal growth) results in the splitting of the *a*-tilted semi-polar facet into two individual nearly-$\{11\bar{2}2\}$ semi-polar sub-facets (Figure 101, *e*, *k*), which were observed already in (Figure 99, *l*) and were identified as $\{12\bar{3}3\}$ and $\{1\bar{3}23\}$. One of the possible mechanisms for that is due to the acceptance angle (the solid angle at which the surface receives precursors from the ambient) in the central part of an *a*-tilted semi-polar plane is greater than in the regions close to the intersections of two adjacent facets while adatom surface diffusion cannot compensate for that. This process is also favoured by probably faster growth rate of these intermediate (oriented azimuthally between *a*- and *m*-directions) semi-polar planes compared to purely *a*-tilted $\{11\bar{2}2\}$. Eventually this results in a change of the intersection of the V-pit with the *c*-plane surface from purely hexagonal to slightly star-like shaped.

A similar evolutional behaviour was observed during the study of surface topology as a function of thickness variation in $H_2 + N_2$ ambient (not shown). Coalescence, in this case, occurs earlier (e.g., at 4 μm of nominal growth, a full planarization of Δ-type sample has been achieved) because of, we believe, stronger lateral growth (along non-polar directions) and earlier closure of the tunnel as discussed in P. 138 (section on the effect of carrier gas). However, in terms of

precursor spending, there was no advantage due to higher pre-reactions and reduced growth rate compared to pure hydrogen ambient condition.

Possible mechanism of change in growth rate ratio

From the above discussions, it is clear that the particular evolution of surface morphology is defined by the relative growth rates of the involved crystallographic orientations and the initial geometry of the µ-patterned structures. A key question is what causes these growth rates to change relatively as a function of growth conditions. For example, increase in temperature seemingly enhances growth of $\{11\bar{2}2\}$ semi-polar family of planes: at low temperatures ($\leq$ 950°C) it is so slow that no transformation (rotation) of V-pit occurs; at intermediate temperatures (~1060°C), the hexagonal shape of V-pit rotates by 30°, and finally, at high enough temperatures ($\geq$ 1160°C), not only rotation but also coalescence takes place.

The $\{11\bar{2}2\}$ family of planes is known to be faster growing in GaN compared to $\{1\bar{1}01\}$ at moderate temperatures[152]. For example, Hartmann *et al.*[151] manages to grow vertical microfin structures (with only horizontal *c*- and vertical *a*-plane facets) through line apertures oriented along the *m*-axis while their attempt to do the same for line apertures oriented along *a*-axis ended up in structures with pyramidal slanted facets $\{1\bar{1}01\}$ which they explain by exactly slower growth rate along $(1\bar{1}01)$. Feenstra *et al.*[155] suggested hydrogen termination of $\{1\bar{1}01\}$ crystallographic orientation as the mechanism explaining the formation of these semi-polar facets in a wide range of growth parameters. Furthermore, Akiyama *et al.*[156] studied the H-termination of various III-nitride crystallographic orientations and their results show that it is possible for $\{11\bar{2}2\}$-planes too.

Our understanding lies in line with the above considerations: in typical MOCVD conditions, III-nitride surfaces (including *c*-plane[157]) get terminated with atomic hydrogen, which prevents group-III adatoms from incorporating into the lattice. With adatoms arriving from the ambient while their incorporation is suppressed, they will accumulate on the surface increasing the adlayer thickness until their chemical potential exceeds that of hydrogen, and so the probability of adatom incorporation to the lattice increases. However, this occurs at different adlayer thicknesses for different crystallographic orientations. Thus, on complicated surfaces like our µ-HC, changes in group-III adlayer thickness occur for different facets. As a

result, some facets (with thinner adlayer thickness) act as sinks of adatoms while others will effectively 'feed' them with precursors that originally arrived to them.

From our data, it is clear that over a wide range of growth conditions semi-polar facets act as a source of group-III adatoms while the *c*-plane acts as a sink, leading to a low G_{sp}/G_c ratio, apparently below 0.5 (causing *c*-plane regions to shrink and disappear). The hydrogen chemical potential is known to decrease with temperature[158], which reduces the above-mentioned adlayer thickness differences between facets, and this then appears to reduce the 'feeding' of the *c*-plane with group-III adatoms (that initially landed on the semi-polar facets). This has the effect of increasing the G_{sp}/G_c ratio to about 0.5 so that the *c*-plane neither expands too much nor shrinks (e.g. Figure 97). Increased ammonia flow reduces adatom surface diffusion length, which on top of the reduced adlayer thickness differences between different facets (due to high temperature) suppresses the *c*-plane 'feeding' even further, resulting in a further increase in the G_{sp}/G_c ratio, to above 0.5 and hence allows *c*-plane expansion (Figure 101).

It looks like the G_{sp}/G_c ratio increase discussed above occurs faster for the $\{11\bar{2}2\}$-planes leading to an initially faster growth rate compared to $\{1\bar{1}01\}$ which leads to the 30° rotation of hexagonal V-pits and then to $\{11\bar{2}2\}$-planes growth rate high enough to satisfy the coalescence condition ($G_{\{11\bar{2}2\}}/G_{[0001]} > \cos(\omega_{\{11\bar{2}2\}})$). The reason for the apparently stronger temperature dependence of H-termination of $\{11\bar{2}2\}$ compared to $\{1\bar{1}01\}$ is beyond the scope of the current study; however, in favour of this view, two works of Hirmatsu *et al*. can be cited. They suggest that while the increase of temperature leads to improved GaN growth rate along $(11\bar{2}2)$ direction[67], the same does not occur for the growth rate along $(1\bar{1}01)$[159].

With this understanding in mind, it is now possible to speculate about another region in the growth parameters space leading to coalescence described in 4.2.1.3 (low temperature and extremely low V/III ratio). First of all, low temperature reduces the pyrolysis of ammonia, reducing the presence of atomic hydrogen. For this reason, despite of low temperature hydrogen passivation of different crystallographic orientations might be partly inhibited. Secondly, nitrogen adatoms on the surface are expected to be in deficiency effectively reducing the growth rate of all crystallographic orientations. Finally, in these conditions, group-III atoms adlayer thicknesses are expected to be increased also for all crystallographic orientations so that expectedly

large diffusion lengths do not cause significant adatom transfer between them. So basically, the growth rate along all crystallographic orientations is suppressed in such a way that the difference between semi-polar planes (which, by the way, in this particular case are probably $\{1\bar{1}01\}$ rather than $\{11\bar{2}2\}$) and *c*-plane is apparently less than 2, which leads to *c*-plane expansion and coalescence as a result.

Nevertheless, these conditions with some modifications and optimization might be usable for the coalescence of Al-rich AlGaN or AlN μ-HC but are not favourable for Ga-rich AlGaN but further work is required to find the optimum conditions.

4.2.3.5 *Material Characterization*

Besides the topological evolution of overgrown µ-HC structures, it is important also to check the improvement in crystalline quality to conclude whether or not this approach is promising for the fabrication of good quality AlGaN templates.

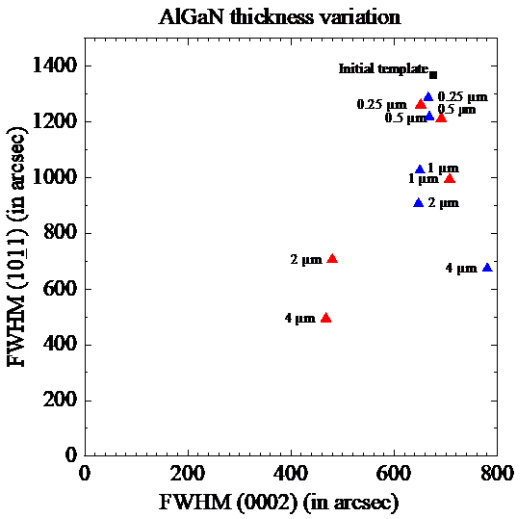

Figure 102: X-ray diffraction (red Δ-symbols show quality of sample with increasing AlGaN thickness grown at 1060°C, whereas blue Δ-symbols represents quality of samples with increasing AlGaN thickness of at 1160°C)

The material quality was assessed using X-ray diffraction as described in section 2.1.3.2 and was found to be directly related to the thickness of the overgrown AlGaN layer. Figure 102 shows reduction in the FWHM 101 reflection as a function of AlGaN layer thickness grown on Δ-type sample forming V-pit semi-polar facets, as shown in Figure 99, *a-f*. This trend is attributed to the reduction in *a*-type dislocations, which can be further confirmed from the optical quality comparison of the 4 µm sample with a planar reference sample shown in Figure 103. The possible mechanism of this improvement is due to the bending of dislocations reaching the surface at the slanted facets towards the tunnel region where they merge and/or annihilate.

Similar trend is also observed for samples grown in coalescence conditions shown in Figure 101, *a-f* as the µ-faceted templates i.e reduction in the FWHM of 101 reflection with nominal layer thickness shown in Figure 102. However, the FWHM of 002 reflection for the planarized template shown in Figure 101, *f* tend to increase which is opposite to µ-faceted one. While it is possible that the coalescence of surface features leads to partial conversion of edge-type dislocations to screw-type ones, there is an alternative explanation for the observed behaviour. Semi-polar facets are expected to incorporate more gallium (more details below) leading to larger in-plane and out-of-plane lattice parameters in the regions near the coalescence point. To partially accommodate this local strain, *c*-planes have to bend upward creating thus periodic undulations which in fact are local non-parallelities appearing in XRD as broadened FWHM, the effect similar to screw dislocations. A thorough TEM study

would be required to confirm this mechanism and quantify the effect, which, however, is out of the scope of this work.

On the other hand, these samples (that underwent *c*-plane expansion growth conditions and coalesced) were found optically as poor as reference samples shown in Figure 103*. While further study is required to understand this behaviour, a possible mechanism might be described as follows. Crystallographic orientations such as semi-polar facets incorporate more gallium[69,72,73] compared to *c*-plane regions. Therefore, a gradient of aluminium composition is expected in our structures immediately upon coalescence. The presence of a compositional gradient (results in a potential gradient) in regions above V-pits and the residual dislocations can act as localization centres for photo-excited carriers. Effectively, the photo-excited carriers recombine in these centres (at the dislocations) non-radiatively so that overall IQE stays low despite provisionally lower dislocation density compared to reference planar samples.

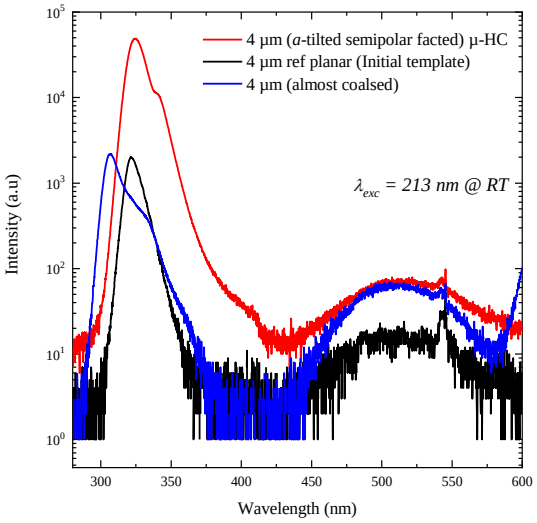

Figure 103: Photoluminescence of Δ- type µ-HC structures grown in conditions favouring semi-polar facet formation (in red) and coalescence condition (in blue).

4.2.4 Conclusions

In conclusion, a fabrication technique of AlGaN layers into patterns in the form of µ-HC structures (both Y- and Δ-type) has been developed. At this, an understanding of the main HC parameters (depth and diameter of µ-holes, array pitch) leading to suppression of *parasitic* growth has been obtained. It has been found that

* The red shift of the PL spectra of the coalsed sample compared to the semipolar faceted sample is due to the higher Aluminum content in the *c*-plane regions compared to the semipolar regions. In addition to that, the presence of a low energy shoulder in the PL spectra of almost coalsed sample (Figure 101, *f*) is due to the presence of small semipolar facets visible through the discontinuous (almost) coalsed surface. This can also be inferred by comparing the PL peak position of the semipolar faceted sample with the peak position of the low energy shoulder in the almost coalsed sample.

to avoid *parasitic* growth in the majority of growth conditions, the depth-to-diameter ratio of µ-holes should be equal to or more than 1.

As a result of the exploration of the space of growth parameters, the conditions required for both coalescence and semi-polar facet formation have been identified. The key parameter for coalescence has been found to be the ratio between growth rates along the *c*-plane and semi-polar planes. Taking into account the crystallographic orientation of semi-polar planes ($\{11\bar{2}2\}$ and sometimes $\{1\bar{1}01\}$) and their inclination with respect to the *c*-plane by about 60°, this ratio has to be less than approx. 2 (1/cos 60°) to coalesce a µ-HC structure back into a planar layer.

Since at *normal* growth conditions, semi-polar facets get passivated with atomic hydrogen, it appears that coalescence can be achieved in two rather extreme cases. At low temperatures and low V/III ratio (I), this passivation is weak due to both low ammonia flow and its cracking efficiency (low availability of atomic hydrogen) and is overcome by thick group-III adlayers due to deficiency of nitrogen. At high temperatures and high V/III ratio (II), H-passivation weakens reducing the difference in group-III adlayers thicknesses between *c*- and semi-polar planes while high V/III ratio reduces adatom diffusion lengths. As a result, at both these regions of space of growth parameters, the ratio between *c*- and semi-polar planes falls below 2 leading to *c*-plane expansion and coalescence.

All these experiments provided us with a sound understanding of the topological evolution of a µ-HC structure subjected to overgrowth. The secondary purpose of studying this was to achieve quality improvement of a coalesced layer which was not obtained. However, the material quality improvement observed during the topological evolution of semi-polar facets suggests that quality improvement might be possible if a strategy combining both these conditions is developed. In this strategy, initially, semi-polar facets are to be grown for long enough to bend out the majority of pre-existing dislocations. Then growth conditions are to be switched to ones favouring *c*-plane expansion, leading to coalescence of formed V-pits with hopefully improved quality of the material.

As a future work, these conditions are suggested to be explored further to achieve both improved quality standard planar and novel-type (with QWs along semi-polar facets) UV LEDs. On the semi-polar µ-facet-based LEDs front, future work may require optimization of *p*-GaN or ideally *p*-AlGaN as an increased unintentional

incorporation of various impurities makes us believe achieving hole conductivity is non-trivial.

4.3 Conclusion of template development

In summary, the background and understanding required to develop a template for a UV LED were attempted in this work by both planar and patterned approaches. Both the approaches provided insightful information and are required from cost and quality standpoints.

Planar approaches such as the AlN connection layer and grading the Al content in the buffer AlGaN region led us to crack-free, transparent, thick, conductive *n*-AlGaN buffer templates on which fully functioning (yet underperforming compared to the state-of-the-art) UVLEDs have been realized. The patterned approach studied in this chapter provided us with a critical understanding of the topological evolution of a µ-patterned surface which can either lead to a V-pit semi-polar surface or into a new coalesced layer. These results have the potential for further utilization in various aspects to improve the quality of the templates or realize novel devices.

Conclusion and outlook

Since the vision of our group is to improve the efficiency of a UV-LED, in this quest, this thesis contributes towards understanding two important issues, that directly impact the efficiency of UVA-LEDs. The two issues addressed in this dissertation were: a) apparent contradiction between routine use of thin (~30 nm) AlGaN as electron blocking layers in III-nitride based LEDs and reported its alleged inefficiency in UPHSes; b) lack of cheap and lattice-matched substrates for low/mid-Al content AlGaN and its poor crystalline quality when grown on cheap lattice-mismatched substrates.

Barrier properties of AlGaN in an *n*-GaN/AlGaN/*n*-GaN UPHS

To address the first issue, simulation and experimental works in the context of vertical electron transport through an intrinsic AlGaN barrier layer sandwiched between an *n*-doped GaN layer (also referred to as unipolar heterostucture denoted by UPHS) were conducted. In the simulation section, three different compositional descriptions of barrier regions of UPHS were used to study vertical carrier transport. All three developed models managed to qualitatively correctly describe the modelled structure producing intuitively understandable behaviour: increased knee voltage with barrier height and thickness. Although models including the averaging procedure (whose main function was the conversion of digital/discrete alloy into more physical/continuous one) showed reduced knee voltages compared to the reference VCA model, the non-rectifying behaviour reported in the literature could not be reproduced.

On the experimental front, it was possible to observe behaviours both similar to the ones predicted by our simulation (rectifiying JV) and the ones which had previously been observed in the literature (non-ohmic/non-rectifiying JV). Possible mechanisms behind the actual behaviour of the AlGaN barrier were proposed. In summary, they can be expressed as follows: Experimentally, UPHSes can show three different behaviours (ohmic, non-ohmic/non-rectifying, rectifying) depending on the AlGaN layer parameters (compositional contrast and thickness) for either too thin ($\lesssim$ 5 nm) or low Al-content ($\lesssim$ 10%), ohmic behaviour was systematically observed. For thick and/or high barriers ($\gtrsim$ 20 nm and $\gtrsim$ 15%, respectively), distinctly rectifying

behaviour was observed. The region in between these two ranges corresponds to non-ohmic/non-rectifying behaviour.

However, certain effects were found to influence this generic trend. Particularly, the formation of nano-fissures in the AlGaN layer (occurring during for example growth pause introduced to ramp conditions from the conductive layer of a UPHS to its barrier layer and back) was shown to ruin its effectiveness as a barrier layer even if AlGaN is in the "rectifying" region parameter-wise. This is most probably the main reason why previous studies failed to observe the rectifying effect experimentally as growth interruptions are not unusual at the growth of structures requiring different growth conditions for different layers.

In short, the strong sides of my contribution to this topic are:

I) the development of a framework that allows modelling UPHSes considering VCA and, if necessary, compositional landscape in their barrier region;
II) experimental demonstration of rectifying behaviour of UPHSes that qualitatively is correctly described by the above model;
III) determination of the parameter space for barrier regions defining their electrical properties;
IV) identification of other factors that can affect deviation from the predicted behaviour.

Nevertheless, there were some drawbacks of my work and issues that I could not adequately address within it: a) the averaging parameter σ used in my simulation was not chosen based on detailed physical consideration or first-principle calculations but was rather an empirical parameter that allowed to convert discrete alloys into continuous ones with feasible amplitude of fluctuations of alloy compositions; b) potentially related to the above issue discrepancy between my simulation and experimental results (even RA/SMI models overestimate knee voltages compared to experimental ones); c) my model failed to predict the mostly symmetric JV-characteristics experimentally observed.

To address the above-mentioned issues, further work in terms of simulating maps of larger lateral dimensions, using a 3D description of alloy fluctuations and including complex effects/models such as tunnelling, localization landscape, etc. may

be necessary. Nevertheless, despite the mentioned drawbacks, my findings already provided a basic understanding of vertical carrier transport in unipolar heterostructures and reported critical parameters which drive their electrical behaviour. My results can help to make an informed decision in the design and growth of structures containing thin AlGaN layers, particularly electron-blocking layers in visible and UV LEDs.

Heteroepitaxy of AlGaN as an LED buffer layer

The second broad topic of my thesis was related to the experimental optimization of hetero-epitaxially grown AlGaN buffer layers, aiming for low dislocation density, high conductivity, UV transparency, smooth surface morphology and continuity (crack-free), for UV LEDs. This matter was initially addressed by various planar techniques: a) replacing bare sapphire with Kyma template (~25 nm AlN/sapphire); b) insertion of an AlN connection layer before the growth of the AlGaN buffer layer; c) LT-AlN interlayers; d) and compositional grading of AlGaN buffer layer. They provided only a limited usefulness in obtaining high-quality AlGaN buffers. In particular, the combined effect of using an AlN connecting layer and graded aluminium content within the buffer allowed to obtain smooth surface morphology of *n*-AlGaN, dislocation density reduction down to 3-4·10^9 cm^{-2} and total thickness of ~2 µm before it cracks. Although these were successfully used for the epitaxial growth of UV LEDs, the overall performance of the prepared devices was found to be far behind the state-of-the-art in the field.

The above results as well as insights from the literature suggested that planar techniques are limited in scope i.e. cannot reduce dislocation density below ~2·10^9 cm^{-2}. Thus, as a mitigation strategy, efforts were directed at pattern-regrowth approaches where a decent fraction of the original (moderate quality) material is etched away and returned as newly grown (ideally improved quality) material. The initial goal here was to demonstrate AlGaN epilayers with substantially improved crystalline quality.

To achieve the above goal, firstly, quite a broad area of growth parameter space had to be studied to identify growth conditions suitable for recovery of planar topology. Secondly, growth mechanisms driving particular surface topology evolution had to be understood. From this point of view, patterns consisting of equally spaced and triangularly arranged µ-holes were chosen. This specific design was opted for

because of its merit of the rich composition of both concave and convex surfaces and a plurality of different crystallographic orientations appearing during overgrowth us allowing to study their mutual competition.

The main achievements on this front can be formulated as follows:

I) an optimized technique of patterning of AlGaN into µ-HC structures of Δ- and Y-type preventing parasitic growth and allowing a high fraction of original material to be removed has been developed;
II) growth conditions allowing both planarization and texturization (in the form of V-pits with semipolar facets of desired crystallographic orientation) of patterned µ-HC structures have been identified;
III) growth mechanisms behind particular surface topology evolution qualitatively describing the whole plurality of experimental data have been proposed;
IV) crystalline quality improvement of µ-faceted templates which manifested itself in both XRD and PL has been demonstrated.

On the downside, despite of achievement of planarized AlGaN layers, so far it was not possible to confirm their improved quality. Both XRD and PL suggest that it is below expectations. Although I proposed possible explanations for why the quality does not improve, further work is required to fully understand the experimental data. A detailed TEM analysis would be very helpful in this but due to limited resources, this was not possible within my research work.

In summary, my findings and the growth mechanism discovered can help an epitaxial grower predict and control the surface topology during AlGaN growth on a µ-patterned surface of arbitrary geometry. The overall technique I developed here is promising in achieving planar AlGaN templates of improved quality and µ-faceted AlGaN templates for planar UV LEDs with enhanced performance and novel-design LEDs with textured topology and non-planar active region, respectively.

Future work

This thesis bridges knowledge gap in our understanding of two crucial layers (EBL and buffer/templates) which play critical role in the functioning of a UVA LED.

In future using these results as a foundation, more targeted research in this area can be accomplished by means of further extending the horizon of the problem or expanding into various avenues depending on whether the end goal is application-centric exploration of technology or scientific exploration. Now that the barrier effect to vertical electron transport is observed for a thin AlGaN layer, it makes more sense to study its technological applicability for electron devices such as high power unipolar devices, bipolar junction transistors or for applications which require symmetric (in the first and third quadrant) rectifying behaviour, or for some other application such as fast-switching, charge storage, etc. Additionally, in the scientific context, research can be pursued in the experimental direction on the open question of "why the device characteristics are symmetric with respect to origin? i.e. in the first and third quadrants". This behaviour is against our fundamental understanding of III-nitride material as the presence of a polarization field along the c-axis direction should introduce an asymmetry in the device response which is not observed in this work.

Furthermore, if the intent of scientific discourse is theoretical in nature, then the simulational framework developed within this work can be pursued to study the effect of anisotropy in the shape of Gaussian averaging and how it affects the carrier transport at large. This is important because the uniform Gaussian averaging which is normally used to generate compositional fluctuating landscape does not capture the effect of ordering which has been observed in III-nitride alloys. Besides that, it would be interesting to understand the interplay of compositional gradient along with doping, by conducting a comparative study of carrier (specifically hole) transport through a graded and uniform alloy fluctuating landscape with or without doping for the same average content of group-III atoms in both the descriptions. This might help us further understand the effects of polarization-based doping used in high aluminium-containing UV LEDs/LDs. Possibilities also exist to use the current framework (upon a certain upgrade to capture the corresponding physics) to study how smearing at the heterostructure interfaces affects the knee voltage of an LED structure, how the

presence of point defects (such as Ga- and/or N-vacancies and incorporation of interstitial atoms) and threading dislocations affect the carrier transport.

On the other hand, the study of electron transport using unipolar heterostructures indicates that a similar transport study of holes should also be conducted to understand their transport through an AlGaN barrier with special emphasis on how growth condition influences the electrical behaviour of the grown AlGaN layer. This from the gained experience should be a blend of both simulation and experiments which support each other and are meant to fill the knowledge gap of how effectively holes are injected (permitted) through an AlGaN layer into the active region and its dependence on barrier parameters.

Another experimental direction is to continue the path of template development based on our acquired insights regarding the topological evolution of a periodic µ-patterned surface. This requires further refining or combining the AlGaN overgrowth strategies into a two-step approach i.e. first using semipolar conditions and then coalescence conditions to achieve improvement in quality and a planar surface while growing thick enough to be able to assertively quantify and assess the quality of the coalesced layer. Moreover, it is believed that these types of templates realized using AlGaN overgrowth are prone to other issues such as a) poor surface morphology; b) the possibility of development of micro-cracks due to differences in gallium incorporation on the polar and non-polar planes during evolution, consequently this effect limits the UV transparency of the template; c) the light extraction capability of such templates. Since a significant amount of time was spent in understanding the topological evolution and finding the desired process parameters resulting in complete coalescence, these issues could not be entrained due to limited resources. However, it would be worth investigating these issues in a follow-up study.

A benefit of exploring these kinds of overgrown templates is their potential for integration with various heterogeneous platforms by transfer printing. So, a feasibility study should be conducted to test and optimize the thickness of the sacrificial layer which in our case can be *n*-(Al)GaN as it can be undercut using an electrochemical etch.

µ-LEDs is a topic of great interest to academicians and industry due to its extensive applications. So, if a graduate is inclined towards application-centric

research, then an interesting PhD thesis work can be the development of µ-LEDs grown on a-tilted semipolar facets. The first direct advantage of growing on a semipolar plane is the reduced polarization field which increases the overlap between electron and hole wavefunction resulting in increased internal quantum efficiency (the generation of a higher number of photons). In addition to that thicker quantum wells can be grown on these semipolar planes which further increase the number of emitted photons. Secondly, an increase in light extraction capabilities is possible due to the inclination of the facets, because the quantum wells grown on these structures can direct light to the bottom of the substrate while preventing light from being trapped in the material along the horizontal direction. A challenge on the fabrication side which can be foreseen is the uniform deposition of p-metal on the textured surface comprising of both c- and semipolar planes while preventing deposition in the centre of the V-pit region. Moreover, work is required on the mask design to achieve individual accessibility of each µ-Honeycomb structure and in a cluster operation configuration. In this regard, this thesis can provide significant level of awareness regarding growth on µ-patterned surfaces and prepare the graduate to come up the learning curve based on the fact that similar issues were encountered by me and new ideas of their own while developing the best quality semipolar faceted templates.

Overall, all the above-proposed works are scientifically valuable and have the potential to enrich our understanding of the field while being exciting and worth pursuing in a PhD thesis.

References

1. HEPACART. Far-UV VS. Near-UV. (2017). at <https://www.hepacart.com/blog/far-uv-vs.-near-uv>
2. Oguma, K., Kita, R., Sakai, H., Murakami, M. & Takizawa, S. Application of UV light emitting diodes to batch and flow-through water disinfection systems. *Desalination* **328,** 24–30 (2013).
3. Inagaki, H., Saito, A., Sugiyama, H., Okabayashi, T. & Fujimoto, S. Rapid inactivation of SARS-CoV-2 with deep-UV LED irradiation. *Emerging Microbes & Infections* **9,** 1744–1747 (2020).
4. Al-Smadi, K., Ali, M., Alavi, S. E., Jin, X., Imran, M., Leite-Silva, V. R. & Mohammed, Y. Using a Topical Formulation of Vitamin D for the Treatment of Vitiligo: A Systematic Review. *Cells* **12,** 2387 (2023).
5. Kfouri, M., Marinov, O., Quevedo, P., Faramarzpour, N., Shirani, S., Liu, L. W.-C., Fang, Q. & Deen, M. J. Toward a miniaturized wireless fluorescence-based diagnostic imaging system. *IEEE Journal of Selected Topics in Quantum Electronics* **14,** 226–234 (2008).
6. Ibrahim, W. I., Hassan, R. M., Ahmed, A. R. & Abdulkafi, A. Q. A cross-Sectional Study in Iraq of 145 Patients with Medullary Psoriasis.
7. Tian, P., Shan, X., Zhu, S., Xie, E., McKendry, J. J., Gu, E. & Dawson, M. D. AlGaN ultraviolet micro-LEDs. *IEEE Journal of Quantum Electronics* **58,** 1–14 (2022).
8. Dreyer, C. & Mildner, F. Application of LEDs for UV-curing. *III-Nitride Ultraviolet Emitters: Technology and Applications* 415–434 (2016).

9. Shiba, S. F., Tan, J. Y. & Kim, J. Multidirectional UV-LED lithography using an array of high-intensity UV-LEDs and tilt-rotational sample holder for 3-D microfabrication. *Micro and Nano Systems Letters* **8,** 1–12 (2020).
10. Parbrook, P. J. & Wang, T. Light emitting and laser diodes in the ultraviolet. *IEEE Journal of Selected Topics in Quantum Electronics* **17,** 1402–1411 (2011).
11. Mukish, P. & Boulay, P. UV LEDS and UV Lamps – Market & Technology Trends 2021 report. (2021). at <https://www.yolegroup.com/product/report/uv-leds-and-uv-lamps--market-and-technology-trends-2021/>
12. Davitt, K., Song, Y.-K., Patterson, W. R., Nurmikko, A. V., Gherasimova, M., Han, J., Pan, Y.-L. & Chang, R. K. 290 and 340 nm UV LED arrays for fluorescence detection from single airborne particles. *Optics express* **13,** 9548–9555 (2005).
13. Marcu, L., French, P. M. & Elson, D. S. *Fluorescence lifetime spectroscopy and imaging: principles and applications in biomedical diagnostics*. (CRC press, 2014).
14. Hellman, E. The polarity of GaN: a critical review. *Materials Research Society Internet Journal of Nitride Semiconductor Research* **3,** e11 (1998).
15. Morkoç, H. *Handbook of nitride semiconductors and devices, Materials Properties, Physics and Growth*. (John Wiley & Sons, 2009).
16. Wood, C. & Jena, D. *Polarization effects in semiconductors: from ab initio theory to device applications*. (Springer Science & Business Media, 2007).
17. Schubert, E. F. *Light-Emitting Diodes (2023)*. (E. Fred Schubert, 2023).
18. Moram, M. & Vickers, M. X-ray diffraction of III-nitrides. *Reports on progress in physics* **72,** 036502 (2009).

19. Dinh, van D. MOVPE growth of InN and InGaN with different surface orientations. (2012).
20. Li, H. MOVPE growth and characterization of Al (Ga) N and InAlN/AlGaN quantum wells for UV LED applications. (2015).
21. Norouzian Alam, S. Optimisation of high-efficiency UV and visible light sources utilising lateral localisation in InAlN and InGaN based nano-structure devices. (2018).
22. Pampili, P. Fabrication and characterization of UV-LEDs. (2019).
23. Malinverni, M. *Optimization of NH_3-MBE grown p-doped (Al) GaN layers and their implementation in long wavelength laser diodes and tunnel junctions*. (EPFL, 2015).
24. Vurgaftman, I. & Meyer, J. n. Band parameters for nitrogen-containing semiconductors. *Journal of Applied Physics* **94,** 3675–3696 (2003).
25. Romanov, A. E., Young, E. C., Wu, F., Tyagi, A., Gallinat, C. S., Nakamura, S., DenBaars, S. P. & Speck, J. S. Basal plane misfit dislocations and stress relaxation in III-nitride semipolar heteroepitaxy. *Journal of Applied Physics* **109,** (2011).
26. Lähnemann, J., Brandt, O., Jahn, U., Pfüller, C., Roder, C., Dogan, P., Grosse, F., Belabbes, A., Bechstedt, F., Trampert, A., & others. Direct experimental determination of the spontaneous polarization of GaN. *Physical Review B* **86,** 081302 (2012).
27. Ambacher, O., Majewski, J., Miskys, C., Link, A., Hermann, M., Eickhoff, M., Stutzmann, M., Bernardini, F., Fiorentini, V., Tilak, V., & others. Pyroelectric properties of Al (In) GaN/GaN hetero-and quantum well structures. *Journal of physics: condensed matter* **14,** 3399 (2002).

28. Stutzmann, M., Ambacher, O., Eickhoff, M., Karrer, U., Lima Pimenta, A., Neuberger, R., Schalwig, J., Dimitrov, R., Schuck, P. & Grober, R. Playing with polarity. *physica status solidi (b)* **228,** 505–512 (2001).

29. Ren, C. Polarisation fields in III-nitrides: effects and control. *Materials Science and Technology* **32,** 418–433 (2016).

30. Kolník, J., Oğuzman, İ. H., Brennan, K. F., Wang, R., Ruden, P. P. & Wang, Y. Electronic transport studies of bulk zincblende and wurtzite phases of GaN based on an ensemble Monte Carlo calculation including a full zone band structure. *Journal of Applied Physics* **78,** 1033–1038 (1995).

31. Dingle, R., Shaklee, K., Leheny, R. & Zetterstrom, R. Stimulated emission and laser action in gallium nitride. *Applied Physics Letters* **19,** 5–7 (1971).

32. Fritsch, D., Schmidt, H. & Grundmann, M. Band-structure pseudopotential calculation of zinc-blende and wurtzite AlN, GaN, and InN. *Physical review B* **67,** 235205 (2003).

33. Jiang, X., Shi, J., Zhang, M., Zhong, H., Huang, P., Ding, Y., Yu, T., Shen, B., Lu, J. & Wang, X. Enhancement of TE polarized light extraction efficiency in nanoscale (AlN) m/(GaN) n (m> n) superlattice substitution for Al-rich AlGaN disorder alloy: ultra-thin GaN layer modulation. *New Journal of Physics* **16,** 113065 (2014).

34. Liou, B.-T., Yen, S.-H. & Kuo, Y.-K. Vegard's law deviation in band gaps and bowing parameters of the wurtzite III-nitride ternary alloys. in *Semiconductor Lasers and Applications II* **5628,** 296–305 (SPIE, 2005).

35. Nam, K., Li, J., Nakarmi, M., Lin, J. & Jiang, H. Unique optical properties of AlGaN alloys and related ultraviolet emitters. *Applied physics letters* **84,** 5264–5266 (2004).

36. Jmerik, V., Lutsenko, E. & Ivanov, S. Plasma-assisted molecular beam epitaxy of AlGaN heterostructures for deep-ultraviolet optically pumped lasers. *physica status solidi (a)* **210,** 439–450 (2013).

37. Teofilov, N., Thonke, K., Sauer, R., Kirste, L., Ebling, D. & Benz, K. Optical investigation of AlxGa1- xN epitaxial films grown on AlN buffer layers. *Diamond and related materials* **11,** 892–895 (2002).

38. Koide, Y., Itoh, H., Khan, M., Hiramatu, K., Sawaki, N. & Akasaki, I. Energy band-gap bowing parameter in an Al x Ga1- x N alloy. *Journal of applied physics* **61,** 4540–4543 (1987).

39. Buchheim, C., Goldhahn, R., Rakel, M., Cobet, C., Esser, N., Rossow, U., Fuhrmann, D. & Hangleiter, A. Dielectric function and critical points of the band structure for AlGaN alloys. *physica status solidi (b)* **242,** 2610–2616 (2005).

40. Coughlan, C., Schulz, S., Caro, M. A. & O'Reilly, E. P. Band gap bowing and optical polarization switching in AlGaN alloys. *physica status solidi (b)* **252,** 879–884 (2015).

41. Fiorentini, V., Bernardini, F. & Ambacher, O. Evidence for nonlinear macroscopic polarization in III–V nitride alloy heterostructures. *Applied physics letters* **80,** 1204–1206 (2002).

42. Waltereit, P., Brandt, O., Trampert, A., Grahn, H., Menniger, J., Ramsteiner, M., Reiche, M. & Ploog, K. Nitride semiconductors free of electrostatic fields for efficient white light-emitting diodes. *nature* **406,** 865–868 (2000).

43. Nishida, T. & Kobayashi, N. 346 nm Emission from AlGaN Multi-Quantum-Well Light Emitting Diode. *physica status solidi (a)* **176,** 45–48 (1999).

44. Kneissl, M., Rass, J., & others. III-Nitride ultraviolet emitters. *Springer Series in Materials Science* (2016).

45. Karpov, S. Y. & Makarov, Y. N. Dislocation effect on light emission efficiency in gallium nitride. *Applied Physics Letters* **81,** 4721–4723 (2002).

46. Royer, L. Recherches expérimentales sur l'épitaxie ou orientation mutuelle de cristaux d'espèces différentes. *Bulletin de Minéralogie* **51,** 7–159 (1928).

47. Ohring, M., Zarrabian, S. & Grogan, A. The materials science of thin films. *Appl. Opt* **31,** 7162 (1992).

48. Amano, H., Akasaki, I., Hiramatsu, K., Koide, N. & Sawaki, N. Effects of the buffer layer in metalorganic vapour phase epitaxy of GaN on sapphire substrate. *Thin Solid Films* **163,** 415–420 (1988).

49. Zhang, B., Egawa, T., Ishikawa, H., Liu, Y. & Jimbo, T. Thermal stability of InGaN multiple-quantum-well light-emitting diodes on an AlN/sapphire template. *Journal of applied physics* **95,** 3170–3174 (2004).

50. Zhao, D., Zhu, J., Liu, Z., Zhang, S., Yang, H. & Jiang, D. Surface morphology of AlN buffer layer and its effect on GaN growthby metalorganic chemical vapor deposition. *Applied physics letters* **85,** 1499–1501 (2004).

51. Brunner, F., Knauer, A., Schenk, T., Weyers, M. & Zettler, J.-T. Quantitative analysis of in situ wafer bowing measurements for III-nitride growth on sapphire. *Journal of Crystal Growth* **310,** 2432–2438 (2008).

52. Schubert, E. F. Light emitting diodes and solid-state lighting. *URL https://www. ecse. rpi. edu/∼ schubert/Light-Emitting-Diodes-dot-org/LED-slide-show. pdf* (2006).

53. Pernot, C., Fukahori, S., Inazu, T., Fujita, T., Kim, M., Nagasawa, Y., Hirano, A., Ippommatsu, M., Iwaya, M., Kamiyama, S., & others. Development of high efficiency 255–355 nm AlGaN-based light-emitting diodes. *physica status solidi (a)* **208,** 1594–1596 (2011).

54. Iwaya, M., Terao, S., Sano, T., Takanami, S., Ukai, T., Nakamura, R., Kamiyama, S., Amano, H. & Akasaki, I. High-Efficiency GaN/AlxGa1—xN Multi-Quantum-Well Light Emitter Grown on Low-Dislocation Density AlxGa1—xN. *physica status solidi (a)* **188,** 117–120 (2001).
55. Takeda, K., Mori, F., Ogiso, Y., Ichikawa, T., Nonaka, K., Iwaya, M., Kamiyama, S., Amano, H. & Akasaki, I. Internal quantum efficiency of GaN/AlGaN-based multi quantum wells on different dislocation densities underlying layers. *physica status solidi c* **7,** 1916–1918 (2010).
56. Bryan, I., Bryan, Z., Washiyama, S., Reddy, P., Gaddy, B., Sarkar, B., Breckenridge, M. H., Guo, Q., Bobea, M., Tweedie, J., & others. Doping and compensation in Al-rich AlGaN grown on single crystal AlN and sapphire by MOCVD. *Applied Physics Letters* **112,** (2018).
57. Weinrich, J., Mogilatenko, A., Brunner, F., Koch, C. & Weyers, M. Extra half-plane shortening of dislocations as an origin of tensile strain in Si-doped (Al) GaN. *Journal of Applied Physics* **126,** (2019).
58. Wang, H.-M., Zhang, J.-P., Chen, C.-Q., Fareed, Q., Yang, J.-W. & Khan, M. A. AlN/AlGaN superlattices as dislocation filter for low-threading-dislocation thick AlGaN layers on sapphire. *Applied physics letters* **81,** 604–606 (2002).
59. Adivarahan, V., Wu, S., Sun, W., Mandavilli, V., Shatalov, M., Simin, G., Yang, J., Maruska, H. & Khan, M. A. High-power deep ultraviolet light-emitting diodes basedon a micro-pixel design. *Applied physics letters* **85,** 1838–1840 (2004).
60. Shatalov, M., Simin, G., Adivarahan, V., Chitnis, A., Wu, S., Pachipulusu, R., Mandavilli, V., Simin, K., Zhang, J. P., Yang, J. W., & others. Lateral current crowding in deep UV light emitting diodes over sapphire substrates. *Japanese journal of applied physics* **41,** 5083 (2002).

61. Iwaya, M., Takeuchi, T., Yamaguchi, S., Wetzel, C., Amano, H. & Akasaki, I. Reduction of etch pit density in organometallic vapor phase epitaxy-grown GaN on sapphire by insertion of a low-temperature-deposited buffer layer between high-temperature-grown GaN. *Japanese Journal of Applied Physics* **37,** L316 (1998).

62. Xi, Y., Chen, K., Mont, F., Kim, J., Schubert, E., Liu, W., Li, X. & Smart, J. Comparative study of n-type AlGaN grown on sapphire by using a superlattice layer and a low-temperature AlN interlayer. *Journal of crystal growth* **299,** 59–62 (2007).

63. Scholz, F., Forghani, K., Klein, M., Klein, O., Kaiser, U., Neuschl, B., Tischer, I., Feneberg, M., Thonke, K., Lazarev, S., & others. Studies on defect reduction in AlGaN heterostructures by integrating an in-situ SiN interlayer. *Japanese Journal of Applied Physics* **52,** 08JJ07 (2013).

64. Zhang, J., Wang, H. M., Gaevski, M. E., Chen, C., Fareed, Q., Yang, J., Simin, G. & Khan, M. A. Crack-free thick AlGaN grown on sapphire using AlN/AlGaN superlattices for strain management. *Applied physics letters* **80,** 3542–3544 (2002).

65. Crawford, M. H., Allerman, A. A., Armstrong, A. M., Smith, M. L. & Cross, K. C. Laser diodes with 353 nm wavelength enabled by reduced-dislocation-density AlGaN templates. *Applied Physics Express* **8,** 112702 (2015).

66. Fan, T., Jia, W., Tong, G., Zhai, G., Li, T., Dong, H. & Xu, B. Influence of in-situ deposited SiNx interlayer on crystal quality of GaN epitaxial films. *Superlattices and Microstructures* **117,** 57–64 (2018).

67. Hiramatsu, K., Nishiyama, K., Onishi, M., Mizutani, H., Narukawa, M., Motogaito, A., Miyake, H., Iyechika, Y. & Maeda, T. Fabrication and

characterization of low defect density GaN using facet-controlled epitaxial lateral overgrowth (FACELO). *Journal of Crystal Growth* **221,** 316–326 (2000).

68. Kamiyama, S., Iwaya, M., Takanami, S., Terao, S., Miyazaki, A., Amano, H. & Akasaki, I. UV Light-Emitting Diode Fabricated on Hetero-ELO-Grown Al0. 22Ga0. 78N with Low Dislocation Density. *physica status solidi (a)* **192,** 296–300 (2002).
69. Wang, K. *Development of Crack-free AlGaN on GaN based on Facet-Controlled Epitaxial Lateral Overgrowth*. (North Carolina State University, 2020).
70. Yoshida, H., Kuwabara, M., Yamashita, Y., Takagi, Y., Uchiyama, K. & Kan, H. AlGaN-based laser diodes for the short-wavelength ultraviolet region. *New Journal of Physics* **11,** 125013 (2009).
71. Taketomi, H., Aoki, Y., Takagi, Y., Sugiyama, A., Kuwabara, M. & Yoshida, H. Over 1 W record-peak-power operation of a 338 nm AlGaN multiple-quantum-well laser diode on a GaN substrate. *Japanese Journal of Applied Physics* **55,** 05FJ05 (2016).
72. Kueller, V., Knauer, A., Brunner, F., Zeimer, U., Rodriguez, H., Kneissl, M. & Weyers, M. Growth of AlGaN and AlN on patterned AlN/sapphire templates. *Journal of Crystal Growth* **315,** 200–203 (2011).
73. Iwaya, M., Terao, S., Sano, T., Ukai, T., Nakamura, R., Kamiyama, S., Amano, H. & Akasaki, I. Suppression of phase separation of AlGaN during lateral growth and fabrication of high-efficiency UV-LED on optimized AlGaN. *Journal of crystal growth* **237,** 951–955 (2002).
74. Allerman, A. A., Crawford, M. H., Lee, S. & Clark, B. Low dislocation density AlGaN epilayers by epitaxial overgrowth of patterned templates. *Journal of Crystal Growth* **388,** 76–82 (2014).

75. Conroy, M., Zubialevich, V. Z., Li, H., Petkov, N., O'Donoghue, S., Holmes, J. D. & Parbrook, P. J. Ultra-high-density arrays of defect-free aln nanorods: A "space-filling" approach. *ACS nano* **10,** 1988–1994 (2016).

76. Omori, T., Yabutani, A., Tanaka, S., Yamada, K., Shimokawa, M., Hasegawa, R., Iwayama, S., Miyake, H., Takeuchi, T., Kamiyama, S., & others. Reduction of dislocation density in lattice-relaxed Al0. 68Ga0. 32N film grown on periodical 1 μm spacing AlN pillar concave-convex patterns and its effect on the performance of UV-B laser diodes. *Applied Physics Express* **15,** 031004 (2022).

77. Hunt, N., Schubert, E., Sivco, D., Cho, A. & Zydzik, G. Power and efficiency limits in single-mirror light emitting diodes with enhanced intensity. *Electronics Letters* **28,** 2169–2171 (1992).

78. Tu, R.-C., Tun, C.-J., Pan, S.-M., Chuo, C.-C., Sheu, J., Tsai, C.-E., Wang, T.-C. & Chi, G.-C. Improvement of near-ultraviolet InGaN-GaN light-emitting diodes with an AlGaN electron-blocking layer grown at low temperature. *IEEE Photonics Technology Letters* **15,** 1342–1344 (2003).

79. Hirayama, H., Tsukada, Y., Maeda, T. & Kamata, N. Marked enhancement in the efficiency of deep-ultraviolet AlGaN light-emitting diodes by using a multiquantum-barrier electron blocking layer. *Applied Physics Express* **3,** 031002 (2010).

80. Lee, K., Parbrook, P., Wang, T., Bai, J., Ranalli, F., Airey, R. & Hill, G. Effect of the AlGaN electron blocking layer thickness on the performance of AlGaN-based ultraviolet light-emitting diodes. *Journal of crystal growth* **311,** 2857–2859 (2009).

81. Pandey, A., Shin, W., Liu, X. & Mi, Z. Effect of electron blocking layer on the efficiency of AlGaN mid-ultraviolet light emitting diodes. *Optics express* **27,** A738–A745 (2019).

82. Nath, D., Yang, Z., Lee, C.-Y., Park, P., Wu, Y.-R. & Rajan, S. Unipolar vertical transport in GaN/AlGaN/GaN heterostructures. *Applied Physics Letters* **103,** (2013).

83. Browne, D. A., Fireman, M. N., Mazumder, B., Kuritzky, L. Y., Wu, Y.-R. & Speck, J. S. Vertical transport through AlGaN barriers in heterostructures grown by ammonia molecular beam epitaxy and metalorganic chemical vapor deposition. *Semiconductor Science and Technology* **32,** 025010 (2017).

84. Stringfellow, G. B. *Organometallic vapor-phase epitaxy: theory and practice*. (Elsevier, 1999).

85. Johnson, M., Yu, Z., Brown, J., Koeck, F., El-Masry, N., Kong, H., Edmond, J., Cook, J. & Schetzina, J. A Critical Comparison Between Movpe and MBE Growth of III-V Nitride Semiconductor Materials for Opto-Electronic Device Applications. *MRS Online Proceedings Library (OPL)* **537,** G5-10 (1998).

86. Herman, M. A., Richter, W. & Sitter, H. *Epitaxy: physical principles and technical implementation*. **62,** (Springer Science & Business Media, 2013).

87. maxxl2 & Patrick87. *MOVPE surface processes*. (2013). at <https://commons.wikimedia.org/wiki/File:MOVPE_surface_processes.svg>

88. Webb, T. *3x2FT system System Manual*. (AIXTRON Ltd).

89. Li, H., Sadler, T. C. & Parbrook, P. J. AlN heteroepitaxy on sapphire by metalorganic vapour phase epitaxy using low temperature nucleation layers. *Journal of Crystal Growth* **383,** 72–78 (2013).

90. Han, J., Waldrip, K., Lee, S. R., Figiel, J. J., Hearne, S., Petersen, G. A. & Myers, S. Control and elimination of cracking of AlGaN using low-temperature AlGaN interlayers. *Applied Physics Letters* **78,** 67–69 (2001).

91. Waldrip, K., Han, J., Figiel, J. J., Zhou, H., Makarona, E. & Nurmikko, A. Stress engineering during metalorganic chemical vapor deposition of AlGaN/GaN distributed Bragg reflectors. *Applied Physics Letters* **78,** 3205–3207 (2001).

92. Bläsing, J., Reiher, A., Dadgar, A., Diez, A. & Krost, A. The origin of stress reduction by low-temperature AlN interlayers. *Applied physics letters* **81,** 2722–2724 (2002).

93. Amano, H., Iwaya, M., Kashima, T., Katsuragawa, M., Akasaki, I., Han, J., Hearne, S., Floro, J. A., Chason, E. & Figiel, J. Stress and defect control in GaN using low temperature interlayers. *Japanese journal of applied physics* **37,** L1540 (1998).

94. Amano, H., Iwaya, M., Hayashi, N., Kashima, T., Nitta, S., Wetzel, C. & Akasaki, I. Control of dislocations and stress in AlGaN on sapphire using a low temperature interlayer. *physica status solidi (b)* **216,** 683–689 (1999).

95. Luo, W., Wang, X., Guo, L., Xiao, H., Wang, C., Ran, J., Li, J. & Li, J. The effect of low temperature AlN interlayers on the growth of GaN epilayer on Si (111) by MOCVD. *Superlattices and Microstructures* **44,** 153–159 (2008).

96. Kidd, P. XRD of gallium nitride and related compounds: strain, composition and layer thickness. *Panalytical: Almelo, Netherlands* 119 (2009).

97. Schuster, M., Gervais, P., Jobst, B., Hösler, W., Averbeck, R., Riechert, H., Iberl, A. & Stömmer, R. Determination of the chemical composition of distorted InGaN/GaN heterostructures from x-ray diffraction data. *Journal of Physics D: Applied Physics* **32,** A56 (1999).

98. Wyatt Tyrone Smith. Electron beam sample interactions. *Electron beam sample interactions* (2020). at <https://commons.wikimedia.org/wiki/File:Electron_beam_sample_interactions.png>

99. Lang, W. & others. Nomarski differential interference-contrast microscopy. (1982).

100. Singh, S. M., Zubialevich, V. Z. & Parbrook, P. J. Surface Morphology Evolution of AlGaN Microhoneycomb Structures during Epitaxial Overgrowth. *physica status solidi (b)* 2300471 (2024).

101. Selberherr, S. *Analysis and simulation of semiconductor devices*. (Springer Science & Business Media, 2012).

102. Silvaco, A. U. M. D. Simulation Software. *Santa Clara CA: Silvaco International* **444,** (2018).

103. Li, C.-K., Piccardo, M., Lu, L.-S., Mayboroda, S., Martinelli, L., Peretti, J., Speck, J. S., Weisbuch, C., Filoche, M. & Wu, Y.-R. Localization landscape theory of disorder in semiconductors. III. Application to carrier transport and recombination in light emitting diodes. *Physical Review B* **95,** 144206 (2017).

104. Piprek, J. *Semiconductor optoelectronic devices: introduction to physics and simulation*. (Elsevier, 2013).

105. Nguyen, D.-P., Regnault, N., Ferreira, R. & Bastard, G. Alloy effects in Ga1-xInxN/GaN heterostructures. *Solid state communications* **130,** 751–754 (2004).

106. Mazumder, B., Kaun, S. W., Lu, J., Keller, S., Mishra, U. K. & Speck, J. S. Atom probe analysis of AlN interlayers in AlGaN/AlN/GaN heterostructures. *Applied Physics Letters* **102,** (2013).

107. Morris, R. J., Cuduvally, R., Melkonyan, D., Zhao, M., van der Heide, P. & Vandervorst, W. Atom probe of GaN/AlGaN heterostructures: The role of electric field, sample crystallography and laser excitation on quantification. *Ultramicroscopy* **206,** 112813 (2019).

108. Wu, Y.-R., Shivaraman, R., Wang, K.-C. & Speck, J. S. Analyzing the physical properties of InGaN multiple quantum well light emitting diodes from nano scale structure. *Applied Physics Letters* **101,** (2012).

109. Tang, F., Zhu, T., Fu, W.-Y., Oehler, F., Zhang, S., Griffiths, J. T., Humphreys, C., Martin, T. L., Bagot, P. A., Moody, M. P., & others. Insight into the impact of atomic-and nano-scale indium distributions on the optical properties of InGaN/GaN quantum well structures grown on m-plane freestanding GaN substrates. *Journal of Applied Physics* **125,** (2019).

110. Tang, F., Zhu, T., Oehler, F., Fu, W. Y., Griffiths, J. T., Massabuau, F. C.-P., Kappers, M. J., Martin, T. L., Bagot, P. A., Moody, M. P., & others. Indium clustering in a-plane InGaN quantum wells as evidenced by atom probe tomography. *Applied Physics Letters* **106,** (2015).

111. Schulz, S., Caro, M. A., Coughlan, C. & O'Reilly, E. P. Atomistic analysis of the impact of alloy and well-width fluctuations on the electronic and optical properties of InGaN/GaN quantum wells. *Physical Review B* **91,** 035439 (2015).

112. O'Donovan, M., Luisier, M., O'Reilly, E. P. & Schulz, S. Impact of random alloy fluctuations on inter-well transport in InGaN/GaN multi-quantum well systems: an atomistic non-equilibrium Green's function study. *Journal of Physics: Condensed Matter* **33,** 045302 (2020).

113. Yang, T.-J., Shivaraman, R., Speck, J. S. & Wu, Y.-R. The influence of random indium alloy fluctuations in indium gallium nitride quantum wells on the device behavior. *Journal of Applied Physics* **116,** (2014).

114. Baranovskii, S. & Efros, A. Band edge smearing in solid solutions. *Sov. Phys. Semicond.,* **12,** 1328–1330 (1978).

115. Brunner, D., Angerer, H., Bustarret, E., Freudenberg, F., Höpler, R., Dimitrov, R., Ambacher, O. & Stutzmann, M. Optical constants of epitaxial AlGaN films and their temperature dependence. *Journal of applied physics* **82,** 5090–5096 (1997).

116. Kaun, S. W., Mazumder, B., Fireman, M. N., Kyle, E. C., Mishra, U. K. & Speck, J. S. Pure AlN layers in metal-polar AlGaN/AlN/GaN and AlN/GaN heterostructures grown by low-temperature ammonia-based molecular beam epitaxy. *Semiconductor Science and Technology* **30,** 055010 (2015).

117. Lu, J., Hu, Y.-L., Brown, D. F., Wu, F., Keller, S., Speck, J. S., DenBaars, S. P. & Mishra, U. K. Charge and Mobility Enhancements in In-Polar InAl (Ga) N/Al (Ga) N/GaN Heterojunctions Grown by Metal–Organic Chemical Vapor Deposition Using a Graded Growth Strategy. *Japanese Journal of Applied Physics* **51,** 115502 (2012).

118. Chen, X., Lin, N., Cai, D., Zhang, Y., Chen, H. & Kang, J. Symmetrically abrupt GaN/AlGaN superlattices by alternative interface–interruption scheme. *Journal of Materials Research* **28,** 716–722 (2013).

119. Amari, H., Ross, I., Wang, T. & Walther, T. Characterization of thickness, elemental distribution and band-gap properties in AlGaN/GaN quantum wells by aberration-corrected TEM/STEM. in *Journal of Physics: Conference Series* **371,** 012014 (IOP Publishing, 2012).

120. Svensk, O., Törmä, P., Suihkonen, S., Ali, M., Lipsanen, H., Sopanen, M., Odnoblyudov, M. & Bougrov, V. Enhanced electroluminescence in 405 nm InGaN/GaN LEDs by optimized electron blocking layer. *Journal of Crystal Growth* **310,** 5154–5157 (2008).

121. Su, C.-Y., Tu, C.-G., Liu, W.-H., Lin, C.-H., Yao, Y.-F., Chen, H.-T., Wu, Y.-R., Kiang, Y.-W. & Yang, C.-C. Enhancing the hole-injection efficiency of a light-emitting diode by increasing Mg doping in the p-AlGaN electron-blocking layer. *IEEE Transactions on Electron Devices* **64,** 3226–3233 (2017).

122. Caro, M. A., Schulz, S., Healy, S. & O'Reilly, E. P. Built-in field control in alloyed c-plane III-N quantum dots and wells. *Journal of Applied Physics* **109,** (2011).

123. Smith, M. D., Thomson, D., Zubialevich, V. Z., Li, H., Naresh-Kumar, G., Trager-Cowan, C. & Parbrook, P. J. Nanoscale fissure formation in AlxGa1–xN/GaN heterostructures and their influence on Ohmic contact formation. *physica status solidi (a)* **214,** 1600353 (2017).

124. Hinz, A. M., Ghosh, S., Fairclough, S. M., Griffiths, J. T., Kappers, M. J., Oliver, R. A. & Wallis, D. J. Strategy for reliable growth of thin GaN Caps on AlGaN HEMT structures. *Journal of Crystal Growth* **624,** 127420 (2023).

125. Moszak, K., Pucicki, D., Grodzicki, M., Olszewski, W., Majchrzak, D., Serafińczuk, J., Gorantla, S. & Hommel, D. Growth and properties of the GaN cap layer strongly influenced by the composition of the underlying AlGaN. *Materials Science in Semiconductor Processing* **136,** 106125 (2021).

126. Korakakis, D., Ludwig, K. & Moustakas, T. Long range order in AlxGa1- xN films grown by molecular beam epitaxy. *Applied physics letters* **71,** 72–74 (1997).

127. Kirste, L., Pavlov, K. M., Mudie, S. T., Punegov, V. I. & Herres, N. Analysis of the mosaic structure of an ordered (Al, Ga) N layer. *Journal of applied crystallography* **38,** 183–192 (2005).

128. Albrecht, M., Lymperakis, L., Neugebauer, J., Northrup, J., Kirste, L., Leroux, M., Grzegory, I., Porowski, S. & Strunk, H. Chemically ordered Al x Ga 1- x N alloys: Spontaneous formation of natural quantum wells. *Physical Review B* **71,** 035314 (2005).

129. Wise, A., Kim, D.-W., Newman, N. & Mahajan, S. Atomic ordering in AlxGa1-xN thin-films. *Scripta materialia* **54,** 153–157 (2006).

130. Jianchang, Y., Junxi, W., Naixin, L., Zhe, L., Jun, R. & Jinmin, L. High quality AlGaN grown on a high temperature AIN template by MOCVD. *Journal of Semiconductors* **30,** 103001 (2009).

131. Jie, Z., Li-Wei, G., Yao, C., Pei-Qiang, X., Guo-Jian, D., Ming-Zeng, P., Hai-Qiang, J., Jun-Ming, Z. & Hong, C. Growth and Characteristics of Epitaxial AlxGa1- xN by MOCVD. *Chinese Physics Letters* **26,** 068101 (2009).

132. Hanser, D., Preble, E., Clites, T., Stephenson, T., Jacobs, R., Johnson, T., Paskova, T. & Evans, K. PVD of AlN nucleation layers for GaN-based LED structures: a cheaper and brighter alternative. in *CS MANTECH Conference* 18–21 (Citeseer, 2009).

133. O'Connell, J., Lee, M., Westraadt, J. & Engelbrecht, J. Defect characterization of MOCVD grown AlN/AlGaN films on sapphire substrates by TEM and TKD. *Physica B: Condensed Matter* **535,** 293–298 (2018).

134. Yin, J., Chen, D., Yang, H., Liu, Y., Talwar, D. N., He, T., Ferguson, I. T., He, K., Wan, L. & Feng, Z. C. Comparative spectroscopic studies of MOCVD grown

AlN films on Al2O3 and 6H–SiC. *Journal of Alloys and Compounds* **857,** 157487 (2021).

135. Jayasakthi, M., Juillaguet, S., Peyre, H., Konczewicz, L., Baskar, K. & Contreras, S. Influence of AlN thickness on AlGaN epilayer grown by MOCVD. *Superlattices and Microstructures* **98,** 515–521 (2016).
136. Khan, M. A., Maeda, N., Jo, M., Yamada, Y. & Hirayama, H. Highly Transparent p-AlGaN-Based (326–341 nm)-Band Ultraviolet-A Light-Emitting Diodes on AlN Templates: Recent Advances and Perspectives. *physica status solidi (a)* **219,** 2100605 (2022).
137. Forghani, K., Schade, L., Schwarz, U. T., Lipski, F., Klein, O., Kaiser, U. & Scholz, F. Strain and defects in Si-doped (Al) GaN epitaxial layers. *Journal of Applied Physics* **112,** (2012).
138. Chen, J., Liu, J., Huang, Y., Liu, R., Dai, Y., Tang, L., Chen, Z., Sun, X., Liu, C., Zhang, S., & others. Hillock Related Degradation Mechanism for AlGaN-Based UVC LEDs. *Nanomaterials* **13,** 1562 (2023).
139. Oehler, F., Zhu, T., Rhode, S., Kappers, M., Humphreys, C. & Oliver, R. Surface morphology of homoepitaxial c-plane GaN: Hillocks and ridges. *Journal of crystal growth* **383,** 12–18 (2013).
140. Ubukata, A., Yano, Y., Yamaoka, Y., Kitamura, Y., Tabuchi, T. & Matsumoto, K. High growth rates of AlN and AlGaN on 8 ″silicon wafer using metal-organic vapor phase epitaxy reactor. *physica status solidi (c)* **10,** 1353–1356 (2013).
141. Keller, S., Parish, G., Fini, P., Heikman, S., Chen, C.-H., Zhang, N., DenBaars, S., Mishra, U. & Wu, Y.-F. Metalorganic chemical vapor deposition of high mobility AlGaN/GaN heterostructures. *Journal of applied physics* **86,** 5850–5857 (1999).

142. Allerman, A., Crawford, M., Fischer, A., Bogart, K., Lee, S., Follstaedt, D., Provencio, P. & Koleske, D. Growth and design of deep-UV (240–290 nm) light emitting diodes using AlGaN alloys. *Journal of crystal growth* **272,** 227–241 (2004).

143. Lobanova, A., Mazaev, K., Talalaev, R., Leys, M., Boeykens, S., Cheng, K. & Degroote, S. Effect of V/III ratio in AlN and AlGaN MOVPE. *Journal of crystal growth* **287,** 601–604 (2006).

144. Armstrong, R., Coulon, P., Bozinakis, P., Martin, R. & Shields, P. Creation of regular arrays of faceted AlN nanostructures via a combined top-down, bottom-up approach. *Journal of Crystal Growth* **548,** 125824 (2020).

145. Krzyżewski, F., Załuska-Kotur, M. A., Turski, H., Sawicka, M. & Skierbiszewski, C. Miscut dependent surface evolution in the process of N-polar GaN (0001\=) growth under N-rich condition. *Journal of Crystal Growth* **457,** 38–45 (2017).

146. Ashby, C. I., Mitchell, C. C., Han, J., Missert, N. A., Provencio, P. P., Follstaedt, D. M., Peake, G. M. & Griego, L. Low-dislocation-density GaN from a single growth on a textured substrate. *Applied Physics Letters* **77,** 3233–3235 (2000).

147. Follstaedt, D. M., Allerman, A. A., Lee, S. R., Michael, J. R., Bogart, K., Crawford, M. H. & Missert, N. A. Dislocation reduction in AlGaN grown on patterned GaN. *Journal of crystal growth* **310,** 766–776 (2008).

148. Liu, Z., Hyun, B.-R., Sheng, Y., Lin, C.-J., Changhu, M., Lin, Y., Ho, C.-H., He, J.-H. & Kuo, H.-C. Micro-light-emitting diodes based on InGaN materials with quantum dots. *Advanced Materials Technologies* **7,** 2101189 (2022).

149. Adhikari, S., Lem, O. L. C., Kremer, F., Vora, K., Brink, F., Lysevych, M., Tan, H. H. & Jagadish, C. Nonpolar Al x Ga1- x N/Al y Ga1- y N multiple quantum wells on GaN nanowire for UV emission. *Nano Research* **15,** 7670–7680 (2022).

150. Zubialevich, V. Z., Pampili, P. & Parbrook, P. J. Thermal stability of crystallographic planes of GaN nanocolumns and their overgrowth by metal organic vapor phase epitaxy. *Crystal Growth & Design* **20,** 3686–3700 (2020).

151. Hartmann, J., Steib, F., Zhou, H., Ledig, J., Fündling, S., Albrecht, F., Schimpke, T., Avramescu, A., Varghese, T., Wehmann, H.-H., & others. High aspect ratio GaN fin microstructures with nonpolar sidewalls by continuous mode metalorganic vapor phase epitaxy. *Crystal Growth & Design* **16,** 1458–1462 (2016).

152. Leung, B., Sun, Q., Yerino, C. D., Han, J. & Coltrin, M. E. Using the kinetic Wulff plot to design and control nonpolar and semipolar GaN heteroepitaxy. *Semiconductor Science and Technology* **27,** 024005 (2012).

153. De Donno, M., Albani, M., Bergamaschini, R. & Montalenti, F. Phase-field modeling of the morphological evolution of ringlike structures during growth: Thermodynamics, kinetics, and template effects. *Physical Review Materials* **6,** 023401 (2022).

154. Wang, N., Yuan, X., Zhang, X., Gao, Q., Zhao, B., Li, L., Lockrey, M., Tan, H. H., Jagadish, C. & Caroff, P. Shape engineering of InP nanostructures by selective area epitaxy. *ACS nano* **13,** 7261–7269 (2019).

155. Feenstra, R. M., Dong, Y., Lee, C. & Northrup, J. Recent developments in surface studies of GaN and AlN. *Journal of Vacuum Science & Technology B: Microelectronics and Nanometer Structures Processing, Measurement, and Phenomena* **23,** 1174–1180 (2005).

156. Akiyama, T., Seta, Y., Nakamura, K. & Ito, T. Modified approach for calculating individual energies of polar and semipolar surfaces of group-III nitrides. *Physical Review Materials* **3,** 023401 (2019).

157. Van de Walle, C. G. & Neugebauer, J. Role of hydrogen in surface reconstructions and growth of GaN. *Journal of Vacuum Science & Technology B: Microelectronics and Nanometer Structures Processing, Measurement, and Phenomena* **20,** 1640–1646 (2002).

158. Van de Walle, C. G. & Neugebauer, J. First-principles surface phase diagram for hydrogen on GaN surfaces. *Physical review letters* **88,** 066103 (2002).

159. Hiramatsu, K., Nishiyama, K., Motogaito, A., Miyake, H., Iyechika, Y. & Maeda, T. Recent progress in selective area growth and epitaxial lateral overgrowth of III-nitrides: effects of reactor pressure in MOVPE growth. *physica status solidi (a)* **176,** 535–543 (1999).

Appendix

FWHM values along 0002 and $10\bar{1}1$ direction of a sample (2879) was assessed to determine the margin of error in the XRD measurement. Eight successive measurements were acquired by rotating the sample during measurements and are shown in Figure 104 and presented in the Table 9.

Table 9: FWHM data of sample 2879 measured using XRD.

#	(0002)			$(10\bar{1}1)$		
	FWHM arcsec	$\Delta\omega$ $\lvert(x_i-\bar{x})\rvert$ arcsec	$\Delta\omega$ $\lvert(x_i-\bar{x})\rvert/7.92$	FWHM arcsec	$\Delta\omega$ $\lvert(x_i-\bar{x})\rvert$ arcsec	$\Delta\omega$ $\lvert(x_i-\bar{x})\rvert/20.4$
1	223.2	13.14	1.66σ	1020.6	12.96	0.63σ
2	204.12	5.94	0.75σ	1021.68	14.04	0.69σ
3	208.8	1.26	0.16σ	1019.52	11.88	0.58σ
4	205.2	4.86	0.61σ	1029.96	22.32	1.09σ
5	199.44	10.62	1.34σ	1017.72	10.08	0.49σ
6	219.24	9.18	1.16σ	974.52	33.12	1.61σ
7	208.08	1.98	0.25σ	990	17.64	0.86σ
8	212.4	2.34	0.3σ	987.12	20.52	1.0σ

The values from Table 9 were used to obtain the sum (using equation 3), mean (using equation 4) and standard deviation of the FWHM values using equation 5. All these equations are already included in the standard deviation calculator[1].

$$\text{sum} = \sum_{i=1}^{N} x_i \qquad 3$$

$$\bar{x} = \frac{1}{N}(\text{sum}) \qquad 4$$

$$\sigma = \sqrt{\frac{1}{N\text{-}1}\sum_{i=1}^{N}(x_i\text{-}\bar{x})^2} \qquad 5$$

where x_i is the FWHM value obtained in a measurement, N is the total number of measure values of the dataset, which is 8, $\bar{x}$ is the mean value of each column and σ is the standard deviation of the data obtained using equation 5.

In the direction of (0002) the measure of spread in FWHM values is within $\leq 1.6\sigma$ around the mean value ($\bar{x}$) of 210.06 arcsec with sigma (σ) of 7.92 arcsec, whereas for $(10\bar{1}1)$ plane the measure of spread in FWHM values is within $\leq 1.6\sigma$ around the mean value ($\bar{x}$) of 1007.64 arcsec with sigma (σ) as 20.48 arcsec.

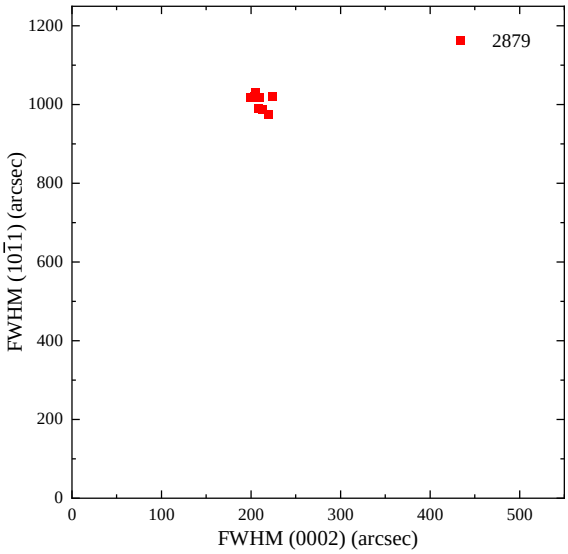

Figure 104: Eight successive measurements of sample (2879) measured following the same procedure and at same XRD settings.

Since we can fit 95% of the measured FWHM data along both the planes within 2σ and there are no outliers beyond it. This gives us confidence in assuming the distribution of the error as a normal (gaussian) distribution.

Based on the above observation, error bars in all the figures using scatter plot containing FWHM data were implemented along the x- and y-axis as can be seen in Figure 105.

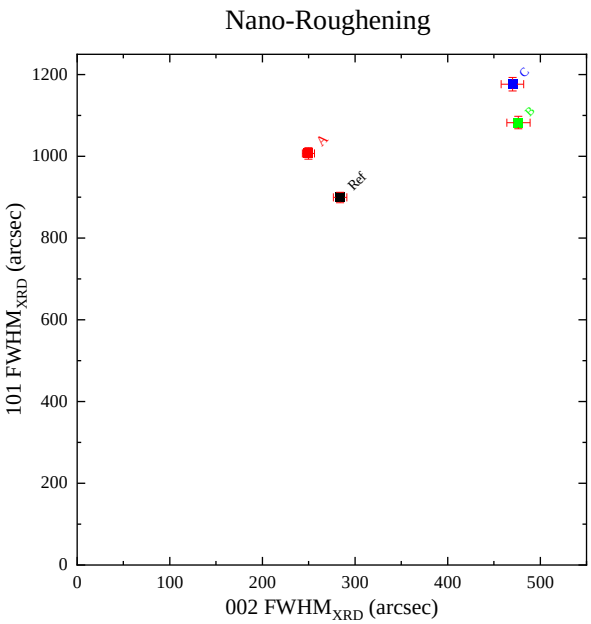

Figure 105: Nano-roughening data (previously measured).

REFERENCES

1. https://www.calculator.net/standard-deviation-calculator.html